Monte Carlo Simulations for BSM Physics and Precision Higgs Physics at the LHC

KUTTIMALAI, SILVAN,SHIWA

Monte Carlo Simulations for BSM Physics and Precision Higgs Physics at the LHC

Silvan Kuttimalai
1st September 2016

Abstract

Monte Carlo event generators are indispensable tools for the interpretation of data taken at particle collider experiments like the Large Hadron Collider (LHC), the most powerful particle collider to date. In this thesis, the general purpose Monte Carlo event generator Sherpa is used to implement a new simulation framework for models that go beyond the Standard Model of particle physics. This is achieved by means of an newly designed interface to a universal format for generic models and by extending existing functionalities in such a way as to handle a generic class of coupling structures that appear in many extensions of the Standard Model. Furthermore, an improved modeling of the dominant LHC Higgs production mechanism in the Standard Model is described and the effects of the improvements are quantified. The improved simulation that is implemented in Sherpa supplements the description of Higgs production at the LHC in terms of an effective Higgs-gluon interaction with finite top quark mass effects that restore a reliable description of the kinematics in events with large momentum transfers. Using this improved description of Higgs production at the LHC, this work demonstrates how the transverse momentum spectrum of the Higgs boson can be used to constrain models that modify the Higgs-gluon coupling. In addition, state-of-the-art Monte Carlo event generation techniques are used in order to assess the sensitivity of analysis strategies in the search for invisibly decaying Higgs bosons. In this analysis, it was found that previously neglected loop-induced contributions have a significant impact and it is demonstrated how multi-jet merging techniques can be used to obtain a reliable description of these contributions. Furthermore, the work presented in the last chapter of this thesis shows how jet substructure techniques can be used in order to search for rare Higgs decays into light resonances that decay further into hadrons. This analysis closes with a demonstration on how such an analysis can be used to constrain extensions of the Standard Model that feature multiple Higgs bosons.

Monte Carlo Simulations for BSM Physics and Precision Higgs Physics at the LHC

Silvan Kuttimalai
1st September 2016

A thesis submitted in partial fulfilment
of the requirements for the degree of
Doctor of Philosophy

Institute for Particle Physics Phenomenology
Department of Physics
Durham University

Contents

List of Figures

List of Tables

Declaration

This thesis is based collaborative research and the corresponding publications, preprints, and proceedings contributions listed below. No part of this thesis has been submitted elsewhere for any other degree or qualification.

Chapter 3 is based on joint research conducted in collaboration with Dr. Stefan Höche, Dr. Frank Siegert, and Jun.-Prof. Dr. Steffen Schumann. This work was published previously in reference [1].

Chapter 4 is based on joint research conducted in collaboration with Malte Buschmann, Dr. Dorival Gonçalves, Prof. Dr. Frank Krauss, Dr. Philipp Maierhöfer, Prof. Dr. Tilman Plehn, and Dr. Marek Schönherr. This work appeared previously in reference [2], section III.2 of reference [3], and section IV.A of reference [4].

Chapter 5 is based on joint research conducted in collaboration with Dr. Dorival Gonçalves, Prof. Dr. Frank Krauss, and Dr. Philipp Maierhöfer. This work appeared previously in references [5, 6].

Chapter 6 is based on joint research conducted in collaboration with Dr. Andrew S. Chisholm, Dr. Konstantinos Nikolopoulos, and Dr. Michael Spannowsky. It has been submitted for publication as reference [7].

Acknowledgements

I would like to thank my supervisor Frank Krauss for valuable guidance and for initiating the many fruitful collaborations I was lucky enough to be part of. I am also grateful for having been given all the freedom I could possibly ask for to pursue my own interests and for the various opportunities I had to present my work at conferences and workshops.

I would like to express my gratitude to all my collaborators, who contributed greatly to my professional and personal development by sharing their experience, providing guidance, and helping with problems I encountered. I thoroughly enjoyed the five weeks I spent working with Stefan Höche at SLAC and I would like to thank him and the SLAC theory group for hospitality. Throughout my time as a PhD student I enjoyed being part of the Sherpa collaboration and I am thankful to everyone in the team who made me feel respected and valued.

The financial support I received from the European Union as part of the FP7 Marie Curie Initial Training Network MCnetITN (PITN-GA-2012-315877) is thankfully acknowledged.

To my mother I am most thankful for the incredible amounts of support she provided in the past and still offers whenever needed.

I would also like to thank Maren, who is the most wonderful person I have ever met and who has now become my wife. I am endlessly grateful for having you, for your companionship, and for the support you provide.

1 Motivation and Outline of this Thesis

Collider experiments provide an environment in which elementary particles can be studied while exchanging large amounts of energy and momentum. For this purpose, beams of particles are accelerated into the highly relativistic regime and then brought to collision. The large amounts of energy available in these collisions allow for the creation of heavy intermediate states that can thus be studied in a controlled environment along with the general high-energy dynamics of particle interactions. The most powerful collider to date is the CERN Large Hadron Collider (LHC) [8–12], where proton-proton collisions are studied using the two general purpose particle detectors ATLAS [13] and CMS [14].

A key item on the LHC physics agenda is the search for the Higgs boson, the last particle in the Standard Model of particle physics (SM) for which no direct experimental evidence was available prior to the commencement of the LHC programme. Within the Standard Model, the Higgs boson plays an important role as it is the remnant of a hypothesised mechanism that breaks a fundamental symmetry of the theory [15–20]. It is responsible for the generation of particle masses in the Standard Model and the underlying mechanism implies a close relationship between a particle's mass and its coupling to the Higgs boson.

The discovery of a Higgs-like particle [21, 22] during the Run-I data taking period of 2011 and 2012 thus marked a major achievement and the already precise determination of its mass $m_h = 125.1\,\text{GeV}$ with an uncertainty of only a few hundred MeV [23] has turned the Standard Model into a fully predictive theory. While the Higgs boson's spin and parity properties as well as its couplings to heavy particles have been found to be compatible with Standard Model expectations [24–26], many of its other properties are still to be determined in order to confirm that the newly discovered particle is fully compatible with a Standard Model Higgs boson. The Higgs boson's couplings to first and second generation fermions need to be constrained in order to confirm the rather peculiar hierarchical structure of Yukawa couplings that is predicted by the Standard Model. Furthermore, the Higgs boson's self couplings need to be determined and its couplings to heavy gauge bosons need to be measured to higher precision in order to rule out alternative electroweak symmetry breaking mechanisms, which could, for example, involve multiple Higgs fields.

Motivation to even consider alternatives to the Standard Model despite its immense success at describing a wide range of phenomena across vast ranges of energies is provided by

both experimental observations and theoretical considerations. For example, observational astrophysical evidence for the existence of *Dark Matter* in the universe has accumulated [27–29]. The existence of Dark Matter is inferred from a number of observations that can currently not be explained without postulating the abundance of a gravitationally interacting non-luminous (and therefore "invisible" or "dark") form of matter, for which the Standard Model provides no candidate.

On the theoretical side, it is clear that the Standard Model cannot be valid up to arbitrarily high energies, as gravitational effects are expected to become sizeable at the Planck scale $M_{\mathrm{Pl}} \approx 10^{28}\,\mathrm{eV}$. These effects are not accounted for by the Standard Model and the consistent inclusion of gravity in a relativistic quantum field theory like the Standard Model is still an unsolved problem. At the same time, almost any imaginable extension of the Standard Model at such a large energy scale would introduce a pathologically strong dependence of qualitative features of the theory on free parameters. As a consequence, these parameters would need to be finely tuned in order to be compatible with observation. This is perceived widely as an unnatural and therefore undesirable feature of the theory. It is commonly referred to as the *fine-tuning problem* or the *hierarchy problem*, as it arises due to the large separation of the electroweak scale from the Planck scale [30–33].

Searches for *new physics* or *beyond the Standard Model* (BSM) physics are therefore another essential part of the LHC programme. So far, no indisputable evidence for new physics has been observed and the parameter spaces of many proposed extensions of the Standard Model were tightly constrained by LHC measurements of Run-I[1].

With the increased centre-of-mass energy now available in proton-proton collisions of Run-II, the sensitivity to physics at even higher energy scales is increased and the precision of measurements will improve as more data will be collected. This increase in experimental precision and reach in model space has to be met on the theoretical side with better predictions for a wider range of models. *Monte Carlo event generators* are numerical computer programs that are used in order to obtain theory predictions for the LHC and thus provide an essential interface between theory and experiment. These generators and their use in the context of Higgs physics and BSM physics at the LHC are the main subject of the work presented in this thesis.

Chapter 2 gives a brief review of modern Monte Carlo event generation techniques with a focus on the Sherpa [36] event generator, which was used throughout this work. The work presented in chapter 3 aimed at addressing some of the challenges outlined above by adapting the Sherpa event generator framework in such a way as to facilitate event generation for a wide range of generic BSM models. Chapter 4 is concerned with improvements on the theoretical modelling of important Higgs production mechanisms within Sherpa. In

[1] See, for example, reference [34] for a summary of constraints on Supersymmetry [35] derived by ATLAS

chapter 5, advanced Monte Carlo techniques are used in order to assess the phenomenological relevance of so-called *loop-induced* scattering reactions at the LHC in the context of Higgs physics and searches for Dark Matter. A new analysis strategy for measurements of rare Higgs decays is presented in chapter 6 and its prospects for Run-II are analysed using Monte Carlo tools.

2 Calculational Techniques in Monte Carlo Event Generation

Monte Carlo Event Generators

In order to improve upon our understanding of the physics that governs particle interactions, one ultimately needs to compare measurements to theoretical model predictions. Given a sufficiently good understanding of the detectors in a collider experiment, one can infer the final state of a scattering reaction from the detector measurement and perform such a comparison. Monte Carlo event generators play a key role in obtaining the corresponding theory predictions and thus provide an essential interface between theory and experiment.

The outcome or final state in a collider experiment is is defined by its particle content and the momenta of the final state particles p_i. In terms of these quantities, one can form a wide range of observables that probe different aspects of a theory. In general, an observable O is a function of the final state f and its momenta

$$O(f; p_1 \dots p_{n_f}). \tag{2.1}$$

The exact outcome, i.e. the final f state with its momenta $p_1, \dots, n_{n_f}$, cannot be predicted for any one specific particle collision, even if the exact initial conditions are known. Therefore, no meaningful prediction for (2.1) can be derived from theory. Within the framework of relativistic quantum field theory, only the differential *probability* for some final state to be produced during a collision can be predicted. This probability is directly proportional to the *differential cross section*

$$\frac{\mathrm{d}\sigma(f; p_1, \dots, p_{n_f})}{\mathrm{d}^3 p_1 \dots \mathrm{d}p_{n_f}}, \tag{2.2}$$

which can be derived from theory. Provided a theory prediction for the differential cross

section, one can make meaningful predictions for the *expectation value* of some observable

$$\langle O \rangle = \mathcal{L} \times \sum_f \int \frac{\mathrm{d}\sigma(f; p_1, \ldots, p_{n_f})}{\mathrm{d}^3 p_1 \ldots \mathrm{d}^3 p_{n_f}} O(f; p_1, \ldots, p_{n_f}) \mathrm{d}^3 p_1 \ldots \mathrm{d}^3 p_{n_f} . \tag{2.3}$$

In order to probe the probability distributions predicted by a theory as accurately as possible, colliders are designed to repeatedly collide particles under near identical initial conditions as many times as possible. The *integrated luminosity* $\mathcal{L}$ in (2.3) is a measure for the number of collisions to be expected over the run time of the experiment under consideration. The higher the integrated luminosity is, the better the discriminating power of an experiment will be when contemplating different possible theory hypotheses.

The complexity of the phase space integral in (2.3) for any realistic number of final state particles n_f renders the calculation of theory predictions extremely challenging. *Monte Carlo integration* techniques are used in event generators in order to cope with the dimensionality of the phase space. In the very simplest form of a Monte Carlo approach, the integral in (2.3) is evaluated numerically by randomly generating a large number M of *phase space points*

$$(p_1^j, \ldots, p_{n_f}^j) \qquad j \in \{1, \ldots, M\}, \tag{2.4}$$

uniformly distributed in the integration region and by exploiting the relation

$$\langle O \rangle = \lim_{M \to \infty} \mathcal{L} \times \frac{V}{M} \sum_f \sum_{j=1}^{M} \left. \frac{\mathrm{d}\sigma(f; p_1, \ldots, p_{n_f})}{\mathrm{d}^3 p_1 \ldots \mathrm{d}^3 p_{n_f}} \right|_{p_i = p_i^j} O(f; p_1^j, \ldots, p_{n_f}^j) \tag{2.5}$$

$$= \lim_{M \to \infty} \mathcal{L} \times \frac{V}{M} \sum_f \sum_{j=1}^{M} w_j^f \, O(f; p_1^j, \ldots, p_{n_f}^j), \tag{2.6}$$

where V is the volume of the integration region. The efficiency of a Monte Carlo integration can be significantly improved upon by generating momenta that are not distributed uniformly but in accordance with the structure of the integrand [37]. Since the analytic structure of the integrand is often unknown, adaptive algorithms [38], which make use of the knowledge about the structure gained throughout the integration procedure, are often employed.

In contrast to what (2.6) suggests, a *fully differential* Monte Carlo event event generator does typically not calculate one specific observable. Instead, it stores the *weights* w_i^f along with the final states and their momenta w_i^f as *events*. These can be thought of as simulated outcomes of a scattering process. Having stored the momenta and weights w_i^f for a generated set of events, one can calculate any observable by simply calculating the observable for each event $O(f; p_1, \ldots, p_{n_f})$ and performing the summation in (2.6). This is a major advantage over an analytic evaluation of (2.3), which is typically only valid for one specific observable.

Fixed-Order Expansion of Matrix Elements

Differential cross sections for elementary particle scattering reactions can be calculated by deriving the corresponding scattering matrix element $\mathcal{M}$ from the underlying theory. In terms of the matrix element, the differential cross section is given by

$$\mathrm{d}\hat{\sigma} = \frac{1}{4\sqrt{(k_a k_b)^2 - m_a m_b}} |\mathcal{M}(k_a, k_b; p_1, \ldots, p_{n_f})|^2 (2\pi)^4 \delta^4(p_0) \prod_{i=1}^{n} \frac{\mathrm{d}^3 p_i}{(2\pi)^3 2E_i} \,. \tag{2.7}$$

The calculation of exact matrix elements for phenomenologically relevant theories and scattering processes are well beyond available calculational techniques and one typically has to resort to approximations. A very successful approach to this problem is the expansion of $\mathcal{M}$ as a power series in the coupling constants. For small values of the coupling constants, a truncation of the series at some finite order can be justified. For a theory that contains only one coupling parameter g, one has

$$\mathcal{M} = g A_1(k_a, k_b; p_1, \ldots, p_n) + g^2 A_2(k_a, k_b; p_1, \ldots, p_n) + g^3 A_3(k_a, k_b; p_1, \ldots, p_n) + \ldots \,. \tag{2.8}$$

A formalism due to Stueckelberg and Feynman formulates straightforwardly applicable recipes for the construction, organisation, and graphic visualisation of all terms that contribute to the coefficient functions A_i at any order i. In this formalism, each term is represented by a *Feynman diagram*. A Feynman diagram is made up of lines that are connected to each other by *vertices*. Each field in the Lagrangian corresponds to a species of lines and each vertex that is allowed to appear in a diagram corresponds to a coupling term in the Lagrangian. In this formalism, the task of finding all terms that contribute to a scattering amplitude boils down to drawing all possible Feynman diagrams allowed by the vertices of the theory and translating each of them into a mathematical expression. Since each vertex contributes a corresponding coupling constant factor, the diagrams that contribute to the leading term in (2.8) usually have a tree-like structure with no closed loops. This is illustrated in figure 2.1a for the production of a Higgs boson H in association with a Z boson through the annihilation of two quarks, $q\bar{q}$. As will be discussed in the following sections, the cross section for this process can only be calculated *inclusively*, as the cross section for the production of some specific final state and nothing else is typically ill-defined. In consequence, a calculation based on the tree-level diagram in figure 2.1a must be interpreted as the leading order contribution to the inclusive process $q\bar{q} \to ZH + X$, where X denoted "anything". In order to calculate this process at the next-to-leading (NLO) order in the strong coupling constant one must therefore include QCD emission diagrams that include an extra parton in the final state, as shown in figure 2.1b. At the same order in the relevant coupling constant,

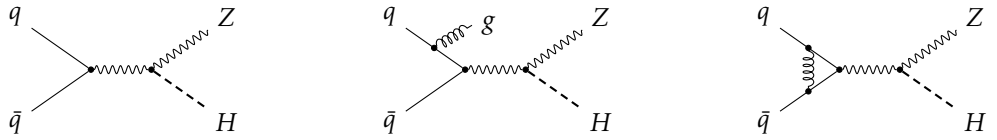

(a) Tree-level diagram. (b) Real-emission diagram. (c) One-loop diagram.

Figure 2.1: Feynman diagrams for the partonic process $q\bar{q} \to ZH$.

one-loop diagrams as shown in figure 2.1c contribute. These NLO corrections are referred to as *real emission corrections* and *virtual corrections*, respectively. It is worth noting that the real emission corrections are tree-level contributions, despite them contributing to the inclusive cross section only at NLO.

Nowadays, the calculation of matrix elements at tree-level is in full generality automatised through numerical programs. Such programs are commonly referred to as *matrix element generators*. Two matrix element generators, Amegic++ [39] and Comix [40], are fully integrated in the Sherpa Monte Carlo and allow for the automatic calculation of fully differential cross sections at the tree-level. Other widely used matrix element generators include MadGraph [41], O'Mega [42], and CalcHEP [43].

Due to the significant complexity of one-loop calculations, numerous numerical programs developed specifically for the evaluation of virtual contributions exist. Among them are OpenLoops [44], BlackHat [45], GoSam [46, 47], and MadLoop [48]. The results presented in this thesis were obtained using OpenLoops in combination with Collier [49, 50], a numerical tool which employs the methods of [51–53] for the evaluation of scalar and tensor integrals.

Factorisation of the Hadronic Cross Section

The methods for calculating differential cross sections outlined in the previous section are directly applicable only if the external particles involved in the scattering process are of elementary nature. If, however, the scattering reaction involves composite strongly interacting particles such as protons, the matrix elements cannot be perturbatively expanded as in (2.8) anymore. The internal structure of protons is governed by energy scales below its mass of about a GeV and thus lie in a non-perturbative regime, where an expansion in α_s, the relevant coupling parameter, does not converge. These low energy effects can, however, be factorised in such a way as to allow for the calculation of scattering cross sections in terms a convolution of partonic cross sections with non-perturbative structure functions. The structure functions capture the low-energy features of the composite hadron an can be measured. The partonic scattering cross sections can be calculated perturbatively in terms of elementary partons, as outlined in the previous section. For hadron-hadron collisions as they

are studied at they LHC, the factorised expression for the cross section for a certain final state $\mathcal{F}$ takes the form

$$\mathrm{d}\sigma = \int_0^1 \int_0^1 \sum_{i,j} f_i(x_1, \mu_F^2) f_j(x_2, \mu_F^2) \, \mathrm{d}\hat{\sigma}_{ij\to\mathcal{F}}(\mu_F, x_1, x_2) \, \mathrm{d}x_1 \, \mathrm{d}x_2 \,, \tag{2.9}$$

where the indices i and j label gluons and all massless quarks in the factorisation scheme. The partonic cross sections $\mathrm{d}\hat{\sigma}_{ij\to\mathcal{F}}$ are then calculated for the partonic scattering reactions $ij \to \mathcal{F}$ according to (2.7). The value of the structure function $f_i(x, \mu_f^2)$ can hence be interpreted as the probability of finding a parton i carrying longitudinal momentum fraction x inside the proton. The structure functions are therefore commonly referred to as *parton distribution functions* (PDFs). The factorisation of low-energy physics into the PDFs comes at the cost of introducing a *factorisation scale* μ_f. As indicated in equation (2.9), both the structure functions and the partonic scattering cross section depend on this dimensionful parameter and on the calculational scheme used to achieve the factorisation. This dependency, however, cancels in the full result. A residual dependence arises in typical calculations only because of the truncation of the partonic cross section some finite order.

It is worth noting that a factorisation in the form of (2.9) has been proven only for certain processes [54]. In fact, it is known that factorisation is violated for non-inclusive observables at higher orders in perturbation theory, see e.g. [55]. Equation (2.9) is nonetheless typically used in Monte Carlo event generators, assuming that factorisation violating effects are sufficiently small as to justify this practice.

Soft and Collinear Factorisation of QCD Matrix Elements

A well known feature of QCD matrix elements is their behaviour in the limit in which the momenta of two partons become collinear or one final state gluon becomes soft [56–59]. The leading behaviour of QCD Matrix elements in these regimes arises diagrammatically from splittings of external parton lines as illustrated in figure 2.2, where gluon that is connected to the rest of the diagram splits into a pair of quarks. In terms of the "mother" parton's momentum p_a and the two "daughter" partons' momenta p_b, p_c, the collinear limit is commonly parametrised in terms of the energy fraction $z = E_b/E_a$ of the splitting and the virtuality t of the mother parton, for which we have in the collinear limit:

$$\theta \to 0 \Rightarrow t = p_a^2 \to 0 \,. \tag{2.10}$$

In this small angle limit, the differential cross section $\mathrm{d}\sigma_1$ factorises into process independent *splitting kernels* $\hat{P}_{ab}$ and the differential cross section $\mathrm{d}\sigma_0$ for the process in which the partons

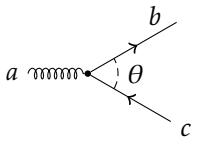

Figure 2.2: Splitting of an external gluon into a pair of quarks. The rest of the diagram, to which the gluon is connected, is not shown.

labelled b and c are replaced by their mother parton a

$$\mathrm{d}\sigma_1 \xrightarrow{t \ll Q^2} \mathrm{d}\sigma_0 \frac{\alpha_s}{2\pi} \frac{\mathrm{d}t}{t} \mathrm{d}z \hat{P}_{ab}(z). \tag{2.11}$$

The reference scale Q denotes the smallest kinematic invariant that characterises the partonic cross section $\mathrm{d}\sigma_0$. Equation (2.11) is differential only in z, t, and the partonic kinematics of $\mathrm{d}\sigma_0$. An additional azimuthal angle as well as the the spins and polarisations of external partons are understood to be averaged over. The explicit form of the *unregularised Altarelli-Parisi splitting kernels* $\hat{P}_{ab}$ can be found in standard textbooks, e.g. in references [58, 59].

While equation (2.11) is particularly simple because it only involves the kinematics of on pair of partons, there are corrections to this relation for partonic configurations in which an emitted gluon's energy E becomes small without being emitted collinearly with respect to any other parton. Such a gluon is emitted coherently off the collective ensemble of partons. In this limit, the factorised form of the cross section reads

$$\mathrm{d}\sigma_1 \xrightarrow{E^2 \ll Q^2} \mathrm{d}\sigma_0 \frac{\alpha_s}{2\pi} \frac{\mathrm{d}\Omega}{2\pi} \frac{\mathrm{d}E}{E} \sum_{i,j} C_{ij} W_{ij}\,, \tag{2.12}$$

where the summation includes all pairs i, j of strongly interacting external particles in the process corresponding to $\mathrm{d}\sigma_0$. In equation (2.12), Ω denotes the solid angle of the gluon's momentum. The colour factor C_{ij} depends on the colour charges of partons i and j, while W_{ij} depends on their momenta and the momentum of the soft gluon q:

$$W_{ij} = \frac{E^2 p_i p_j}{(p_i q)(p_j q)}. \tag{2.13}$$

The factorised form of (2.12) correlates emissions off all possible pairs of partons i, j. This is in contrast to the collinear case, where only the kinematics and colour charge of the collinear pair of partons enter in the factorised form of (2.11).

Jet Cross Sections

An important implication of equations (2.11) and (2.12) is that partonic cross sections with QCD partons in the final state can potentially diverge in the soft and collinear limit, i.e. when $t \to 0$ or $E \to 0$. These partonic cross sections are therefore ill-defined. Experimentally, it is not even possible to measure such a cross section. In the soft limit, one would have to distinguish a final state with a gluon carrying zero energy from a final state in which this gluon is not present. Similarly, one cannot distinguish a pair of exactly collinear partons from a single parton carrying the combined quantum numbers of the pair. Sensible observables must therefore meet a criterion that is commonly referred to as *infrared safety*. In the limit in which a collinear or soft splitting occurs, an observable $\mathcal{O}$ must obey

$$\mathcal{O}(f_{n+1}; p_1, \ldots, p_{n+1}) \longrightarrow \mathcal{O}(f_n; p_1, \ldots, p_n) \tag{2.14}$$

in order to be infrared safe. In (2.14), f_n is understood to be the final state one obtains from f_{n+1} by removing the arbitrarily soft gluon or the collinear splitting.

Among the most widely studied infrared safe observables are so-called event shape variables [60] and jet cross sections. In order to render cross sections for processes with QCD partons in the final state and the corresponding observables finite, jet cross section definitions introduce some resolution criterion that classifies emissions as either resolvable or unresolvable. For this purpose, *jet algorithms* are used. They successively combine (or *cluster*) unresolvable emissions into composite *jets* until no unresolvable emissions remain. By means of a jet algorithm, partonic configurations can thus be mapped onto jets, in terms of which one can define infrared safe observables. When calculating the n-jet cross section according to some jet algorithm, the phase space integrals of the terms in equations (2.11) and (2.12) over t and E, respectively, are then cut off at some lower bound that is related to the resolution criterion. As a remnant of the divergent structure of the matrix elements, a logarithmic dependence on the cutoff Q_0 typically arises. In e^+-e^- collisions, for example,

the n-jet fractions for the k_T-jet algorithm are given by [61, 62]:

$$\begin{aligned}\frac{\sigma_n}{\sigma_2} = &\left[\left(\frac{\alpha_s}{\pi}\right)\left[A_{12}^{(n)}\log^2\left(\frac{\mu_Q^2}{Q_0^2}\right) + A_{11}^{(n)}\log^1\left(\frac{\mu_Q^2}{Q_0^2}\right) + \ldots\right]\right.\\ &+\left(\frac{\alpha_s}{\pi}\right)^2\left[A_{24}^{(n)}\log^4\left(\frac{\mu_Q^2}{Q_0^2}\right) + A_{23}^{(n)}\log^3\left(\frac{\mu_Q^2}{Q_0^2}\right) + \ldots\right]\\ &+\left(\frac{\alpha_s}{\pi}\right)^3\left[A_{36}^{(n)}\log^6\left(\frac{\mu_Q^2}{Q_0^2}\right) + A_{35}^{(n)}\log^5\left(\frac{\mu_Q^2}{Q_0^2}\right) + \ldots\right]\\ &\left.+\ldots\right]\end{aligned} \tag{2.15}$$

For small resolution scales Q_0, the logarithms in equation (2.15) can become large and the presence of these large logarithms spoils the convergence of a power series in α_s. If eventually $\alpha_S \log^2(\mu_Q^2/Q_0^2) \approx 1$, the truncation of (2.15) at any fixed order will fail to give a reasonable approximation. In this regime, fixed order matrix elements need to be supplemented by *resummation techniques*, which aim at summing up the largest logarithmic terms in (2.15) to all orders in α_s. In Monte Carlo event generators, this is typically achieved through *parton shower* algorithms, which will be subject of the next section.

Parton Showers

The PDFs appearing in equation (2.9) can presently not be calculated perturbatively. Instead, they are instead measured in experiments. Their scale dependence with respect to μ_f can, however, be calculated perturbatively. Requiring (2.9) to be independent of μ_f at the desired order in α_s, one obtains the *Dokshitzer-Gribov-Lipatov-Altarelli-Parisi* (DGLAP) equations [56, 63–65], which govern the scale dependence of the PDFs:

$$t\frac{\partial}{\partial t}\left(\frac{f_a(x,t)}{\Delta_a(t_0,t)}\right) = \frac{1}{\Delta_a(t_0,t)}\sum_b \int \frac{\mathrm{d}z}{z}\frac{\alpha_s(t)}{2\pi}\hat{P}_{ba} f_b(x/z,t) \tag{2.16}$$

As is evident from equation (2.16), the PDF evolution is determined by the Altarelli-Parisi splitting kernels, which characterise QCD matrix elements in the collinear limit (see equation (2.11). In terms of these kernels, the *Sudakov form factor* is given by

$$\Delta_a(t_0,t) = \exp\left[-\sum_b \int_{t_0}^{t}\frac{\mathrm{d}t'}{t'}\int_{\epsilon(t_0,t')}^{1-\epsilon(t_0,t')}\mathrm{d}z\frac{\alpha_s(t')}{2\pi}\hat{P}_{ab}(z)\right]. \tag{2.17}$$

With this definition, one can cast equation (2.16) in integral form

$$f_a(x,t) = \Delta_a(t_0,t) f_i(x,t_0) + \sum_b \int_{t_0}^{t} \frac{\mathrm{d}t'}{t'} \frac{\Delta_a(t_0,t)}{\Delta_a(t_0,t')} \int_0^1 \frac{\mathrm{d}z}{z} \frac{\alpha_s(t')}{2\pi} \hat{P}_{ba} f_b(x/z,t') \tag{2.18}$$

$$= \Delta_a(t_0,t) f_i(x,t_0) + \sum_b \int_{t_0}^{t} \frac{\mathrm{d}t'}{t'} \Delta_a(t',t) \int_0^1 \frac{\mathrm{d}z}{z} \frac{\alpha_s(t')}{2\pi} \hat{P}_{ba} f_b(x/z,t'). \tag{2.19}$$

The above evolution equations can be interpreted probabilistically as follows [58]. As mentioned above, the structure functions can be thought of as parametrising the proton in terms of a probabilistic ensemble of partons. The probability of finding a specific parton a with momentum fraction x is given by $f_a(x,t)$, where t denotes the squared momentum scale at which one probes the proton. At any t, they can be assigned the differential splitting probability of $\frac{\alpha_s}{2\pi}\mathrm{d}t/t \int \mathrm{d}z \hat{P}_{ab}(z)$, in accordance with (2.11). The Sudakov form factor $\Delta(t_0,t)$ then gives the probability for a parton in the ensemble *not* to split when evolving from t_0 to t. Equation (2.19) therefore gives the distribution of partons at t in terms of the distribution at t_0 by "counting" the number of partons at x that did not branch between t_0 and t (first term on the right-hand side) and adding the partons from all other x that *did* branch in such a way as to produce a parton that carries momentum fraction x (last term on the right-hand side). The cutoff $\epsilon(t_0,t')$ imposed on the energy fraction z in the definition of the Sudakov form factor in (2.17) effectively defines a minimum energy for a resolvable splitting at virtuality t'. It is therefore typically closely related to the corresponding cutoff imposed on the virtuality, t_0, but ultimately a matter of choice.

The probabilistic treatment outlined above, which recovers the DGLAP evolution equations, is implemented in modern *parton shower* algorithms. In the initial state, the PDFs are evaluated at the typical scale of the partonic scattering μ_Q^2 first, and then evolved downwards towards some cutoff $t_0 < \mu_Q^2$. This *backwards evolution* requires only minor modifications [66] to the treatment outlined above, where a forward evolution was assumed. The additional final state particles produced through branchings during the evolution are treated in a similar manner. With every new branching giving rise to more final state particles that can further split, a parton cascade develops. Since the splitting kernels of parton showers are derived from the appropriate matrix elements in the soft and collinear region, the leading and next-to-leading logarithmic terms in expression (2.15) for the jet rates are correctly

recovered. They are of the form

$$\text{LL} \qquad \alpha_S^n \log^{2n} \left(\frac{\mu_Q^2}{Q_0^2} \right), \tag{2.20}$$

$$\text{NLL} \qquad \alpha_S^n \log^{2n-1} \left(\frac{\mu_Q^2}{Q_0^2} \right) \tag{2.21}$$

A parton shower can therefore *resum* the potentially large logarithms in (2.15) to all orders.

Multi-Jet Merging

While a parton shower algorithm appropriately describes QCD corrections due to multiple soft and collinear emissions, the underlying approximation of QCD matrix elements through splitting kernels $\hat{P}_{ab}$ fails outside that specific kinematic region. For hard, wide-angle emissions, a hierarchy of scales that induces large logarithms as in (2.15) is typically absent, such that the calculation of these cross sections in terms of fixed-order matrix elements is more accurate. In that sense, the parton shower approach is complimentary to calculating QCD emission corrections at fixed order in α_s. It is therefore desirable to combine the two methods in such a way as to retain the accuracy of either approach in the kinematic regions in which it performs best. *Multi-jet merging techniques* are designed to achieve this. The discussion here will be focused on the *CKKW* algorithm, which is the method implemented in the Sherpa event generator. It was proposed in the context of e^+-e^- collisions in [67] and generalised to hadronic collisions in [68, 69]. Variants of this approach include the *CKKW-L* [70] and the *MLM* [71, 72] merging schemes. A comparative study of these methods can be found in [73, 74].

Common to most multi-jet merging techniques is the general idea of separating the phase space into two domains, one of which is dominated by soft and collinear radiation, the complimentary region being dominated by hard and wide-angle emissions. Starting with some core process of interest with final state multiplicity n, any extra QCD emission is assigned a dimensionful scale Q_{n+1} that characterises its hardness. In the CKKW approach, a k_T-type measure [61, 62, 75, 76] is used in order to quantify the hardness of an emission. If the hardness of an emission is below a certain threshold $Q_{n+1} < Q_{\text{cut}}$, it is generated as usual by the parton shower. If instead $Q_{n+1} > Q_{\text{cut}}$, the differential cross section of the corresponding final state is calculated using fixed-order matrix elements. In order to restore the logarithmic accuracy of the parton shower in the matrix element region, the differential cross section is supplemented with appropriate Sudakov factors. This does not affect the accuracy of the matrix elements at fixed order in α_s, and fixed-order matrix element accuracy

is therefore guaranteed above Q_{cut}. In order to avoid double-counting of configurations that arise through the shower and through matrix element emissions above Q_{cut}, a *truncated shower* has to be employed that vetoes any further emission above Q_{cut} [69]. Schematically, events are thus generated according to the following expression for the cross section:

$$\begin{aligned}\sigma = \int \mathrm{d}\phi_n B_n(\Phi_n)\Bigg[\Delta_n(t_0,\mu_Q^2) + \int\limits_{t\in[t_0,\mu_Q^2]} \mathrm{d}\Phi_1 \mathrm{K}_n(\Phi_1)\Delta_n(t,\mu_Q^2)\Theta(Q_{\text{cut}}-Q_{n+1})\Bigg] \\ + \int \mathrm{d}\Phi_{n+1} B_{n+1}(\phi_{n+1})\Delta_n(t,\mu_Q^2)\Theta(Q_{n+1}-Q_{\text{cut}})\end{aligned} \tag{2.22}$$

The first line of equation (2.22) represents the core $2 \to n$ process calculated with fixed-order matrix elements (the Born-level process B_n) supplemented by a parton shower that is restricted to emissions below Q_{cut}. Correspondingly, it is written in terms of the one-particle emission phase space of the shower

$$\mathrm{d}\phi_1 = \mathrm{d}t\,\mathrm{d}z\,\mathrm{d}\phi J(t,z,\phi), \tag{2.23}$$

with the appropriate Jacobian $J(t,z,\phi)$. In order to keep the notation legible and focused on the relevant aspects, summations over all possible flavour combinations of splittings will be omitted throughout. In this somewhat symbolic notation, the Sudakov form factor can be written as

$$\Delta_n(t_0,t) = \exp[-\int\limits_{t\in[t_0,t]} \mathrm{d}\phi_1 K_n(\phi_1)], \tag{2.24}$$

where K_n denotes the sum of all splitting kernels applicable to the Born flavour configuration

$$K_n(\phi_1) = \frac{\alpha_s}{2\pi}\sum_i P_{a_i b_i}(z). \tag{2.25}$$

The Heaviside theta function on the first line of equation (2.22) implements the phase space restriction to emissions below Q_{cut}. Emissions above Q_{cut} are then generated according to the term on the last line of equation (2.22). Expanding this term in α_s and retaining only the leading term in α_s, one recovers the full fixed order result, as desired. For fully inclusive

observables, it is useful to rewrite equation (2.22) as follows:

$$\begin{aligned}\sigma = &\int \mathrm{d}\phi_n B_n(\phi_n)\left[\Delta_n(t_0,\mu_Q^2) + \int\limits_{t\in[t_0,\mu_Q^2]} \mathrm{d}\phi_n K_n(\phi_1)\Delta_n(t_{n+1},\mu_Q^2)\right] \\ &+ \int \mathrm{d}\Phi_{n+1}\left[B_{n+1}(\Phi_{n+1}) - B_n(\Phi_n)K_n(\Phi_{n+1})\right]\Delta(t,\mu_Q^2)\Theta(Q_{n+1}-Q_{\mathrm{cut}}).\end{aligned} \tag{2.26}$$

The first line in (2.26) represents the result one would obtain using a normal parton shower in combination wit matrix elements for the core process. Due to the unitary nature of the parton shower, the terms in the square bracket of this term integrate to one, reproducing the fixed leading order result for the inclusive cross section. The second line, however, gives a higher-order correction that arises from the additional matrix elements which are used for emissions above Q_{cut}. Full consistency would require to include the corresponding virtual corrections as well. In order to keep the impact of this correction to inclusive quantities under control, Q_{cut} cannot be chosen arbitrarily small. It should instead be chosen in such a way as to restrict the corrections to a hard phase space regime in which they are justified.

While the merging method outlined above leads to an improved description of one emission above Q_{cut}, it can be straightforwardly iterated in order to include fixed order matrix elements of yet higher jet multiplicities. This is achieved by iteratively applying the master equation (2.22) to the term involving B_{n+1} in (2.22). This preserves all properties of the algorithm and effectively implements fixed-order matrix element corrections to higher jet multiplicities. In practice, the number of jets one can describe at fixed order accuracy using this method is nonetheless limited by the availability of computing power for the evaluation of high multiplicity matrix elements.

NLO-Subtraction

In the previous sections, it was implicitly assumed that fixed-order cross sections were calculated at leading order (LO). A rapid development of calculational techniques in the recent past has lead to the full automatisation of calculations at the next-to-leading order (NLO) in α_s, despite a considerable increase in complexity when going from LO to NLO. When calculating some process at NLO, one generically has to include real-emission corrections R that are due to final state configurations in which an additional emission is not resolved. Without applying a finite resolution criterion, an observable is ill-defined, as discussed previously. Additionally, virtual corrections V that are due to one-loop diagrams contribute at NLO. As shown in figure 2.1, real-emission corrections reside in a higher dimensional phase space than the Born contribution and the virtual corrections due to the additional

QCD parton in the final state. One therefore has to calculate two integrals of different phase space dimensionality in order to obtain an NLO cross section:

$$\sigma = \int \mathrm{d}\phi_B \Big[B(\phi_B) + V(\phi_B) \Big] + \int \mathrm{d}\phi_R R(\phi_R). \tag{2.27}$$

In the soft and collinear region, the real-emission matrix elements in R are divergent, as discussed previously. However, according to the *Kinoshita-Lee-Nauenberg theorem* [77, 78], any divergence in R will eventually be cancelled by a divergence in the virtual corrections V, thus rendering the overall result finite. Evaluating the two divergent integrals in (2.27) separately using Monte Carlo techniques is, however, not possible. A commonly employed strategy to overcome this problem is to introduce subtraction terms that match the infrared behaviour of the real emission matrix elements. Those terms are then subtracted from the integrand in the real emission phase space $\mathrm{d}\phi_R$, thus cancelling the divergences. Adding the integrated subtraction terms back in the integral over the born phase space then also cancels the divergences in the loop corrections. Schematically, events are thus generated according to

$$\sigma = \int \mathrm{d}\phi_B \Big[B(\phi_B) + V(\phi_B) + \mathcal{I}(\phi_B) \Big] + \int \mathrm{d}\phi_R \Big[R(\phi_R) - \mathcal{D}(\phi_R) \Big], \tag{2.28}$$

where $\mathcal{D}$ denotes the sum of all differential subtraction terms necessary to cancel the divergences in the real emission terms R. Integrating these terms over the one-particle emission phase space gives the integrated subtraction terms $\mathcal{I}$, which cancel the infrared divergences in V. In the overall sum, any contribution from the subtraction terms $\mathcal{D}$ and $\mathcal{I}$ cancel each other, such that (2.28) reproduces the exact NLO-accurate cross section. Since the infrared behaviour of the matrix elements is universal, one can fully automate the generation and calculation of subtraction terms. Subtraction schemes that employ this technique include the antenna subtraction method [79–81], the FKS scheme [82, 83] and the Catani-Seymour dipole subtraction technique [84], which is implemented in Sherpa [85] and which will be described in what follows.

In order to mimic the behaviour of matrix elements in both the collinear and the soft limit, the subtraction terms in the Catani-Seymour formalism replicate the dipole-like structure of (2.12):

$$\mathcal{D}(\phi_R) = \sum_{i,j} \sum_{k \notin \{i,j\}} D_{ij}^k(\phi_R). \tag{2.29}$$

A dipole D_{ij}^k is designed to approximate the limit in which $p_i p_j \to 0$ and it depends on an additional *spectator* QCD-parton k. For the case where all partons labelled i, j, k are final

state particles, we have

$$D_{ij}^{k} = -\frac{1}{2p_i p_j}\mathcal{M}^{*}(p_1,\ldots,\tilde{p}_{(ij)},\ldots,\tilde{p}_k,\ldots,p_n)\frac{T_i T_j}{T_{(ij)}^2}V_{ij,k}\mathcal{M}(p_1,\ldots,\tilde{p}_{(ij)},\ldots,\tilde{p}_k,\ldots,p_n), \tag{2.30}$$

where $\mathcal{M}$ denotes the matrix elements for the partonic configuration that arises from replacing partons i and j with a mother parton labelled (ij) that carries their combined quantum numbers. T_i and T_j are matrices in colour space, but their colour indices and the corresponding indices of $\mathcal{M}$ are suppressed in (2.30). The momenta $\tilde{p}_{(ij)}$ and $\tilde{p}_k$ are determined through a specific momentum mapping that allows all partons to be on shell simultaneously while ensuring $\tilde{p}_{(ij)}+\tilde{p}_k = p_i+p_j+p_k$. The specific form of this mapping, explicit expressions for the colour matrices and factors in (2.30), and a treatment of cases in which initial state partons are involved can be found in reference [84]. Since the factorised form of equation (2.30) allows one to construct subtraction terms in terms of only born-level matrix elements and process-independent building blocks, it is customary to write, in a symbolic notation [84],

$$\int \mathrm{d}\phi_R \mathcal{D}(\phi_R) = \sum_i \int \mathrm{d}\sigma_B \otimes \mathrm{d}V_i\,. \tag{2.31}$$

The employed kinematic mapping allows for a factorisation of the phase space in such a way as to facilitate the explicit analytic evaluation of the process-independent part $\mathrm{d}V_i$ in dimensional regularisation. In turn, this allows one to write the integrated subtraction term as

$$\int \mathrm{d}\phi_B \mathcal{I}(\phi_B) = \sum_i \int \mathrm{d}\sigma_B \otimes \mathrm{d}V_i \tag{2.32}$$

The resulting poles in the regulator can be cancelled explicitly against the poles in the virtual corrections V, thus rendering all integrals in (2.28) separately finite.

NLO-Parton shower matching

Combining a parton shower algorithm with fixed-order cross sections is particularly simple at leading order. When calculating cross sections at NLO, special care must be taken in order to avoid a "double-counting" of emissions when adding a parton shower. In a naive approach, such double-counting can arise when QCD emissions are generated by the parton shower at leading logarithmic accuracy, despite already being included at full leading order accuracy in the real emission corrections of the fixed-order cross section. The parton shower thus needs to be consistently *matched* to the NLO fixed-order cross section. The most commonly

employed matching methods include the MC@NLO technique [86] and POWHEG [87, 88]. The MC@NLO technique will be described in what follows, since it it the method employed throughout the work that will be presented in this thesis. For the same reason, the focus will be on the special case in which NLO subtraction dipoles are used as parton shower evolution kernels. Note that such a dipole shower, as the name suggests, does not evolve external QCD partons individually, but rather in pairs forming a colour-dipole [85]. Using this type of evolution, one can take into account the correlations between emissions in the soft limit, as implied by the dipole-like structure of equation (2.12).

The MC@NLO matching procedure is most conveniently formulated in terms of the differential *NLO-weighted Born cross section*

$$\bar{B}(\phi_n) = B_n(\phi_n) + V_n(\phi_n) + \mathcal{I}_n(\phi_n) - \int \mathrm{d}\phi_1 \mathcal{D}(\phi_{n+1})\theta(t - \mu_Q^2) \tag{2.33}$$

and the hard remainder function

$$H_n(\phi_{n+1}) = R_n(\phi_{n+1}) - \mathcal{D}(\phi_{n+1})\theta(\mu_Q^2 - t). \tag{2.34}$$

The argument t the in the theta-functions in (2.34) and (2.33) is defined for each dipole term in $\mathcal{D}$ separately according to its kinematic mapping and phase space factorisation, written in the form of (2.23). The MC@NLO Sudakov form factor

$$\Delta_n^A(t_0, t) = \exp\left[-\int_{t_0}^{t} \mathrm{d}\phi_1 \frac{\mathcal{D}_n(\phi_n, \phi_1)}{B_n(\phi_n)}\right] \tag{2.35}$$

implicitly depends on ϕ_n, as opposed to the standard parton shower Sudakov form factor. In terms of the above expressions, MC@NLO events are generated according to

$$\begin{aligned}\sigma = \int \mathrm{d}\phi_n \bar{B}_n(\phi_n)\left[\Delta_n^A(t_0, \mu_Q^2) + \int_{t_0}^{\mu_Q^2} \mathrm{d}\phi_1 \frac{\mathcal{D}_n(\phi_n, \phi_1)}{B_n(\phi_n)} \Delta_n^A(t, \mu_Q^2)\right] \\ + \int \mathrm{d}\phi_{n+1} H(\phi_{n+1}).\end{aligned} \tag{2.36}$$

The term proportional to the fixed a fixed-order part $\bar{B}_n$ is written as a sum of contributions with no resolvable parton shower emission and at least one resolvable parton shower emission on the first line. The second line represents events a fixed-order hard emission term, written inclusively. Events that correspond to this term and the events that correspond to the first line in (2.36) after the first step in the parton shower can be treated by a normal parton shower, as in the case of a leading order calculation. On can show that events generated according to this prescription do not suffer from any double counting [86]. The advantage

of an NLO-matched simulation over an LO multi-jet merged calculation is that one-jet observables are described with leading order precision throughout the entire phase space. Furthermore, inclusive observables are described with NLO precision and with no spurious dependence on an unphysical merging scale.

Multi-Jet Merging at NLO

The merging algorithm described previously at leading order has been extended in such a way as to make use of NLO matrix elements [89, 90]. In this scheme, an MC@NLO-matched calculation of the core process is supplemented with MC@NLO-matched calculations of processes with additional jets in the final state. In contrast to leading order merging, NLO accuracy for the core process and for jet observables above the merging scale Q_{cut} are thereby guaranteed. The construction of the corresponding algorithm schematically follows the leading order technique, with the additional complication that an inclusive observable sensitive to n-jet configurations above Q_{cut} will receive contributions from n-parton matrix elements (including their virtual corrections) and $n+1$-parton matrix elements. The resulting expressions can be found in [89] and will not be repeated here. It is worth noting, however, that this merging technique has been fully automated within the Sherpa event generator. With this automatised implementation, a merged calculation can be performed for any process for which fixed-order NLO matrix elements and sufficient computing power are available.

Hadronisation Models, Hadron Decays, and Underlying Event

One important aspect of QCD is *colour confinement*. Colour confinement follows from the fact that QCD becomes strongly coupled at small energies. This in turn implies that colour-charged objects and in particular QCD partons cannot propagate on long timescales. Instead, they *hadronise* into composite hadrons with no net colour charge. In collider experiments, these hadrons are observed instead of the fundamental QCD partons. Since hadronisation is a consequence of QCD becoming strongly coupled, it cannot be treated perturbatively. In Mote Carlo event generators, the perturbative QCD evolution performed by the parton shower is therefore stopped at a low cutoff scale near $\Lambda_{\text{QCD}} \approx 200\,\text{MeV}$ where QCD becomes non-perturbative. The subsequent hadronisation process is then simulated using phenomenological models which are motivated by certain aspects of QCD. Among the most widely used models are the Lund string model [91–93] and the cluster hadronisation

model [94–96]. It is the latter that is implemented in Sherpa [97]. After the hadronisation step, any unstable hadrons are treated by an iterative hadron decay simulation. For this purpose, experimental input on the relevant branching ratios is used.

Hadronic activity that goes beyond parton shower effects, hadronisation and hadron decays in hadronic collisions is attributed to the *underlying event* in Monte Carlo event generators. Phenomenologically, the underlying event manifests itself in the presence of additional jets which are uncorrelated with the actual hard scattering process being studied. The additional soft jets have only little impact on experimentally reconstructable jet observables but rather affect global event observables like the overall sum of particle transverse energy or the overall charged particle multiplicity. Experimentally, underlying event effects at the LHC have been measured both by ATLAS [98–101] and by CMS [102–106]. In Sherpa and other Monte Carlo generators, these effects are modelled by multiple parton-parton interactions within the same hadron-hadron collision [107].

3 Monte Carlo Simulation of BSM Physics

As mentioned in chapter 1, one of the primary purposes of the LHC experiments is to search for physics beyond the Standard Model. BSM searches are motivated by conceptual issues of the Standard Model and already existing experimental evidence for phenomena that cannot be explained by the Standard Model. A vast variety of general theoretical concepts for the extension of the Standard model as well as concrete BSM models are being considered both by the experimental and the theoretical community. Additionally, the description of generic BSM physics in terms of non-renormalisable effective theories has recently gained attention. In any case, Monte Carlo generators are an indispensable tool for the purpose of predicting collider signatures of BSM models, for optimising search strategies, and for setting exclusion bounds on BSM model parameters.

The variety of models that are being studied using LHC data has therefore triggered the development of automatised computational tools that facilitate the implementation of BSM models in Monte Carlo event generators. Rather than deriving and implementing Feynman rules for each model by hand, the use of computational tools that automate this process has become standard. Examples of such tools include LanHEP [108–112], Sarah [113–116], and FeynRules [117–122]. Starting from a model description in terms of a Lagrangian, these programs can provide Monte Carlos and matrix element generators with all the information that is required in order to compute differential scattering cross sections from the input parameters of the model.

In the past, the Sherpa Monte Carlo was used for BSM calculations in the context of various models, most of which were implemented by hand [123–127]. A dedicated interface allowed for the use of model input provided through FeynRules while still imposing severe restrictions on the type of interactions that were allowed to appear in the theory. The aim of the work presented in this section is to lift these restrictions and to adopt a universal and Monte Carlo generator independent format for the model input rather that to rely on a dedicated interface to only one of the available tools that are available for the calculation of Feynman rules.

3.1 The Universal FeynRules Output Format

Initially, the communication between FeynRules and Sherpa was achieved through a dedicated interface. With the development of the *Universal FeynRules Output* (UFO), a universal format that is intended to be usable by any matrix element generator became available [128]. A model written out in this format is unambiguously defined in terms of its particle content, its Feynman Rules, and its free parameters. The format is designed to be fully generic in the sense that it can accommodate any quantum field theory that is defined in terms of a gauge and Lorentz invariant Lagrangian with local interactions of quantum fields with spin 1/2, 1, 3/2, and 2. Part of the UFO convention is also a file format for the specification of free parameters which complies largely with the SLHA standards [129–131].

In the UFO format, models are distributed as Python modules. A model can hence be accessed though a Python interpreter by importing the respective module. No dedicated parsing routines are therefore required in order to access the format. Another advantage of the format is its extensibility, which is facilitated by the design of the Python language. Attributes can be added to any object in a UFO model without making any changes to the structure of the format itself.

The use of the standardised UFO format for models along with its input format for free parameters is clearly advantageous because it greatly facilitates the validation procedures across different matrix element generators. In also renders the continuous maintenance of dedicated interfaces between Feynman rule generators an matrix element generators redundant. Correspondingly, it has been adopted by various matrix element generators, such as GoSam [46, 47], Herwig [132, 133], and MadGraph [134]. Furthermore, the format is now supported by the Feynman rule calculators LanHEP and Sarah.

3.2 Tree-Level Matrix Elements in Comix

Previous versions of Sherpa relied on Amegic [39] as a matrix element generator for BSM physics. In terms of computational efficiency for high-multiplicity final states, the techniques employed by Comix [40] are, however, superior to the diagrammatic approach that is implemented in Amegic. The efficiency of the algorithm implemented in Comix relies on an an extension of the Berends-Giele recursion relations of references [135, 136] to full scattering amplitudes [137].

The algorithm is formulated in terms of so-called *off-shell currents*. An off-shell current is characterised by the quantum numbers of the particle or field it represents and hence carries colour and Lorentz indices accordingly. For the sake of notational convenience, those indices will often be omitted in what follows. In order to formulate a recursion relation

for off-shell currents, consider a scattering process with $N+1$ external particles. Let ω_i denote the quantum numbers of the i-th external particle with $i \in \{0,\dots,N\}$. Let furthermore $\Omega = \{\omega_i\}_{i=1}^{N}$ and let $\mathcal{P}_l(\Omega)$ be the set of partitions of Ω into l subsets. The off-shell current $\mathcal{J}_{\omega_0}(\Omega)$ is then recursively defined via

$$\mathcal{J}_{\omega_0}(\Omega) = P_{\omega_0} \sum_{l} \sum_{\substack{\{\Omega_1,\dots,\Omega_l\} \\ \in P_l(\Omega)}} \sum_{\beta_1,\dots,\beta_l} S(\{\Omega_1,\dots,\Omega_l\}) \mathcal{V}(\omega_0,\beta_1\dots\beta_l) \mathcal{J}_{\beta_1}(\Omega_1)\dots\mathcal{J}_{\beta_l}(\Omega_l), \tag{3.1}$$

where $\mathcal{V}(\omega_0,\beta_1\dots\beta_l)$ is the sum of all vertices in the Lagrangian of the model that couples fields with the quantum numbers $\omega_0,\beta_1\dots\beta_l$. P_{ω_0} is the momentum space propagator of the field corresponding to ω_0 in the usual Feynman diagram formalism. The recursion is initiated by the external currents $\mathcal{J}_{\omega_i}(\{\omega_i\})$, which are defined to be the external wave function factors for the particle of type ω_i in the standard momentum space Feynman rules of the theory. As the diagrammatic representation of this recursion in figure 3.1 illustrates, the current $\mathcal{J}_{\omega_0}(\Omega)$ represents the sum of all Feynman diagrams with external particles Ω and one uncontracted propagator of type ω_0. Removing this propagator and contracting the remaining object with the external wave function for ω_0, one therefore obtains the full amplitude as

$$\mathcal{M} = \mathcal{J}_{\omega_0}(\{\omega_0\}) P_{\omega_0}^{-1} \mathcal{J}_{\omega_0}(\Omega). \tag{3.2}$$

The factor $S(\{\Omega_1,\dots,\Omega_l\}) \in \{-1,+1\}$ in 3.1 is a symmetry factor that is necessary if fermions are among the external particles. In a recursive approach, the determination of this factor is nontrivial if the theory contains Majorana fermions. The techniques proposed in reference [138] are implemented in Comix for this purpose.

With the Lorentz and colour indices suppressed, equation (3.1) is somewhat symbolic. Making the Lorentz indices α_i and the colour indices a_i explicit by writing $\mathcal{J}_{\beta_i}(\Omega_i) = \mathcal{J}_i^{\alpha_i a_i}$, we have

$$\mathcal{V}(\omega_0,\beta_1\dots\beta_l)\mathcal{J}_{\beta_1}(\Omega_1)\dots\mathcal{J}_{\beta_l}(\Omega_l) = \sum_j c_j f_j(a_0,a_1,\dots,a_l) \Gamma_j^{\alpha_0\alpha_1\dots\alpha_l} \mathcal{J}_1^{\alpha_1 a_1}\dots\mathcal{J}_l^{\alpha_l a_l}, \tag{3.3}$$

where a summation over the Lorentz indices α_i is implicit. In equation (3.3), the coupling constant, the colour structure, and the Lorentz structure of the j-th vertex in the sum are denoted by c_j, f_j, and Γ_j, respectively. Along with the external wave functions $\mathcal{J}_{\omega_i}(\{\omega_i\})$ and the propagators P_{ω_i} these are the essential building blocks necessary to compute an arbitrary amplitude in this formalism.

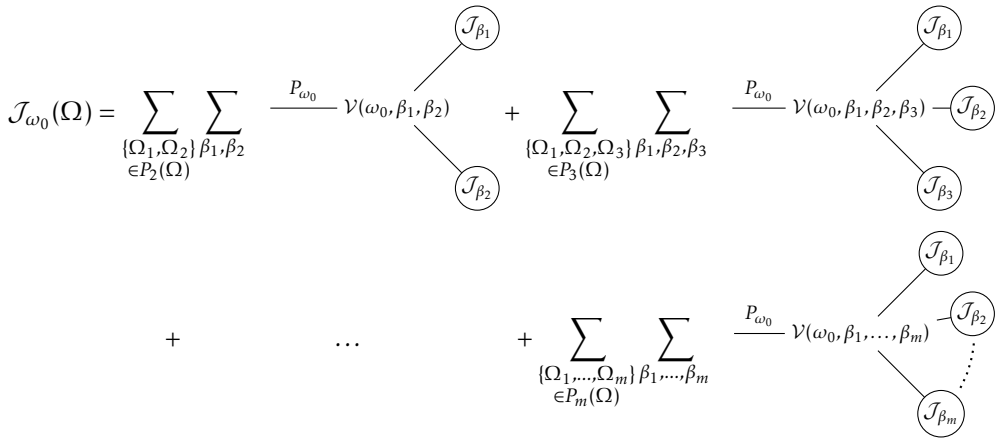

Figure 3.1: Diagrammatic illustration of the recursion relation (3.1). The summation over l in (3.1) is replaced by explicit example terms for $l = 2, 3, \ldots, m$. In this diagrammatic form it becomes intuitively clear that (3.1) is equivalent to a sum of all possible Feynman diagrams with external particles $\{\omega_0\} \cup \Omega$. In this sum, each diagram can be uniquely associated with one of the terms in the pictorial representation of (3.1) above.

3.3 Automatic Generation of Coupling Structures

As detailed in section 3.2, the basic building blocks required for the calculation of an amplitude in Comix are the external wave functions, propagators, Lorentz structures, colour structures, and of course the coupling constants. The number of relevant propagators and external wave functions in the UFO format is limited to those of spin-0, spin-1/2, spin-1, spin-3/2, and spin-2 fields. They can be implemented once and for all such that no automation is required. As of this writing, the corresponding expressions for spin 0, 1/2, and 1 are implemented in full generality in Comix. Spin-2 propagators are available as well but the corresponding external wave functions are not. It is left for future work to implement and validate spin-3/2 fields and the external wave functions for spin-2 particles.

Even when considering only fields of certain spin, there is no exhaustive list of Lorentz structures one could implement in order to capture all possible BSM couplings if one allows for non-renormalisable interactions. Effective theories which introduce such non-renormalisable interactions are being intensively studied at the LHC and an automated approach at implementing their Lorentz structures is therefore well motivated. In the UFO format, Lorentz structures are written symbolically in terms of the set of basic structures listed in table 3.1. Using these elementary structures, one can construct arbitrary Lorentz-

Name	Symbol
Dirac Matrices	$[\gamma^\mu]_{ab}$
Fifth Dirac Matrix	$[\gamma^5]_{ab}$
Charge Conjugation Matrix	$[C]_{ab}$
Kronecker Delta	$[\delta]_{ab}$
Chiral Projectors	$\left[\frac{1\pm\gamma^5}{2}\right]_{ab}$
Minkowski Metric	$\eta^{\mu\nu}$
Momentum of i-th Particle	p_i^μ
Pauli Matrices	$[\sigma^{\mu\nu}]_{ab}$
Antisymmetric Epsilon Tensor	$\epsilon^{\mu\nu\rho\theta}$

Table 3.1: Elementary Lorentz structures in UFO.

invariant products of fields with spin 0, 1/2, 3/2, and 2. In table 3.1, different types of indices were used for vector indices (Greek letters) and for spinor indices (a and b), as it is customary in physics. For the purpose of numerically evaluating expressions of the form (3.3), the nature of the indices is, however, completely irrelevant. Correspondingly, generic indices α_i will be used in the following. In this notation, the task of implementing a Lorentz structure into a generator that implements equation (3.1) reduces to generating computer code that, given the complex valued components of "incoming" currents $\mathcal{J}_i^{\alpha_i}$, evaluates expressions of the form

$$\mathcal{J}^{\alpha_0} = \Gamma^{\alpha_0\alpha_1\ldots\alpha_l}\mathcal{J}_1^{\alpha_1}\ldots\mathcal{J}_l^{\alpha_l}, \tag{3.4}$$

which represents an "outgoing" current with one uncontracted index α_0. This can be achieved as follows:

1. Assuming for now that a concrete representation of the Lorentz structure $\Gamma^{\alpha_0\alpha_1\ldots\alpha_l}$ in terms of complex numbers is given, one can obtain the functional form of the outgoing current's components in terms of the incoming currents by performing the multiplications and contractions of indices in (3.4) with symbolic expressions for the components of the incoming currents $\mathcal{J}_i^{\alpha_i}$. The resulting expressions can then be written into source code.

2. For this purpose, the Lorentz structure itself, $\Gamma^{\alpha_0\alpha_1\ldots\alpha_l}$, has to be calculated as a sum of products of fundamental Lorentz structures ζ_i as they appear in table 3.1. In a simple case where the number of external particles of the vertex under consideration is $l = 3$,

one can for example have

$$\Gamma^{\alpha_0\alpha_1\alpha_3} = \zeta_1^{\alpha_0\alpha_1\tilde{\alpha}}\zeta_2^{\tilde{\alpha}\alpha_3} = [\gamma^{\alpha_0}]_{\alpha_1\tilde{\alpha}}\left[\frac{1-\gamma^5}{2}\right]_{\tilde{\alpha}\alpha_3}. \tag{3.5}$$

Lorentz structures can of course be considerably more complex with sums of products of more than two elementary structures. Especially if the number of external particles at some vertex is large, the Lorentz structure can become intricate. At the same time, the form of their implementation is critical when considering performance. When taking expressions (3.4) along with (3.5) at face value, the number of multiplications involved can be extremely large. In a tree-level calculation, they constitute the critical bottle-neck of most implementations. Given a specific representation of the elementary structures in table 3.1 to be used, the contraction of repeated indices in (3.5) can however be performed explicitly in order to obtain a concrete representation of the tensor with uncontracted indices as required by the structure of the vertex.

For the purpose of addressing the above issues, a Python class has been developed that is capable of representing tensors as objects with an arbitrary number of indices. By supplementing this class with appropriate multiplication, addition and subtraction operators, one can explicitly evaluate the concrete representation of a Lorentz structure in the form of (3.5). Since the tensor class is designed to be completely agnostic to the type of values that the components of a tensor represent, it can also perform a multiplication with the symbolic external currents in (3.4) as long as an appropriate multiplication operator for the symbolic expressions themselves is provided.

In practice, concrete instances of this class representing the elementary structures in table 3.1 are first created. Their components are complex numbers that only depend on the representation of the matrices that are being used. Using these building blocks, an instance representing a composite Lorentz structure $\Gamma^{\alpha_0\alpha_1\ldots\alpha_l}$ can be created by means of sums of products of the form (3.5). Instances of the tensor class that represent the incoming currents in (3.4) are then created as well. They hold symbolic expressions representing the a priori unknown values of the respective components. The product of the external incoming currents and the Lorentz structure then gives the desired result (3.4) in terms of symbolic expressions, which can then be written into source code files, compiled and used for evaluation at runtime.

The order of tensor multiplications of course does not matter. The product objects representing the incoming currents in (3.4) can be evaluated first, yielding an object with l uncontracted indices. This object can then be multiplied with the Lorentz structure such that only one uncontracted index remains. Alternatively, the Lorentz structure can be successively multiplied with incoming currents, reducing the number of uncontracted indices one by one.

Name	Symbol
Kronecker Delta	$\delta_i^{\tilde{k}}$
Fundamental Representation matrices	$[T^a]_i^{\tilde{k}}$
Structure Constants	f^{abc}
Symmetric Tensor	d^{abc}
Antisymmetric Tensor	$\epsilon^{\tilde{k}\tilde{l}\tilde{m}}$, ϵ_{ijk}
Sextett Representation Matrices	$[T_6^a]_\alpha^{\tilde{\beta}}$
Sextett Clebsch-Gordon Coefficient	$(K_6)_\alpha^{\tilde{k},\tilde{l}}$
Anti-Sextett Clebsch-Gordon Coefficient	$(\tilde{K}_6)_{ij}^{\tilde{\alpha}}$

Table 3.2: Elementary Colour structures in UFO.

3.4 Optimisation of Lorentz Calculators for Massless Spinors

The products of external currents representing massless fermions often vanish for certain combinations of chiralities. For a vector-coupling to two fermionic currents of opposite chirality, for example, we have

$$[\overline{\mathcal{J}}_R]_i[\gamma^\mu]_{ij}[\mathcal{J}_L]_j = 0\,. \tag{3.6}$$

Furthermore, the chirality of an outgoing current can be determined from the chiralities of incoming currents for many interactions. In the Weyl representation used in Comix [139], a chiral spinor current has two vanishing components, which in do not need to be calculated if the chirality of the spinor is known in advance. Both of these circumstances can be exploited in order to optimise Lorentz calculator routines. For this purpose, fermionic currents are flagged according to their chirality. A Lorentz calculator routine can then check the chirality configuration of the incoming currents and immediately return zero if the product of the corresponding currents vanishes or it can skip the calculation of certain components of the outgoing currents if they are numerically zero anyways. This feature is implemented in the automatically generated Lorentz structures in a fully automated fashion. For this purpose, dedicated Lorentz calculators for all possible combinations of chiralities are written out and then called as appropriate at runtime. The dedicated Lorentz calculators are generated by setting components of incoming currents to zero according to their chirality. For the calculation of a partonic process of the form $q\bar{q} \to q\bar{q}q\bar{q}$, the performance gain achieved by employing the optimised Lorentz calculators is of the order of 40 %.

3.5 Colour Structures

The approach at generating Lorentz calculators presented in section 3.3 is sufficiently general to be applicable to the automatic generation of routines for colour structures as well. In UFO, they are given in terms of sums and products of the elementary structures listed in table 3.2. The problem of generating routines for colour structures therefore reduces to exactly the same problem as calculating the Lorentz structures of the form (3.5). At this point, this is however not being used in Sherpa because a fairly comprehensive set of colour structures is already implemented in Sherpa in a highly optimised fashion. This set covers the entire MSSM but does not allow for the calculation of cross sections in models containing arbitrary higher dimensional operators of strongly interacting particles. The incorporation of automatically generated and optimised colour calculators is, however, planned for the near future.

3.6 Other Aspects of the Interface

Since a UFO model comes in the form of a Python module, it is most conveniently processed through a Python interpreter. Correspondingly, the process of making a UFO model available for event generation in Sherpa proceeds through a Python executable. This executable imports the UFO model, extracts the information on the particle content, free parameters, and their relation to the particle properties and couplings. A C++ model implementing the corresponding relations is then written out along with the Feynman rules that specify the interactions in the model. Subsequently, the Lorentz routines are generated and written out. The source code is then compiled and linked into a dynamic library to be loaded automatically at runtime if the respective model is requested. Model parameters can be specified in a syntax that is fully compliant with the UFO standard either in the run card or in an external file.

With the BSM model available to Sherpa, fixed-order differential cross sections can be calculated. Due to limited computing resources, it is in practice sometimes not feasible to calculate the differential cross sections of interest at the level of stable final state particles. In many BSM models, this is due to the appearance of multiple heavy intermediate resonances that decay through long decay chains, emitting large numbers of particles and thereby leading to high-multiplicity final states. In a narrow-width-approximation [140] this problem is avoided by factorising the differential cross section into matrix elements for the production of unstable resonances and matrix elements for their decay, thus discarding any non-factorising contributions. Non-factorising contributions typically become small if the total width of the resonance is small compared to its mass and if the decay daughter particles are

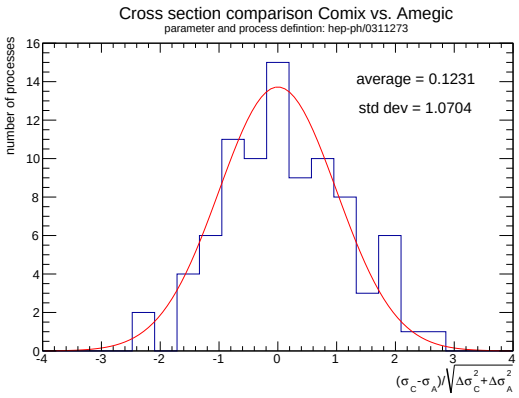

Figure 3.2: Deviation between results from Amegic and Comix for the 86 $e^+e^- \to 6f$ processes listed in reference [144], using the parameters given ibidem. The red curve represents a normal distribution and should be considered the reference.

much lighter than the decaying resonance, thus rendering the narrow-width-approximation appropriate. In this approach, events can be simulated by generating fixed-order events for the production of intermediate resonances according to the corresponding on-shell production matrix elements. The decay chains of unstable resonances are then simulated in accordance with decay matrix elements step by step. An algorithm implementing the simulation of decay chains in this manner is implemented in Sherpa [1]. Spin correlations between the production and the decay of resonances can be recovered by means of the algorithm proposed in reference [141]. The building blocks for the decay algorithm with spin correlations are the same as for usual matrix elements. It can thus be employed in a fully automatised way for any BSM model that is supported by the UFO interface.

All other modules of Sherpa that are necessary for the simulation of events at the hadron level are seamlessly integrated with UFO models as well. This includes the parton shower, leading order merging techniques, the hadronisation model, and the underlying event simulation. Since these steps of the simulation implicitly assume the Standard-Model, the particle content of the SM along with SM QCD interactions must be present in the BSM model for the additional simulation steps to be applicable. In the context of multi-jet merging in BSM models, it is often necessary to amend the merging of matrix elements and parton showers with the requirement that no new resonances be present at higher multiplicity. This can be achieved in Sherpa using a diagram filter, corresponding to the diagram-removal method described in references [142, 143].

Model	number of processes tested	max. rel. deviation Comix ↔ MadGraph5
Standard Model	60	$2.3 \cdot 10^{-10}$
Higgs Effective Field Theory	13	$4.3 \cdot 10^{-13}$
MSSM	401	$1.0 \cdot 10^{-10}$
Minimal Universal Extra Dimensions	51	$2.8 \cdot 10^{-12}$
Anomalous Quartic Gauge Couplings	16	$5.9 \cdot 10^{-12}$

Table 3.3: Maximal relative deviations between squared tree-level matrix elements computed with Comix and MadGraph5. For each model, the largest observed deviation among all processes and all 1000 random phase-space points is quoted.

3.7 Validation

The incorporation of the features discussed above required a considerable adaption of existing code in Comix. A re-validation of Standard Model calculations is hence necessary. For this purpose, 86 leading order cross sections for the e^+e^--collider processes listed in reference [144] were calculated with a Monte Carlo uncertainty of less than 5 ‰ both with Comix and with Amegic. All tested processes feature six particle final states. Figure 3.2 shows the distribution of relative deviations of cross sections computed with the two generators. It can be seen that the deviations between the two generators are compatible with purely statistical fluctuations within the Monte Carlo uncertainties. This confirms the correct implementation of the Standard Model in the extended version of Comix and it validates the recursive phase-space generator of Comix [40].

In order to thoroughly test both the interface to the UFO format and the automatically generated Lorentz structures, a comparison of squared matrix elements evaluated at random phase space points was performed additionally. As a numerical reference program, MadGraph5 was used. In addition to the Standard Model, effective theories that feature more complicated Lorentz structures were considered. The Higgs Effective Field Theory Model is based on the Standard Model and includes couplings of a scalar and a hypothetical pseudoscalar Higgs boson to gluons via a top-quark loop (see chapter 4 and references [145–147] for more details). This theory involves up to five-point vertices. Additionally, a model for anomalous quartic gauge couplings [148–150] was used for the tests. This model implements the interaction terms (A7) - (A10) of reference [151]. They extend the gauge sector of the Standard model with vertices connecting up to eight external particles. Processes with four and six external particles were tested, thus validating automatically generated Lorentz structures of effective six-particle vertices. In order to ensure a correct treatment of Majorana fermions, the Minimal Supersymmetric Standard Model was invoked. In this model, the

Figure 3.3: Example decay chain for a pair of squarks.

comprehensive set of processes considered in [123] was tested. To further extend the range of tested models, the processes listed in reference [118] for the Minimal Universal Extra Dimensions Model [152] were tested as well. The test of the Standard Model processes listed in [118] was supplemented with additional $2 \to 2$, $2 \to 3$, and $2 \to 4$ processes.

For each process in the various models, 1000 random phase space points were generated for the evaluation of squared matrix elements both with Comix and with MadGraph5. Table 3.3 lists, for each model, the maximum of relative deviations between the two squared matrix elements that were observed among all tested processes and all phase space points. Excellent agreement between Comix and MadGraph5 is found throughout. In order to validate the spin correlated decay chain simulations of Sherpa in the context of BSM models, the pair production and subsequent decay of squark pairs in the MSSM was analysed in more detail. In the MSSM, a pair of up-type squarks can decay along the chain depicted in figure 3.3, leading a collider signature of the form

$$pp \to \tilde{u}\bar{\tilde{u}} \to d\,\chi_1^0\,\mu^+\,\nu_\mu\,\bar{u}\,e^+\,e^-\,\chi_1^0. \tag{3.7}$$

Figure 3.4 shows two-particle invariant mass distributions in this final state that are sensitive to spin correlations in the decay chain. For generating the technical validation results shown here, the SPSP1a benchmark model parameter point [153] was used. Results for three types of simulation are shown:

Full ME The full $pp \to d\,\chi_1^0\,\mu^+\,\nu_\mu\,\bar{u}\,e^+\,e^-\,\chi_1^0$ reaction is generated as a hard process with a restriction to the resonant diagrams shown in figure 3.3. This automatically includes all spin correlations and is thus to be considered the reference.

Correlated decays The $pp \to \tilde{u}\bar{\tilde{u}}$ process is generated as a hard scattering reaction with a subsequent factorised simulation of the decay chain shown in figure 3.3 and with spin correlations taken into account

Uncorrelated decays As above, but with spin-correlations disabled.

As demonstrated in the lower panels of figure 3.4, the simulation using the spin-correlated factorised decay treatment is, within the statistical uncertainties, in excellent agreement with

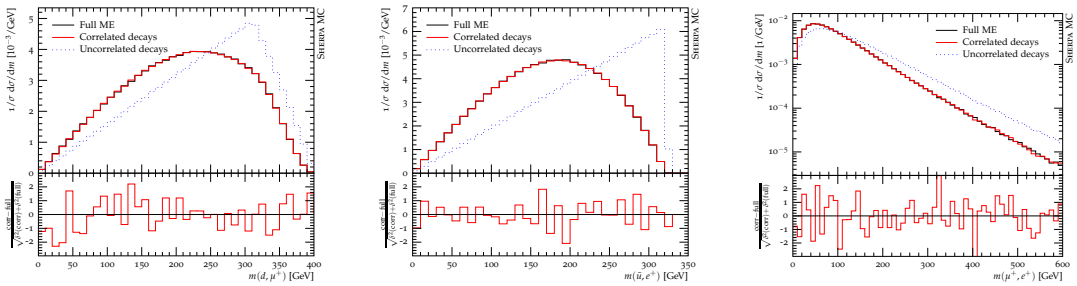

Figure 3.4: Spin-correlation effects in the decay cascade following squark pair production in the MSSM. The three simulation setups are described in the main text. The ratio plots display the relative differences in terms of the statistical uncertainty.

the full ME simulation. This comparison completes the validation of the fixed-order matrix element aspects of event generation with UFO BSM models in Sherpa.

3.8 Conclusions

In this work, a new method for the fully automatised implementation of generic new-physics models into the event generator Sherpa based on the Universal FeynRules Output format was described. This Monte Carlo generator independent BSM model output format is supported by multiple Feynman rule generators and is being adopted by an increasing number of matrix element generators. As part of the new UFO support, a new automatic generator for Lorentz calculators was introduced. It allows to implement arbitrary Lorentz structures and is, in its functionality, equivalent to the Aloha package [154]. The matrix-element generator Comix was adapted accordingly, such that arbitrary higher-point Lorentz functions can be used for amplitude generation.

The new and extended version of Comix described here, together with the newly constructed decay module of Sherpa, allows to compute the production and decay of BSM particles, with spin correlations in the decay taken into account. The simulations can be embedded in the larger event generation framework of Sherpa to also include QCD radiative corrections by means of the parton shower and multi-jet merging. Non-perturbative effects can be accounted for through cluster hadronisation, hadron decays, and underlying event simulation. Overall, a complete framework to address many new-physics simulations in a fully automated way was presented. Currently, the implementation is restricted to spin-0, spin-1/2 and spin-1 particles, and to the colour structures of the MSSM. The addition of higher-spin states and a fully automatised treatment of arbitrary colour structures is foreseen for the near future and currently under active development.

The fixed-order aspects of event generation were thoroughly validated in this work. The

validation tests based on squared matrix elements have been fully automated and are now being used for continuous validation within Sherpa. The list of processes and models in the tests gets extended as new models are being considered by the authors.

4 Heavy Quark Mass Effects in Gluon Fusion Higgs Production

As all other particles in the standard model, the proton constituent quarks and gluons couple directly to the Higgs via tree-level couplings that are proportional to their respective masses. Therefore, all of these couplings are small compared to the ones of heavy gauge bosons or the top quark. This applies to the gluon as well as the light quark flavours u, d, c, s, and the b. As a consequence, the phenomenologically relevant Higgs production mechanisms at the LHC proceed through intermediate heavy gauge bosons or intermediate top quarks [155]. By far the most dominant production mode is due to heavy quark loops that couple to initial state gluons as well as the Higgs, thereby mediating an interaction to the initial state partons. The type of Feynman diagram that contributes at leading order to the *gluon fusion* mechanism is depicted in figure 4.1. Because there are no tree-like diagrams for the partonic process $gg \to H$, it is referred to as being *loop-induced*.

The presence of closed massive quark loops already in the lowest-order diagrams of the gluon fusion process renders even a leading order calculation cumbersome. At the same time, higher order corrections to this process are particularly large. Commonly employed approximations neglect the loop structure of the Higgs-gluon interactions entirely, thus facilitating higher order calculations. Although this approximation has proven to yield reasonably accurate results for very inclusive observables, it is known to fail in certain kinematic regimes.

The aim of the work presented in this chapter is to improve upon the usual approximation in such a way as to still capture higher order effects in an approximate fashion. This chapter is also concerned with BSM physics effects that might alter the loop structure which mediates

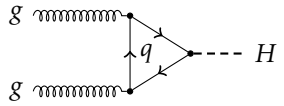

Figure 4.1: Leading order diagram for the gluon fusion Higgs production process. Any quark q in principle contributes with a diagram of this form, but the top quark contribution is by far the largest, due its large Yukawa coupling y_t.

the Higgs-gluon coupling and addresses the question whether one can exploit the event kinematics in Higgs production at the LHC in order to establish whether or not such BSM physics exists.

4.1 Higgs Effective Field Theory

The complexity of the gluon fusion process can be considerably reduced by by employing a *low-energy theorem* [145–147]. This theorem is applicable in the limit where the centre-of-mass energy is much lower than the mass of the heavy quarks in the loops, such that its validity is restricted to the top quark contributions at the LHC. By means of the low-energy-theorem, these contributions can be obtained from an effective Lagrangian that describes the interactions between gluons and the Higgs boson in terms of direct couplings [156, 157]

$$\mathcal{L}_{\text{HEFT}} = \frac{\alpha_s}{12\pi} G^a_{\mu\nu} G_a^{\mu\nu} \ln\left(1 + \frac{H}{v}\right) \tag{4.1}$$

$$= \frac{\alpha_s}{12\pi} G^a_{\mu\nu} G_a^{\mu\nu} \left[\left(\frac{H}{v}\right) - \frac{1}{2}\left(\frac{H}{v}\right)^2 + \frac{1}{3}\left(\frac{H}{v}\right)^3 - \dots\right]. \tag{4.2}$$

In what follows, the approximate description in terms of the Lagrangian (4.2) will be referred to as the *Higgs effective field theory (HEFT)* approximation. The first term in the expanded expression (4.2) gives rise to the Feynman diagrams depicted in figure 4.2. Because the Higgs-gluon-interactions as described by (4.2) are mediated by direct couplings, the complexity of the process is effectively reduced to a level that is comparable to that of an ordinary process which proceeds through tree-level diagrams at leading order. Many well established calculational tools for the computation of higher-order corrections can hence be applied in a straightforward manner with little or no modification in this framework.

The total gluon fusion Higgs production cross section in the HEFT approximation was calculated at NLO in [158, 159]. The α_S^3 contributions give rise to corrections of relative size around 100 %. Only the subsequently preformed NNLO calculations [160–162] showed indications of a convergence of the perturbative expansion with an overlap of error bands between the NLO and NNLO calculation but scale variation uncertainties still being of the order of ±10%. With the N^{3}LO calculation of references [163–165] , perturbative uncertainties were eventually reduced to a level below ±5 %.

4.2 Validity of the HEFT Approximation

The total inclusive Higgs production cross section at the LHC is known to be well approximated when calculated in the HEFT framework. The correction one obtains by calculating

the cross section in the full Standard Model (heavy quark mass corrections, as they will be referred to in what follows) remain moderate. Taking into account only the top quark contributions, they amount to 5 % at leading order and remain at the percent-level when going to NLO [166–168] and NNLO [169–174] in α_s. The bottom quark loops, which are entirely neglected in the HEFT, give rise to negative corrections to the total cross section of the order of 5% [175], thus approximately compensating for the finite top quark mass corrections. Contributions due to loops of charm quarks contribute a mere 0.5 % [175] to the total cross section and will not be considered in what follows.

As mentioned previously, the effective Lagrangian (4.2) is derived from a low-energy limit in which the centre-of-mass energy is assumed to be smaller than the top quark mass. Despite the heavy quark mass effects being small for the inclusive cross section, the HEFT approximation therefore completely fails to describe kinematic regimes in which the partonic centre-of-mass energy exceeds m_t. Collider signatures of such configurations include the production of a Higgs boson at large transverse momentum [176–179] as well as events with a large invariant mass of the Higgs decay products, commonly referred to as off-shell Higgs production [180–182]. The tails of the invariant mass distribution and the Higgs transverse momentum distribution are therefore poorly described in the HEFT. In the $gg \to Hg$ channel, the heavy quark mass dependence of the matrix element in the limit of large Higgs transverse momenta, $p_T \gg m_H, m_q$, is given by

$$\mathcal{M} \propto \frac{m_q^2}{p_T}\left[A_0 + A_1 \ln\left(\frac{p_T^2}{m_q^2}\right) + A_2 \ln^2\left(\frac{p_T^2}{m_q^2}\right)\right], \tag{4.3}$$

with A_i independent of m_q [179]. In the HEFT approximation, the corresponding relation reads

$$\mathcal{M} \propto p_T\,, \tag{4.4}$$

with no dependence on the heavy quark mass [179]. As is evident from equations (4.3) and (4.4), the transverse momentum spectrum will be overestimated when using the HEFT approximation for $p_T \gg m_q$.

By contrast, the effects of bottom quark loops in the transverse momentum distribution are restricted to small values of p_T [177, 178, 183]. This is due to the behaviour of the matrix elements in the limit $p_T, m_H \gg m_q$, where the dependence on top heavy quark mass is given by [176]

$$|\mathcal{M}|^2 \propto m_q^4 \ln^4\left(\frac{m_q^2}{p_T^2}\right) \to 0\,. \tag{4.5}$$

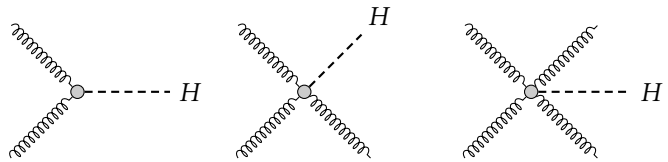

Figure 4.2: Pictorial representation of the Feynman rules of the terms of the effective Lagrangian (4.2) that involve only one power of the Higgs field.

Relation (4.5) is valid for all partonic channels and implies that the tail of the transverse momentum distribution is dominated by the top quark contributions. The effects of bottom quark contributions are sizeable in the region of $p_T \approx m_b$, however [178, 183]. The leading contribution involving bottom quarks is an interference term proportional to $y_t y_b$ and it does therefore not only involve the bottom quark. In what follows, any contribution involving y_b will nonetheless be referred to as a bottom quark contribution. Bottom quark effects combined with those of a finite top quark mass will be referred to as heavy quark mass effects.

4.3 Implementation of Heavy Quark Mass Corrections

Several fully differential Monte Carlo programs for inclusive Higgs boson production have been developed that work in the infinite top mass limit at NNLO in QCD. Among them are FEHiP [184], HNNLO [185, 186], as well as a dedicated implementation in Sherpa [187]. Fully differential NLO calculations for Higgs production in association with at least one jet in the HEFT approximation have been presented in [188–191]. The corresponding results for two and three jets were calculated in [192] and [193, 194], respectively.

As mentioned in section 4.2, finite heavy quark mass effects on the total inclusive cross section have been studied at NNLO accuracy [169–174]. Differentially, these effects are only known to NLO accuracy. They have been implemented in various fully differential Monte Carlo programs [183, 195–197]. For Higgs production in association with one, two, or more jets, the heavy quark mass effects are only known at leading order [176–178, 198]. Theoretical uncertainties on the Higgs transverse momentum distribution are correspondingly large since a nonzero Higgs p_T in gluon fusion is necessarily induced by QCD jet emissions. NLO calculations of these processes for finite top quark masses are presently not available due to the missing two-loop virtual corrections.

However, finite top mass effects have been studied in an approximate fashion at NLO for the one-jet final state in [199], where it was found that the effects on the Higgs differential distributions approximately factorise from the NLO QCD corrections. To a good approx-

imation, one can therefore recover finite top quark mass effects by reweighting the NLO prediction obtained in the HEFT with leading order top mass correction factors according to the prescription

$$\langle\mathcal{O}\rangle_{\mathrm{NLO}} = \langle\mathcal{O}\rangle^{\mathrm{HEFT}}_{\mathrm{NLO}} \times \frac{\langle\mathcal{O}\rangle_{\mathrm{LO}}}{\langle\mathcal{O}\rangle^{\mathrm{HEFT}}_{\mathrm{LO}}}\,. \tag{4.6}$$

This observation is the key motivation for the implementation of finite top quark mass corrections as it will be presented in what follows. Implementing the reweighting in equation (4.6) in a differential and observable-independent way is however not trivial. Writing the reweighting factor in terms of cross sections, we have

$$\begin{aligned}\frac{\langle\mathcal{O}\rangle_{\mathrm{LO}}}{\langle\mathcal{O}\rangle^{\mathrm{HEFT}}_{\mathrm{LO}}} &= \frac{\int \mathrm{d}\sigma^{\mathrm{LO}}/\mathrm{d}\phi_B}{\int \mathrm{d}\sigma^{\mathrm{LO}}_{\mathrm{HEFT}}/\mathrm{d}\phi_B}\theta\left(|\mathcal{O}(\phi_B)|\right)\mathrm{d}\phi_B \\ &\approx \int \frac{\mathrm{d}\sigma^{\mathrm{LO}}/\mathrm{d}\phi_B}{\mathrm{d}\sigma^{\mathrm{LO}}_{\mathrm{HEFT}}/\mathrm{d}\phi_B}\theta\left(|\mathcal{O}(\phi_B)|\right)\mathrm{d}\phi_B = \int \frac{B(\phi_B)}{B_{\mathrm{HEFT}}(\phi_B)}\theta\left(|\mathcal{O}(\phi_B)|\right)\mathrm{d}\phi_B\,.\end{aligned} \tag{4.7}$$

In going from the first to the second line of (4.7), it was assumed that (4.6) also holds differentially. This allows one to incorporate the correction on on an event-by-event basis for the terms with born kinematics. The real-emission terms, however, would have to be reweighted by a non-local and observable-dependent factor:

$$\begin{aligned}\langle\mathcal{O}\rangle_{\mathrm{NLO}} &= \int (B+V+\mathcal{I})\mathcal{O}(\phi_B)\,\mathrm{d}\phi_B + \int\left[R(\phi_R)\mathcal{O}(\phi_R) - \sum D^k_{ij}(\phi_B,\phi_1)\mathcal{O}(\phi_B)\right]\mathrm{d}\phi_R \\ &\approx \Bigg[\int (B+V+\mathcal{I})^{\mathrm{HEFT}}\mathcal{O}(\phi_B)\,\mathrm{d}\phi_B \\ &\quad + \int\left[R(\phi_R)\mathcal{O}(\phi_R) - \sum D^k_{ij}(\phi_B,\phi_1)\mathcal{O}(\phi_B)\right]^{\mathrm{HEFT}}\mathrm{d}\phi_R\Bigg] \times \frac{\langle\mathcal{O}\rangle_{\mathrm{LO}}}{\langle\mathcal{O}\rangle^{\mathrm{HEFT}}_{\mathrm{LO}}} \\ &= \int (B+V+\mathcal{I})\frac{B}{B^{\mathrm{HEFT}}}\mathcal{O}(\phi_B)\,\mathrm{d}\phi_B \\ &\quad + \int\left[R(\phi_R)\mathcal{O}(\phi_R) - \sum D^k_{ij}(\phi_B,\phi_1)\mathcal{O}(\phi_B)\right]^{\mathrm{HEFT}}\mathrm{d}\phi_R \times \frac{\langle\mathcal{O}\rangle_{\mathrm{LO}}}{\langle\mathcal{O}\rangle^{\mathrm{HEFT}}_{\mathrm{LO}}}\,,\end{aligned} \tag{4.8}$$

where the notation of chapter 2 was used and some of the obvious phase arguments were suppressed.

However, when taking into account the full heavy quark mass dependence, the real-emission terms as well as their their subtraction terms still only depend on one-loop diagrams. The corresponding matrix elements are available through the automatised loop provider OpenLoops [44] and can be evalueated efficiently with Collier [49, 50]. Using these matrix elements, real-emission terms can therefore also be reweighted in such a way as to correct the

last line in (4.8) for finite top mass corrections without any further approximation according to

$$\begin{aligned}\langle\mathcal{O}\rangle_{\mathrm{NLO}} \approx &\int (B+V+\mathcal{I})^{\mathrm{HEFT}} \frac{B}{B^{\mathrm{HEFT}}}\mathcal{O}(\phi_B)\,\mathrm{d}\phi_B \\ &+\int \Big[R(\phi_R)\mathcal{O}(\phi_R) - \sum D_{ij}^k(\phi_B,\phi_1)\mathcal{O}(\phi_B)\Big]\mathrm{d}\phi_R\,. \end{aligned} \tag{4.9}$$

This approach comes with the additional benefit that the any contribution from a real emission correction comes with the exact leading order heavy quark mass dependence. The Higgs transverse momentum spectrum in an NLO calculation of inclusive Higgs production is therefore leading order accurate in this approach and comes with the exact heavy quark mass dependence. Only observables that receive contributions from the born-like terms in the first line of (4.10) will be affected by the ad-hoc approximate treatment of virtual corrections.

In principle, one could compute the terms B, $\mathcal{I}$, R, and $\mathcal{D}$ (the tree-level terms in the HEFT approximation) using the appropriate one-loop matrix elements from the start, such that no reweighting would be necessary. The implementation of the corrections as an a posteriori reweighting is, however, much simpler in the Sherpa framework. The real-emission terms are hence calculated schematically according to

$$\begin{aligned}&\int \Big[R(\phi_R)\mathcal{O}(\phi_R) - \sum D_{ij}^k(\phi_B,\phi_1)\mathcal{O}(\phi_B)\Big]\mathrm{d}\phi_R \\ &= \int \left[\frac{|\mathcal{M}_R|^2}{|\mathcal{M}_R^{\mathrm{HEFT}}|^2}R(\phi_R)\mathcal{O}(\phi_R) - \sum \frac{|\mathcal{M}_B|^2}{|\mathcal{M}_B^{\mathrm{HEFT}}|^2} D_{ij}^k(\phi_B,\phi_1)\mathcal{O}(\phi_B)\right]\mathrm{d}\phi_R \end{aligned} \tag{4.10}$$

In this approach, each matrix element needs to be evaluated at least twice, once in the HEFT approximation and once as an m_t-exact one-loop matrix element. The computational cost of the additional evaluation of the tree level matrix element is, however, negligible in comparison with the evaluation of the one-loop matrix element, which is necessary in any case.

It should be stressed at this point that the approximate NLO treatment of finite top quark mass effects cannot be employed in order to incorporate bottom quark contributions. The approximation (4.6) is based on the calculation of α_S-corrections in an effective low-energy approximation. An effective treatment of the bottom quark contributions is, however, not applicable since the bottom mass is much smaller than the partonic centre-of-mass energy necessary to produce a Higgs boson. In what follows, bottom quark contributions will therefore be calculated at leading order. This applies to the interference terms proportional to $y_t y_b$ as well as the squared bottom contributions proportional to y_b^2. The necessary

decomposition of matrix elements into contributions proportional to y_t^2 and contributions proportional to either $y_t y_b$ or y_b^2 has been implemented in OpenLoops for this purpose. The NLO corrections to the total inclusive cross sections for the $y_t y_b$ contributions and the y_b^2 contributions are only of the order of 1 % and 20 %, respectively, such that a leading order treatment is in fact appropriate [200]. The y_b^2 contributions featuring the slightly larger NLO K-factor are also significantly suppressed compared to the $y_t y_b$ terms [200].

It is also worth noting that the implementation of parton shower matching and multijet merging techniques in Sherpa is completely agnostic to the details of the fixed-order scattering process being considered. Having implemented and validated the heavy quark mass corrections at the level of fixed-order calculations, one can therefore directly apply these methods.

4.4 Validation of the Implementation

In the approach outlined in section 4.3, the real emission and subtraction terms in (4.10) are reweighted using matrix elements of different final state multiplicity. Any error in the correct implementation of the reweighting procedure would spoil the cancellation of soft and collinear divergences in the NLO subtraction. The mere convergence of the integral in (4.10) therefore provides a stringent check of the implementation. The convergence of the cross section calculation for inclusive Higgs production and Higgs production in association with one jet at NLO was explicitly checked.

As previously mentioned, heavy quark mass effects have been implemented at NLO in publicly available tools for the inclusive Higgs production process. The accuracy of the approximate treatement of virtual corrections inherent to (4.9) can therefore be quantitatively assessed through this process. For this purpose, the numerical program HNNLO version 2.0 was employed [183, 185, 201]. Finite heavy quark mass effects are implemented in this program without any approximations at NLO accuracy. Figure 4.3a shows the total inclusive NLO cross section for inlcusive Higgs production obtained with this program, both in the HEFT approximation and with finite top mass effects taken into account. For comparison, the corresponding results obtained with Sherpa in the approximation (4.9) are shown as well. The relative difference between the approximate result and the exact treatment is below 0.5 % and completely negligible compared to the perturbative uncertainties estimated by the conventional scale variations of factors of two up and down.

Figure 4.3b shows the Higgs transverse momentum distribution obtained from fixed order calculations with HNNLO and Sherpa with finite top mass effects taken into account. The p_T distributions are obtained from an NLO calculation of the inclusive Higgs production process and are therefore leading order accurate. Within the small statistical uncertainties,

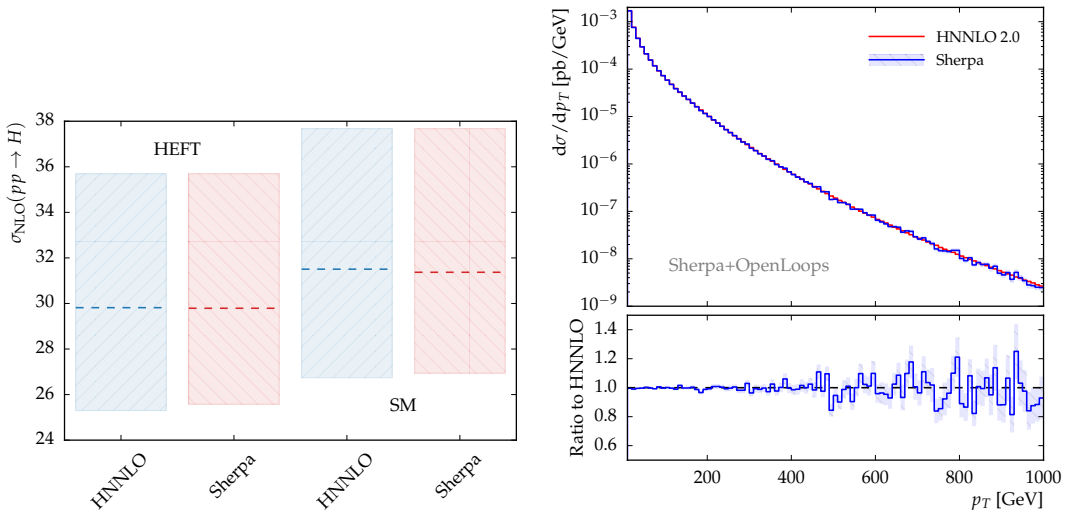

(a) The total inclusive cross section in the HEFT approximation and with the top mass dependence taken into account (SM). The uncertainty bands are obtained from independent variations of the factorisation and renormalisation scale by factors of two up and down.

(b) Higgs transverse momentum in the diphoton decay channel as obtained from HNNLO and from Sherpa using the implementation of finite top quark mass corrections presented here. The uncertainty bands indicate statistical uncertainties only.

Figure 4.3: Validation of the fixed-order NLO calculation of inclusive Higgs production through gluon fusion at the LHC with $\sqrt{s} = 13\,\mathrm{TeV}$ against HNNLO. Factorisation and renormalisation scales are set to $\mu_{F/R} = m_H$.

an excellent agreement can be observed. Note that agreement within statistical Monte Carlo uncertainties is to be expected as a consequence of the m_t-exact treatment of real-emission corrections inherent to the implementation presented here (see equation (4.10)). One can of course obtain the transverse momentum spectrum shown in figure 4.3b by performing a leading order calculation of Higgs production in association with a jet. Having calculated the distribution in an NLO calculation of inclusive Higgs production, however, also validates the implementation of heavy quark mass effects in the NLO subtraction procedure with its interplay between real-emission and subtraction terms expressed in equation (4.10).

4.5 Finite Top Mass Effects

As is evident from the comparison of NLO cross sections in figure 4.3a, the total inclusive Higgs production cross section is only mildly affected by finite top mass effects. This is also the case for one-, two-, and three-jet inclusive cross sections which are shown, at leading order, in table 4.1. The region of low Higgs transverse momenta, where the bulk of the cross section

	H	Hj	Hj^2	Hj^3
HEFT	13.33 pb	7.69 pb	3.67 pb	1.68 pb
SM	14.22 pb	8.10 pb	3.74 pb	1.51 pb

Table 4.1: Leading order inclusive cross sections for Higgs boson boson production in association with $n = 0, 1, 2, 3$ jets at the LHC for $\sqrt{s} = 13\,\text{TeV}$ based on the m_t-exact calculation (SM) and the HEFT approximation. Jets are reconstructed using the anti-k_T algorithm with $R = 0.4$ and a minumum transverse momentum of 30 GeV. Factorisation and renormalisation scales were set to the Higgs mass in the calculation.

in inclusive Higgs production is located, can therefore be expected to exhibit only a moderate dependence on the top quark mass. In regimes where a kinematic invariant significantly exceeds m_t, however, the HEFT approximation can be expected to break down. The p_T distributions in figure 4.4a confirm this picture. The Higgs boson transverse momentum distributions for final states with one, two, and three jets calculated at fixed leading order are shown. For this purpose, jets are reconstructed using the anti-k_T algorithm [202] with a radius parameter of $R = 0.4$ and a minimum jet transverse momentum of 30 GeV, except for the 1-jet case, where only a small minimum p_T-cut of 1 GeV was applied in order to be able to show the distribution down to small values of p_T. The distributions for all three jet multiplicities exhibit a very similar pattern when comparing the full SM result to the HEFT approximation. Below $p_T \approx m_H$, a flat excess of around 6 % that recovers the correction factor to the total inclusive Higgs production cross section at leading order can be observed. The deviations become very large when p_T significantly exceeds m_t, as expected. The similarity of the top mass dependence of the p_T spectrum for all jet final multiplicities confirms similar observations for one- and two-jet configurations made by the authors of reference [203].

As stated previously, the implementation of heavy quark mass effects allows for the parton shower matching and for performing multijet merged calculations at NLO. In a merged calculation, the intra-jet dynamics of soft and collinear radiation is modelled by the parton shower, whereas the kinematics of hard jets is described by the appropriate matrix elements at leading order or at NLO. Currently, one-loop matrix elements for up to three jets in the final state are available through OpenLoops and can be evluated reasonably quickly, allowing for merged calculations that include NLO matrix elements for zero, one, and two jets in the final state. Figure 4.4b shows the Higgs transverse momentum distribution obtained from a merged calculation with NLO matrix elements for zero and one jet in the final state as well as LO matrix elements for two jets in the final state taken into account with Q_{cut} set to 30 GeV. Individual curves for events with one, two and three jets in the final state are shown in the plot. From the ratio plot in figure 4.4b it is evident that in our approximation we

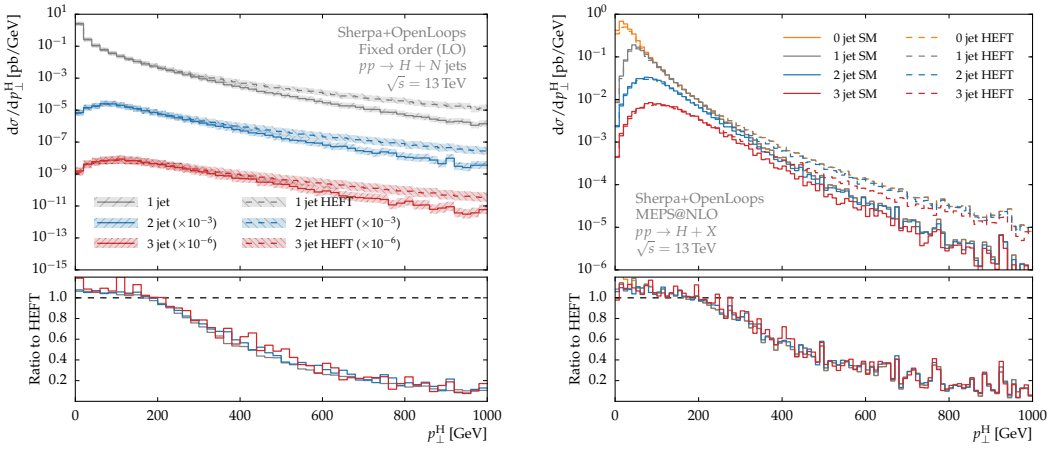

(a) LO fixed order calculation for up to three jets. The error bands indicate variations of the factorisation and renormalisation scales.

(b) Multijet merged calculation. The zero- and one-jet final states are included at NLO along with the two jet final state at leading order. The individual curves show inclusive N-jet contributions.

Figure 4.4: The Higgs transverse momentum spectrum in gluon fusion. Individual curves for the HEFT approximation (dashed) and the full SM result taking into account the mass dependence in the top quark loops are shown. The lower panels show the ratio of the SM results to the respective HEFT approximations.

recover the same suppression patterns as in the respective fixed leading order calculations for all jet multiplicities. This is a nontrivial observation as an m-jet configuration receives corrections from m-jet matrix elements as well as from $m+1$-jet matrix elements through the real emission corrections R in (4.9). A factorisation in the form of equation (4.6) is therefore recovered despite the non-facorised application of heavy quark mass effects in phase spaces of different final state multiplicities.

This factorisation in a merged calculation can be further quantified in terms of the differential NLO K-factor

$$K(p_\perp) = \frac{\mathrm{d}\sigma_{\mathrm{NLO}}/\mathrm{d}p_T}{\mathrm{d}\sigma_{\mathrm{LO}}/\mathrm{d}p_T}\,. \tag{4.11}$$

The label "NLO" in (4.11) indicates that zero and one-jet matrix elements are included at NLO in the calculation whereas "LO" indicates that only LO matrix elements were used for those final states. Two-jet configurations are understood to be described at LO accuracy in both setups. Figure 4.5 shows the differential NLO K-factor both in the HEFT approximation and with finite top mass effects taken into account. As demonstrated in this figure, the ap-

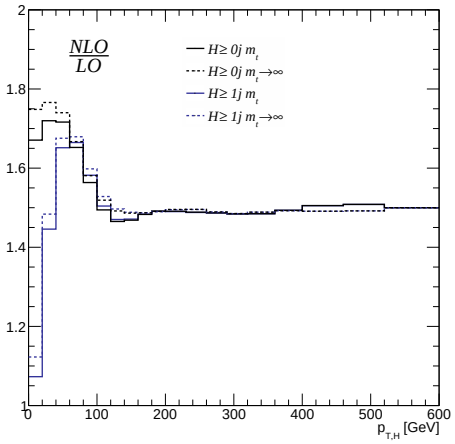

Figure 4.5: Differential NLO K-factor as defined in equation (4.11) in a fully inclusive sample and in jet-inclusive sub-samples. Dashed curves show results in the HEFT approximation (labelled $m_t \to \infty$ in this plot) and solid curves show results of a calculation with finite top mass effects taken into account (labelled m_t in this plot).

proximate treatment of top mass effects at NLO preserves the qualitative features of the NLO K-factor as a function of the Higgs transverse momentum. For transverse momenta above roughly the Higgs mass, the differential K-factor is near identical in the HEFT approximation and in the simulation that takes into account finite top mass effects. These effects therefore factorise to a very good approximation from the α_s corrections in this regime.

4.6 Bottom Quark Effects

As pointed out already in [177, 178], the inclusion of the bottom quark in the loops affects the p_T distribution only at small values of p_T near m_b. In figure 4.6 these findings are reproduced by means of a fixed order calculation of the process $pp \to H + j$. In the p_T range around m_b, where the bottom effects are large, a fixed order prediction is, however, unreliable due to the large hierarchy of scales between m_H and the transverse momentum. This large separation of scales induces Sudakov logarithms of the form $\ln(m_H/p_T)$ that spoil any fixed order expansion and require resummation. In a Monte Carlo simulation, this resummation can be achieved by means of a parton shower algorithm.

It was argued by the authors of [183] that the resummation of these logarithms is complicated by the presence of the bottom quark in loops that couple to the Higgs boson. The bottom quark introduces m_b as an additional scale above which the matrix elements for additional

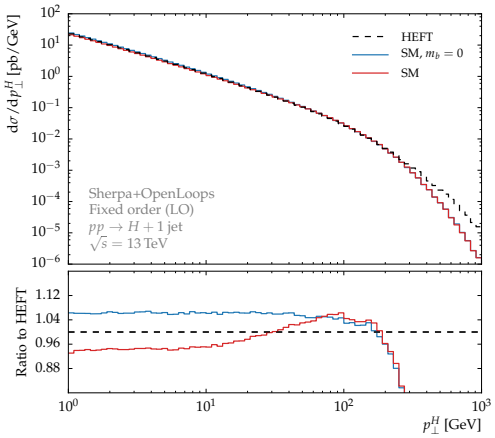

Figure 4.6: Bottom quark mass effects at fixed leading order. The minimum jet p_T is set to 1 GeV in order to map out the low p_T region as well.

QCD emissions do not factorize. Since a factorisation is essential for the applicability of resummation techniques, it was proposed to use a separate resummation scale of the order of m_b for the contributions involving y_b, thereby restricting the range of transverse momenta where resummation is applied to the phase space where factorisation is guaranteed. Two quantitative prescriptions have been proposed for the determination of a specific numerical value for the resummation scale of the bottom contributions in [204, 205]. These two methods yield numerical values of 9 GeV and 31 GeV [200] for the dominant top-bottom interference terms. In addition to m_b, these values will therefore be considered for numerical studies. The pure top quark contributions proportional to y_t^2 will be treated as usual, with the resummation scale set to m_H.

While reference [183] was concerned with analytical resummation techniques, similar approaches were studied in the context of NLO-matched parton shower Monte Carlos [200, 204, 205]. In a parton shower Monte Carlo, the resummation scale is the starting scale of the parton shower μ_Q, which restricts the hardness of QCD radiation a parton shower might produce. The results presented here will be restricted to the leading order as the approximation used for the NLO calculation of the top quark contributions (4.9) is invalid for the bottom quark terms. Using separate parton shower starting scales for the top and the bottom contributions, respectively, requires to generate and shower them separately as well. A corresponding separation of terms in the one-loop matrix elements was implemented in OpenLoops for this purpose. By means of this separation into terms proportional to y_t^2 and the remainder, one can generate an MC@NLO sample for the top quark contributions while calculating the terms involving y_b at leading order.

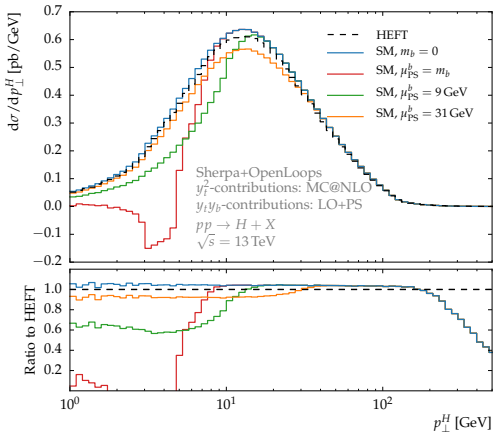

(a) Bottom quark mass effects calculated at parton shower accuracy with small parton shower starting scales μ_{PS}^b. The specific values chosen for μ_{PS}^b are motivated in the text.

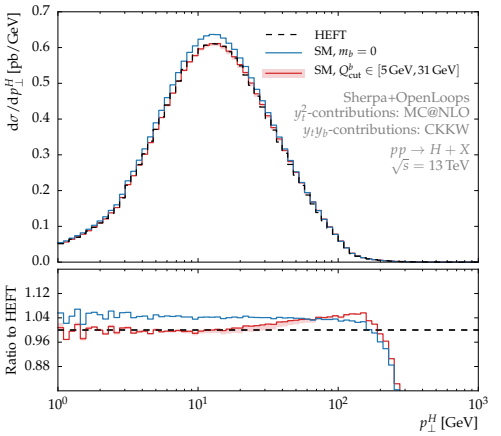

(b) Bottom quark mass effects taken into account by means of CKKW merging with a small merging scale $Q_{cut}^b = \mathcal{O}(m_b)$. The red uncertainty band shows variations of this scale as indicated.

Figure 4.7: The Higgs transverse momentum spectrum in gluon fusion. Individual curves for the HEFT approximation (dashed) and the full SM result taking into account the mass dependence in the top quark loops and neglecting (blue) and accounting for (red) bottom mass effects.

Figure 4.7a shows the p_T spectrum obtained this way. We show results with the parton shower starting scale used for the bottom contributions, μ_{PS}^b, set to m_b, 9 GeV, and 30 GeV as motivated above. The parton shower starting scale for the top quark contributions will be $\mu_{PS}^t = m_H$ throughout. For small μ_{PS}^b, the suppression in the low p_T region below m_b is much more pronounced than in the fixed order result in figure 4.6. When lowering μ_{PS}^b down to sufficiently low values, the differential cross section may even become negative as a consequence of the unitary nature of the parton shower. Setting the value of μ_{PS}^b to a small value, the entire leading order bottom cross section contributions will be distributed in a phase space with Higgs transverse momenta not significantly exceeding μ_{PS}^b. Since this cross section is negative for the dominant interference term, the spectrum must become negative at some point when lowering μ_{PS}^b.

Another approach at taking into account the bottom quark contributions in a parton shower Monte Carlo simulation shall therefore be suggested here. The non-factorisation of the real emission matrix elements above some scale Q_{cut}^b can be taken into account by correcting any parton shower emissions harder than this scale with the appropriate fixed order matrix elements. This can be done consistently using the leading order CKKW merging

techniques described in chapter 2. Setting the merging scale for the bottom contributions Q_{cut}^{b} to m_b implements the correction of parton shower emissions in the regime, where the matrix elements involving m_b do not factorize. In contrast to the method in which the parton shower starting scale ist set to m_b, this does not restrict all emissions to the phase space below this scale. Above Q_{cut}, parton shower emissions are, however, corrected using the appropriate fixed-order accuracy of the real emission matrix elements. Their non-factrisation is therefore properly accounted for.

Furthermore, the parametric accuracy of this method guarantees a leading order accurate Higgs transverse momentum distribution above Q_{cut}^{b}. This is parametrically the same accuracy that NLO-matched parton shower simulations achieve. The bottom quark corrections to inclusive observables are only leading order accurate, however. But as mentioned in section 4.3, the NLO corrections to the bottom contributions in the inclusive cross section are very small.

Figure 4.7b shows the bottom quark effects on the p_T spectrum in this approach. Matrix elements with up to one jet are included in the merging such that a leading order accuracy in α_s is guaranteed for both the top and the bottom contributions to the p_T spectrum. This allows a direct comparison to figure 4.6. The effects of the bottom quarks lead to a very similar suppression pattern over the entire displayed range of p_T. The large NLO K-factor that appears in the MC@NLO calculations of the top contributions affects the overall normalisation of the bottom quark effects in the ratio plot, however. They are correspondingly smaller by roughly 50 % in the ratio plot of figure 4.7b when compared to figure 4.6. The sensitivity to variations of the scale in the calculation that effectively accounts for the presence of the bottom mass in the problem is drastically reduced. Figure 4.7b includes an uncertainty band corresponding to variations of Q_{cut}^{b} in the interval between m_b and 31 GeV. On the displayed scale, these variations are hardly visible.

4.7 Finite Top Mass Effects at a Future Collider

Having considered a Run-II LHC collider setup so far, it is also interesting to assess the magnitude of finite top mass corrections at higher energies in future collider experiments. Among the options that are being currently considered is a hadron-hadron collider operating at a centre-of-mass energy of 100 TeV [206, 207]. In this section, Higgs production through gluon fusion at a 100 TeV proton-proton collider will therefore be considered.

Figure 4.8 shows the Higgs transverse momentum distribution at 100 TeV for Higgs production in association with up to three jets calculated at fixed leading order. From the ratio plots in the lower panels of this figure it is evident that the relative size of the finite top-mass corrections to the p_T distributions exhibit the same universal suppression pattern

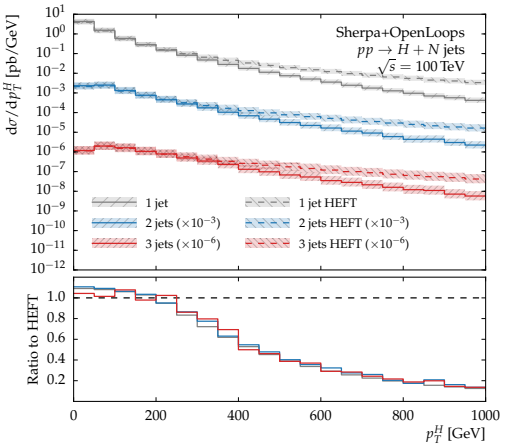

Figure 4.8: Differential Higgs transverse momentum distributions in Higgs production with up to three jets at a future 100 TeV proton-proton collider. The error bands indicate independent variations of the factorisation and renormalisation scales by factors of two up and down.

for all jet multiplicities. When comparing the results for collider energies of 13 TeV and 100 TeV, the similarity of the relative size of the corrections is quite remarkable. Considering the increase in partonic energy that is available at 100 TeV, one could have expected that for a given value of Higgs p_T , the mean partonic centre-of-mass energy would be higher, thus giving rise to larger discrepancies between the HEFT calculation and the m_t-exact calculation. This is, however, not the case, even for three-jet final states, where the jets can in principle carry large amounts of additional energy.

However, a notable effect of the increased centre-of-mass energy can be observed when considering cumulative distributions, as exemplified in figure 4.9. The total cross section receives large finite top mass corrections at $\sqrt{s} = 100\,\text{TeV}$ when applying a minimum transverse momentum cut on the Higgs. This is due to the fact that the tail of the Higgs transverse momentum spectrum exceeds far into the high energy regime, where finite top-mass effects are large. The effect is already substantial for a cut of $p_T > 50\,\text{GeV}$, where the HEFT result overshoots the m_t-exact result by more than 50 % in the three-jet case. The same effect can be observed in the n-jet inclusive cross sections that are displayed in figure 4.9b as a function of the minimum jet transverse momentum. Even for moderate cuts on the jet transverse momenta around 50 GeV, large corrections of the order of −30 % are observed, indicating a poor description of even very inclusive observables in three-jet final states. Table 4.2 illustrates this further with the leading order cross sections for all three jet multiplicities at $p_T^{j,\text{min}} = 50\,\text{GeV}$.

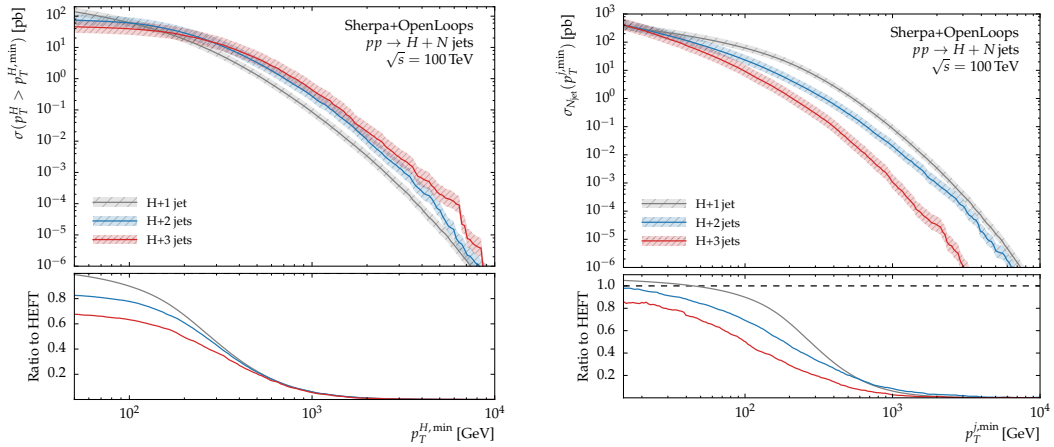

(a) Total cross sections for one-, two-, and three-jet final states as a function of a minimum Higgs transverse momentum cut. A minimum jet transverse momentum cut of 50 GeV is applied.

(b) Total cross sections for one-, two-, and three-jet final states as a function of the minmum jet transverse momentum cut applied in the jet definition.

Figure 4.9: Fixed-order cross sections for Higgs production in association with up to three jets as a function of a minimum Higgs transverse momentum cut (left panel) and as a function of the minimum jet transverse momentum cut (right panel) with finite top-mass effects taken into account at a 100 TeV proton-proton collider. The lower panels show the ratios to the respective HEFT predictions and quantify the finite top-mass corrections. The uncertainty bands indicate independent variations of the factorisation and renormalisation scales by factors of two up and down.

	H	Hj	Hj^2	Hj^3
HEFT	215 pb	138 pb	94 pb	68 pb
SM	229 pb	137 pb	79 pb	47 pb

Table 4.2: Leading order inclusive cross sections for Higgs boson boson production at a 100 TeV-collider in association with $n = 0, 1, 2, 3$ jets based on the m_t-exact calculation (SM) and the HEFT approximation. Jets are reconstructed using the anti-k_T algorithm with $R = 0.4$ and a minumum transverse momentum of 50 GeV. Factorisation and renormalisation scales were set to the Higgs mass in the calculation.

4.8 New Physics Effects in the Higgs-Gluon Coupling

While the Higgs couplings to massive gauge bosons can be extracted from measurements of processes that proceed dominantly though tree-level diagrams, current measurements of the Higgs coupling to top quarks largely rely on loop-mediated couplings between gluons and the Higgs [26].

A more direct measurement can be performed based on top pair associated Higgs production. However, the extremely complex final states that arise from this production mechanism and the smaller production cross sections render such analyses challenging [208–212].

On the other hand, a determination of the top Yukawa coupling based on loop-induced couplings necessarily comes with a certain model dependence. Assuming that this coupling is entirely due to top quark loops, one can constrain y_t from measurements of the Higgs production rate in gluon fusion, but this assumption becomes invalid if additional BSM particles contribute to the loops. In composite Higgs models, the top Yukawa can be shifted downwards, while additional vector-like top partners can contribute in such a way as to largely compensate for this effect [213–217]. In Supersymmetric theories, top and bottom squarks can generate sizeable perturbative corrections to the Higgs-gluon coupling that can also compensate each other in certain parameter regions [218–222]. In both scenarios, the total gluon fusion production rates would be unaffected and additional strategies would have to be devised in order to disentangle Standard Model contributions from possible BSM contributions in the loops.

As demonstrated in section 4.5, the Higgs transverse momentum spectrum is sensitive to the mass of particles that mediate the Higgs-gluon interactions. In the region of large $p_T \gg m_t$, the the infinite top mass approximation predicts a much harder spectrum than the m_t-exact result. Contributions from a hypothetical additional BSM particle of mass $M \gg p_T \gg m_t$ would therefore manifest themselves in an excess of events in the high-p_T regime. Based on this observation, it was proposed in the literature to use event kinematics of jet-associated Higgs production as a probe for new physics in the Higgs-gluon coupling [179, 203, 223–225]. The work presented in this section aims at assessing the LHC's potential for constraining generic BSM scenarios by means of this strategy, with a particular emphasis on improved simulations based on the implementation of finite top mass effects presented in section 4.3. For this purpose, a benchmark model will be considered which is based on the following considerations: as long as $M \gg p_T \gg m_t$ is satisfied, one can capture the impact of additional heavy states of mass M in the loops by means of an effective interaction in the form of (4.2). Focusing on the case where the BSM physics leads to a simultaneous reduction of the top Yukawa coupling by a factor of $\kappa_t < 1$, thus leaving the total gluon fusion production cross section approximately untouched, one can parametrise the relevant interactions by a

Lagrangian of the form

$$\mathcal{L} = \mathcal{L}_{\mathrm{SM}}(y_t = \kappa_t y_t^{\mathrm{SM}}) + \kappa_g \frac{\alpha_s}{12\pi} \frac{H}{v} G_{\mu\nu} G^{\mu\nu} . \tag{4.12}$$

The two reference parameter sets

$$(\kappa_t, \kappa_g)_{\mathrm{SM}} = (1, 0) , \tag{4.13}$$

$$(\kappa_t, \kappa_g)_{\mathrm{BSM}} = (0.7, 0.3) . \tag{4.14}$$

will be considered. While the first point corresponds to the Standard Model, the second BSM parameter set was chosen such that the total gluon fusion cross section remains approximately SM-like by satisfying $\kappa_t + \kappa_g = 1$, in order to avoid tension with existing measurements.

The discriminating observable for the two benchmark scenarios in this analysis is the Higgs transverse momentum spectrum. In the literature, it has been pointed out that in the regime of large Higgs transverse momenta, final states with two or even three jets contribute significantly [194] and that the inclusion of not only one-jet final states has the potential to increase sensitivity [203]. It is therefore desirable to include matrix elements for higher jet multiplicities in a merged calculation also for the signal. With the implementation of heavy quark mass effects presented in section 4.3, such a merged calculation can be performed fully automatically. Focusing on the phase space of large Higgs transverse momenta, bottom contributions will be neglected throughout. Technically, the simultaneous inclusion of finite top mass effects and contributions arising from the effective gluon-Higgs coupling in the Lagrangian (4.12) can be achieved by means of SM loop matrix elements. For this purpose, the top quark Yukawa coupling is modified with a factor κ_t and an additional SM quark contribution is introduced. The mass of this additional quark is set to a very large value and its Yukawa is modified with the a multiplicative factor κ_g. The decay channel for the Higgs considered here is $H \to W^+ + W^- \to \ell^+ \ell^- \nu_\ell \bar{\nu}_\ell$ with $\ell \in \{e, \mu\}$.

The dominant backgrounds to this signature arise from top pair production and non-resonant W pair production (with no intermediate Higgs boson or tops). The latter can be split up further into a component that proceeds through tree-level diagrams at leading order and a gluon-initiated QCD contribution that is mediated by quark loops (see chapter 5 for more details). The top backgrounds as well as the tree-induced WW component are simulated using the NLO multi-jet merging techniques of [89, 90]. In case of the top background, NLO matrix elements for the core process are included along with LO matrix elements for up to three additional hard jets. The tree-induced WW contributions are simulated using NLO matrix elements for up to one jet and LO matrix elements for up to three additional jets in the final state. For the loop-induced contributions, leading order merging techniques can be employed as described in chapter 5. Matrix elements for up to

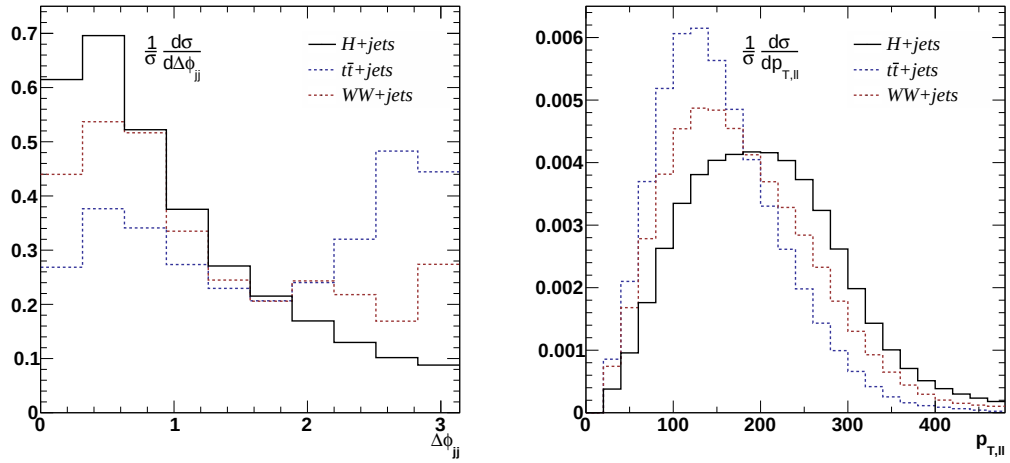

(a) Dijet azimuthal separation in the two-jet inclusive sub samples of signal and background contributions.

(b) Charged dilepton transverse momentum.

Figure 4.10: Example distributions for observables used to suppress backgrounds.

one additional jet are included in this setup.

In order to estimate the LHC's sensitivity for the benchmark BSM scenario, an analysis that largely follows the $H \to W^+W^-$ analysis of reference [203] with fully leptonic W boson decays was performed. Charged leptons ℓ with transverse momentum above 20 GeV are reconstructed in the pseudorapidity range $|\eta_\ell| < 2.5$. Jets are reconstructed using the anti-k_T algorithm with radius parameter $R = 0.5$ and a minimum transverse momentum of 40 GeV. A b-jet veto is applied in order to suppress top backgrounds, assuming a b-tagging efficiency of 70 % throughout the phase space with a mistag rate of 2 %. As an effect of spin correlations, the charged leptons in the signal tend to be emitted into the same direction [226, 227]. This also applies to the neutrino pair and motivates a cut on the charged dilepton azimuthal separation $\Delta\phi_{\ell\ell} < 0.8$, a missing transverse energy requirement of $E_T^{\text{miss}} > 45\,\text{GeV}$, and a cut on the charged dilepton transverse momentum $p_T^{\ell\ell} > 180\,\text{GeV}$. A charged dilepton invariant mass requirement of $10\,\text{GeV} < m_{\ell\ell} < 60\,\text{GeV}$ suppresses Drell-Yan backgrounds. After the application of this cut, Drell-Yan backgrounds are negligible and hence not considered further in what follows. In the two-jet inclusive sub sample, angular correlations between the two leading jets can be exploited in order to suppress top pair backgrounds (see figure 4.10a). An azimuthal separation of $\Delta\phi_{jj} < 1.8$ is applied in order to achieve this.

Table 4.3 shows a cut flow with total cross sections after the successive application of each of the cuts described above. Figure 4.10 shows example distributions for observables used to

	$n_{\text{jet}} \leq 1$			$n_{\text{jet}} \geq 2$		
	H	WW	$t\bar{t}$	H	WW	$t\bar{t}$
$p_T^\ell > 20\,\text{GeV}$, $\lvert y_\ell \rvert < 2.5$	87.9	3220	9640	6.50	203	5890
b-jet veto	84.9	3180	7400	5.09	189	2790
$10\,\text{GeV} < m_{\ell\ell} < 60\,\text{GeV}$	69.0	628	1470	4.22	36.2	503
$E_T^{\text{miss}} > 45\,\text{GeV}$	49.7	504	1250	3.55	32.6	493
$\Delta\phi_{\ell\ell} < 0.8$	24.0	195	561	2.78	20.2	237
$m_T < 125\,\text{GeV}$	23.7	74.5	250	2.75	10.8	119
$p_T^H > 300\,\text{GeV}$	0.27	1.41	1.24	0.42	2.12	5.32
$p_T^{\ell\ell} > 180\,\text{GeV}$	0.15	0.58	0.35	0.24	0.98	1.87
$\Delta\phi_{jj} < 1.8$				0.21	0.69	0.90

Table 4.3: Signal and background cross sections in fb after each step in the applied cut flow. The inclusive samples are split into sub-samples of up to one jet and more than one jet in the final state.

suppress backgrounds.

In order to assess the LHC's Run-II sensitivity for the benchmark BSM scenario, a two-dimensional binned log-likelihood test is performed. The event rates binned in the Higgs transverse momentum and in the number of jets serve as input. This procedure exploits the shapes of the Higgs transverse momentum spectrum in individual jet bins, which have proven to exhibit a universal dependence on the loop structure that mediates the Higgs-gluon coupling. The methods of [228] are used to calculate a signal confidence level CLs as defined in [229, 230]. Figure 4.11 shows the expected signal confidence level as a function of the integrated luminosity based on this analysis and assuming the absence of new physics in the Higgs-gluon coupling. As shown in this plot, an exclusion of the BSM benchmark scenario based on CLs < 5 % would require an integrated luminosity of around $700\,\text{fb}^{-1}$.

4.9 Conclusions

The description of the heavy quark loop-induced couplings between gluons and the Higgs boson in terms of an approximate effective interaction greatly facilitates calculations of the most dominant Higgs production channel at the LHC. This approximation can be understood as a low-energy or infinite top mass limit. For the calculation of the inclusive cross section at LHC energies, the low-energy approximation yields results that agree with a full calculation within the perturbative uncertainties even at N^3LO. Observables that are more sensitive to large partonic energy transfers are, however, poorly described when employing the low-energy effective theory description. In particular, the Higgs transverse momentum

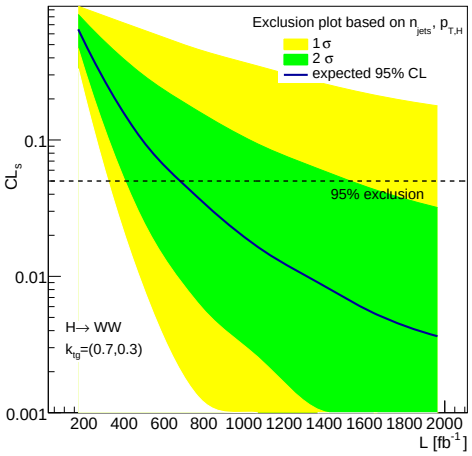

Figure 4.11: Expected signal confidence level CL_s for the BSM benchmark scenario as a function of the integrated luminosity collected at the LHC with $\sqrt{s} = 13\,\text{TeV}$.

distribution is overestimated by orders of magnitude in the tail. Full calculations including the exact top mass dependence beyond the leading order are only available for fully inclusive Higgs production. However, at large transverse momentum, Higgs production in association with jets has a large impact.

An implementation of finite top mass effects in gluon fusion Higgs production that allows to systematically include corrections in an approximate way at NLO for in principle arbitrary jet multiplicities in the final state was presented in this work. Based on this approximation, results for the Higgs boson transverse momentum distributions obtained from NLO matched and merged samples were presented. When comparing the top quark mass dependence in one-, two-, and three-jet final states, a universal suppression can be observed. This pattern agrees very well with the corresponding leading order results and an approximate factorisation of top mass effects from α_s corrections was therefore observed. Finite top mass corrections were also studied for a hypothetical future proton-proton collider operating at a centre-of-mass energy of 100 TeV. In contrast to the situation at the LHC, finite top-mass effects are sizeable at 100 TeV even when considering inclusive jet cross sections with moderate cuts on the jet transverse momentum. It should furthermore be noted, that the event rates for Higgs-boson production in association with TeV-scale jets can exceed several fb at a future 100 TeV hadron collider [4]. In this kinematic regime, the HEFT approximation completely fails and finite top-mass effects must be taken into account in order to obtain meaningful predictions.

A treatment of contributions involving the bottom Yukawa coupling based on m_b- and

m_t-exact leading order matrix elements in combination with tree-level multi-jet merging techniques was proposed. This approximation is appropriate since it allows to retain leading order accuracy for the corresponding contributions in the p_T-spectrum and it also allows to account for the non-factorisation of real emission amplitudes for p_T above m_b. In this approach, the uncertainty associated with the appearance of m_b as an additional scale in the calculation is drastically reduced as opposed to other methods proposed in the literature.

It has been pointed out previously by other authors that the sensitivity of the Higgs transverse momentum spectrum to the loop-structure which mediates the Higgs-gluon coupling can be used to constrain new physics which couples to both the Higgs and gluons. Using the approximate implementation of top mass effects at NLO, the LHC's sensitivity to such BSM scenarios in a jet-differential analysis was estimated. It was found that an integrated luminosity close to $1\,\text{ab}^{-1}$ is needed in order to exclude the BSM benchmark scenario studied. On that time scale it appears unlikely that this detailed kinematic analysis will be able to compete with dedicated Higgs couplings measurements that include top-associated Higgs modes [208–212].

5 Loop-Induced Production Channels in Invisible Higgs Decay Searches

In the Standard Model, "invisible" Higgs decays, i.e. Higgs decays into particles that escape the experiment undetected due to their negligible strong and electromagnetic interactions, arise mostly from Z-mediated couplings of the Higgs to neutrinos. LHC searches for invisibly decaying Higgs bosons are not sensitive to the actual Standard Model invisible Higgs branching fraction of about 0.1 %. These searches rather aim at constraining BSM models that predict an enhancement of this observable. Examples of such model include extensions of the SM in which an additional scalar field is introduced which is not charged under any of the SM gauge groups [231–237]. Being a singlet, such a field can have renormalisable couplings only to the Higgs. It therefore mediates interactions with an otherwise completely "hidden" sector. Such models are hence sometimes referred to as *Higgs portal models* and can provide, with the singlet scalar itself, a viable dark matter candidate, for example

The collider signature of an invisibly decaying Higgs boson is characterised by a momentum imbalance of the measurable final state. At a hadron collider like the LHC, this imbalance can only be measured in the transverse plane, since the centre-of-mass momentum of the colliding partons along the beam direction is unknown. Invisibly decaying Higgs bosons would therefore manifest themselves in an excess of events with missing transverse momentum and can only be identified though the recoiling visible part of the final state. In gluon fusion, where QCD jets can provide the recoil for an invisibly decaying Higgs boson, the irreducible background due to neutrino production through Z bosons in association with jets is extremely large, rendering this channel unuseful for invisible Higgs decay searches [238]. The tagging dijet system in VBF [239] or the decay products of the vector boson in VH production, however, can be used to suppress backgrounds to a sufficiently low level [240, 241]. Both of these production channels are of vital importance for the derivation of upper bounds on the Higgs invisible branching fraction at the LHC. Using Run-I data, ATLAS and CMS were able to exclude invisible Higgs branching fractions larger than 23 % and 58 %, respectively [242, 243]. In view of these results and the SM prediction for this observable, it can be concluded that there is still ample room for new physics in the Higgs sector. Continuing efforts to further constrain the invisible Higgs branching fraction during

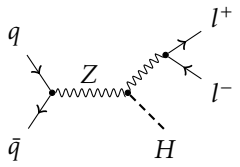

Figure 5.1: Lowest order of Feynman diagram contributing to hadronic ZH production.

Run-II are therefore required in order to close an otherwise unexplored region where new physics could be found.

The subject of the work presented in this chapter is a careful analysis of formally subleading *loop-induced* contributions to both signal and background in searches for invisible Higgs decays in the Z-associated Higgs production channel. These contributions were not included in the invisible Higgs decay analyses of Run-I data performed by ATLAS and CMS [243, 244] and their phenomenological impact therefore needs to be quantified. The discussion will be focused on final states in which the Z boson decays into oppositely charged pairs of either electrons or muons, which will be collectively denoted as $l^{\pm}$. Hadronic Z decay channels are of relevance for LHC analyses as well, but they are typically more difficult to reconstruct and less sensitive [243, 245]. However, since the conclusions drawn from the analysis presented here concern additional *production* mechanisms for the ZH system, the decay mode of the Z will be of little relevance for the discussion.

5.1 Z-Associated Higgs Production in the SM

At leading order, the production of a Higgs boson in association with a Z bosons proceeds through the *Higgs-strahlung* diagram depicted in figure 5.1. Due to the apparent diagrammatic similarity to the Drell-Yan lepton pair production process $q\bar{q} \to l^+l^-$, the NLO QCD corrections to the tree-level differential cross section can be derived from corresponding Drell-Yan calculations [246]. As in case of the Drell-Yan process, the scale uncertainties, being of the order of 5 % at NLO QCD for LHC energies, are very modest. When going to NNLO, the scale uncertainty is further reduced to only 2 % [247]. Parts of the NNLO QCD corrections can be obtained from the corresponding Drell-Yan calculation, but the bulk of correction to the inclusive cross section is due to additional *loop-induced* contributions. They arise from gluon-initiated partonic channels through the loop diagrams shown in figure 5.2. Since there are no lower-order diagrams contributing to these channels, their contribution enters as the square of the diagrams shown in figure 5.2 at relative order α_s^2. It is therefore part of the NNLO correction to the hadronic process $pp \to ZH$, despite being a LO contribution to the partonic process $gg \to ZH$. The loop-induced contributions are also

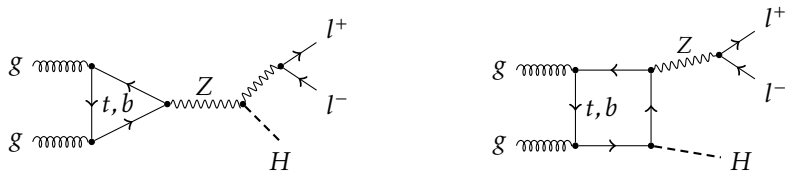

(a) Triangle diagram (b) Box diagram

Figure 5.2: Feynman diagrams contributing to the partonic process $gg \to l^+l^-H$

separately UV finite and gauge-invariant because no tree-level couplings exist that could mediate this partonic scattering and potentially absorb a divergence.

Loop-induced contributions to the total cross section of ZH production were first calculated in references [248–250] and their relative magnitude of around 10 % at the LHC turns out to be larger than what one might naively expect from an NNLO QCD correction [247]. This is a well-understood feature of gluon-induced corrections at high energies. Due to the steep increase of the gluon PDFs with decreasing longitudinal momentum fraction of the gluons involved in the partonic scattering, the relative α_s suppression of the gluon-initiated contributions is partly compensated at high enough hadronic centre-of-mass energies. As will be shown explicitly, their event kinematics is also very different from the tree-induced contributions. This is to be anticipated due to the structure of the Feynman diagrams. For example, despite the apparent similarity to the lowest-order diagram of the tree-induced channel, the triangle diagram in figure 5.2a does not feature a pole in the region where the intermediate Z propagator that is attached to the loop goes on shell. This is due to the Landau-Yang theorem [251, 252], which forbids decays of a massive spin-1 particle into two photons or gluons. Furthermore, the loop-induced contributions are exclusively mediated by heavy quarks and therefore feature threshold effects when the partonic centre-of-mass energy crosses the threshold for on-shell top quark production. For the box diagram in figure 5.2b, this is straightforward to see. In the usual approximation where the first two generations' quarks are treated as massless, they do not contribute to these diagrams since they are proportional to the quarks' Yukawa couplings. Despite not involving any fermion Yukawa, the contributions of massless quarks to the triangle graphs of figure 5.2a vanish as well. This can be seen as follows. The vector-like couplings of the gluon triangle to any vector boson vanishes according to Furry's theorem [253]. The remaining axial couplings to the Z are of equal magnitude but opposite sign for a pair of quarks in a $SU(2)$ doublet. Their sum thus always cancels if the quarks have equal mass. Therefore, only contributions from the top and bottom quarks remain. It is worth noting that the triangle diagram and the box diagram in figure 5.2 interfere destructively, as pointed out by the authors of [250].

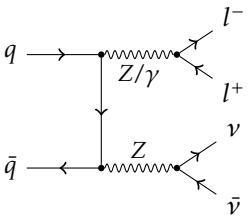

(a) Double resonant ZZ production.

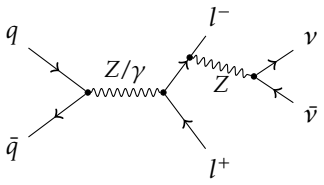

(b) Single resonant diagram.

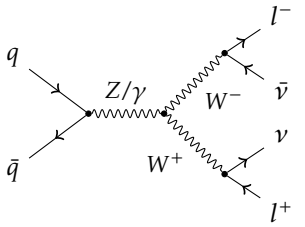

(c) WW contribution with intermediate Z or photon.

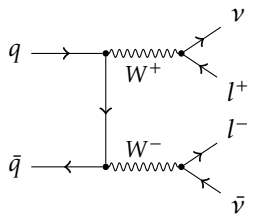

(d) Double resonant WW contribution.

Figure 5.3: Sample of leading order diagrams for the production of a charged lepton pair in association with a pair of neutrinos.

5.2 Backgrounds

Irreducible VV-Backgrounds

The signal signature for invisible Higgs decay searches in association with a leptonically decaying Z boson is experimentally indistinguishable from the signature of charged dilepton production in association with neutrinos. When requiring two charged leptons of the same flavour but opposite electrical charge, this irreducible background is mostly due to double resonant ZZ production as shown in figure 5.3a. Other In addition, there are contributions due to intermediate $W^{\pm}$ bosons and single resonant diagrams. Because the irreducible background is characterised by diagrams with two intermediate vector bosons, it will be referred to as the ZZ/WW-background in the following.

As in the case of the signal, there are loop-induced components to the background as well [254–257]. The relevant diagrams with intermediate Z bosons are shown in figure 5.4. The box diagram in figure 5.4b also includes contribution due to intermediate photons. Single resonant diagrams exist as well but they yield a contribution which vanishes in the limit of massless leptons [254]. In addition to contributions from intermediate Z bosons and photons, loop-induced diagrams with pairs of intermediate W bosons contribute to the background. As in the case of the ZZ process, there are single resonant diagrams, but their contributions cancel with triangle diagrams similar to 5.5a, where the Higgs is replaced with

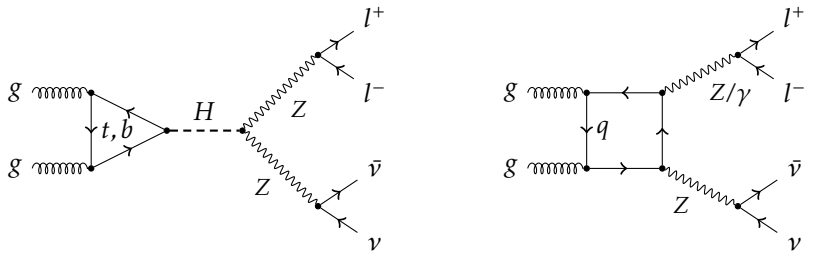

(a) Triangle diagram (b) Box diagram

Figure 5.4: Feynman diagrams contributing to the ZZ component of the process $gg \to l^+l^-\nu\bar{\nu}$

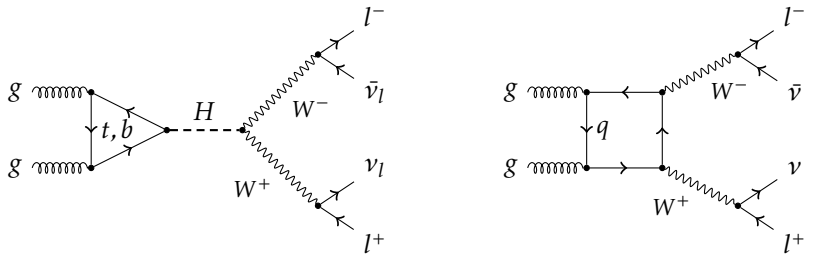

(a) Triangle diagram (b) Box diagram

Figure 5.5: Feynman diagrams contributing to the WW component of the process $gg \to l^-\bar{\nu}_l l^+\nu_l$

a Z boson [256, 257]. The corresponding triangle diagram with an intermediate photon vanishes due to Furry's theorem.

Reducible Backgrounds

In addition to the backgrounds discussed above, which contribute through partonic final states that match the signal signature, there are further background processes to be considered. They can be categorised as follows:

ZW Final states with three charged leptons produced through an intermediate ZW pair can fake a signal if the additional charged lepton originating from the W decay is not vetoed.

Inclusive Z The production of charged lepton pairs with no additional neutrinos can pollute the signal through events with a poorly reconstructed visible final state, resulting in a transverse momentum imbalance. Neutrinos originating from hadron decays can also contribute to missing transverse momentum.

Top Pairs Top pairs that decay leptonically produce final states with two oppositely charged leptons, two neutrinos, and two bottom quarks. If the jets initiated by the bottom quarks are not identified and vetoed, such final states contribute as well.

5.3 Simulation Setup

Simulation of Loop-Induced Contributions

Full higher-order calculations of loop-induced contributions are extremely challenging. The calculation of NLO corrections to these partonic processes is beyond currently available automatised techniques due to two-loop diagrams that enter the virtual corrections. In case of the signal, the calculation is most difficult, since the two-loop virtual corrections include massive double box integrals. Only approximate NLO calculations of this process have been performed in the limit of an infinitely heavy top quark [258].

In the analysis presented here, parts of the radiative QCD corrections will hence be incorporated by means of the leading order multi-jet merging techniques described in chapter 2, rather than by performing full NLO calculations, which are beyond currently available automatised techniques. Using merging techniques, the leading effects of additional QCD radiation on the key differential distributions can be reliably recovered. Multiple soft emissions are accounted for through the parton shower, while the description of hard emissions is improved through the inclusion of the appropriate fixed-order matrix elements. Since the numerical evaluation of one-loop matrix elements is computationally extremely expensive, only matrix elements with up to one extra QCD parton in the final state are used in the merged calculation. The approximate NLO calculation of loop-induced contributions to the signal in [258] and the corresponding results for the background [259–261] indicate large higher order corrections also to inclusive observables of the order of 100 %. This will be accounted for by uniformly scaling up loop-induced contributions by a factor of 2 throughout.

The merging techniques applied here require the relevant matrix elements to be finite after applying a jet-resolution criterion on the final state. For the partonic channel with only gluons in the initial and final state, there are no tree-level diagrams. All squared loop diagrams of this channel are therefore finite and can be included without restrictions. A sample of diagrams contributing to this channel are depicted in figure 5.6. Enhanced by the gluon PDFs at LHC energies, these contributions can be expected to give the dominant contribution. They were therefore included in the calculations presented in [259–265]. When employing a parton shower, contributions from partonic channels with one quark in the initial state are also generated. In a merged calculation, it is thus desirable to include

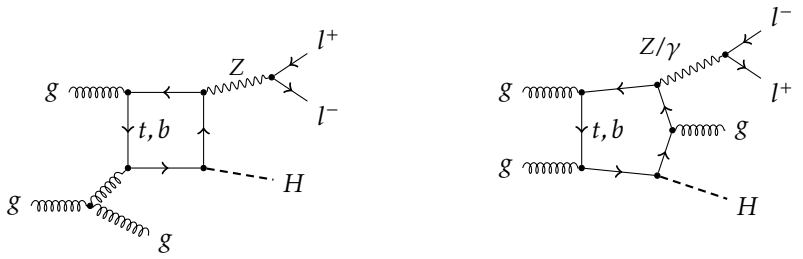

Figure 5.6: Sample of one-loop Feynman diagrams for the partonic channel $gg \to ZHg$

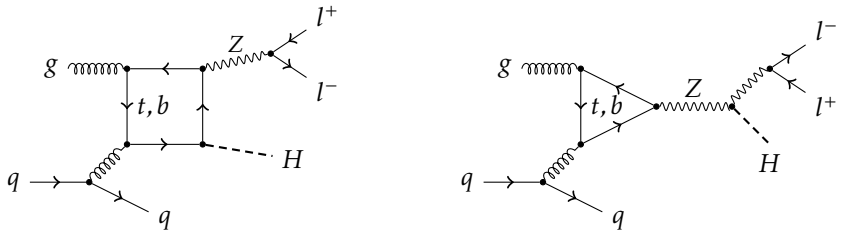

Figure 5.7: Sample of one-loop Feynman diagrams for the partonic channel $gq \to ZHq$

corresponding matrix elements as well. All diagrams with an external quark line and a closed quark loop are therefore included in the calculation presented here. This includes contributions with one and two quarks in the initial state, as shown in figure 5.7 and figure 5.8, respectively. The latter configurations are not generated by the parton shower but they are included here for completeness. The finiteness of all matrix elements used in the merged calculation was checked explicitly through numerical evaluation. It is also worth noting that diagrams with quarks in the initial state can interfere with tree-level diagrams. This interference contributes at lower order in α_s. It is thus included as an NLO-correction to the tree-induced contributions as described below.

Simulation of Tree-Induced Contributions

For the purpose of this study, the tree-induced Hl^+l^- signal contributions, the tree-induced ZZ/WW backgrounds, the ZW backgrounds, the top-pair backgrounds, and the inclusive Z background are calculated using the NLO merging techniques described in chapter 2. NLO matrix elements for up to one extra QCD parton in the final state are included in the calculations of all processes. In case of the inclusive Z process, NLO matrix elements for two additional jets in the final state are included as well. The calculation of the top quark background is simplified by using matrix elements with stable top quarks in the final state and by simulating their decay in the narrow-width-approximation at leading order using

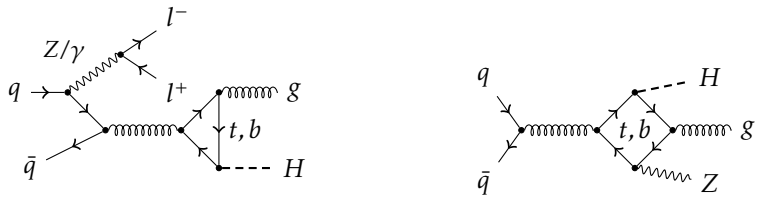

Figure 5.8: Sample of one-loop Feynman diagrams for the partonic channel $gq \to ZHq$

the methods introduced in section 3.6. Hadronisation and underlying event simulations are included throughout.

Note that real-emission corrections to the VV background with two additional QCD partons in the final state are included in the merged calculation. They would normally include contributions from $l^+l^-\nu\nu b\bar{b}$ final states. Since these final states are dominated by diagrams with intermediate top quarks, they are removed from the VV sample and instead accounted for through the simulation of the resonant the top pair production.

Note also that the virtual corrections to the matrix elements with one extra QCD parton in the final state include the interference term between tree-level diagrams and the one-loop diagrams whose squared contribution is accounted for through the loop-induced part as described above.

5.4 Characteristics of Loop-Induced Contributions

In order to assess the impact of loop-induced contributions in invisible Higgs decay searches, an analysis similar to the Run-I studies of ATLAS [244] and CMS [243] in the Z-associated production channel was performed for Run-II energies of $\sqrt{s} = 13\,\text{TeV}$. The analysis is focused on leptonic Z boson decays. The leptonic Z boson decay products are required to have a transverse momentum larger than 20 GeV with pseudorapidity $|\eta_l| < 2.5$. In this kinematic region, a good experimental electron and muon reconstruction efficiency is guaranteed. Events with exactly two such oppositely charged leptons of the same flavour are selected, thus suppressing the ZW background with an third hard lepton in the final state. In order to suppress non-resonant backgrounds with no intermediate Z, the invariant mass of the dilepton pair m_{ll} is required to be close to the Z boson mass m_Z with

$$|m_{ll} - m_Z| < 15\,\text{GeV}\,. \tag{5.1}$$

The cuts described above will be referred to as the "basic" cuts in the following.

Jets are reconstructed using the anti-k_T algorithm in the pseudorapidity range $|\eta| < 5$ with radius parameter $R = 0.4$. They are required to have a transverse momentum of at least

30 GeV and can be used to suppress $t\bar{t}$ and Z plus jets backgrounds by means of jet vetoes. At least for the tree-induced contributions, a jet veto should affect the signal rate only mildly because jets are dominantly produced through initial state radiation off quarks in this case. The $t\bar{t}$ background with its two b-jets in the final state can, however, be effectively suppressed. In the ATLAS analysis of [244], only events without any jets were retained. The CMS analysis of [243], however, allowed for one jet in the final state and separated events into exclusive one- and zero-jet sub samples.

The missing transverse energy is reconstructed from the sum of three-momenta $\boldsymbol{p}^i$ of all "visible" particles in the final state, including photons, leptons, and hadrons:

$$E_T^{\text{miss}} = |\boldsymbol{p}_T^{\text{miss}}| = |\sum_i \boldsymbol{p}_T^i| \tag{5.2}$$

A lower cut on the missing transverse energy of roughly $E_T^{\text{miss}} > 100\,\text{GeV}$ is typically applied in order to suppress the Z plus jets and similar backgrounds that do not feature genuine missing transverse energy in the partonic scattering process. The invisible Higgs branching fraction will be treated as an unknown throughout the discussion. For the presentation of differential distributions and cross sections, an invisible branching fraction of 100 % will be assumed. This value is already excluded by current measurements but it will only affect the overall normalisation of differential distributions and cross sections, which is of little relevance for the discussion.

Large parts of the discussion will be centred around the relative impact of loop-induced contributions in searches for invisible Higgs decays. These contributions will be labelled "Loop^2" throughout in order to distinguish them from the respective contributions that are induced by tree-level diagrams, which carry the label "Tree" in what follows. Using this notation, the relative impact of loop-induced contributions to signal and background can be quantified in terms of the ratio of cross sections

$$R(E_0) = \frac{\sigma_{\text{Loop}^2}(E_T^{\text{miss}} > E_0)}{\sigma_{\text{Tree}}(E_T^{\text{miss}} > E_0)} \tag{5.3}$$

as a function of a minimum missing transverse momentum cut E_0. The basic cuts described above are understood to be always applied. Since the event samples in the analyses of references [243, 244] are divided according to exclusive jet multiplicities, it is helpful to analyse this observable in exclusive jet bins. Figure 5.9 shows the functional dependence of $R(E_0)$ in exclusive jet bins. While the relative contribution of loop-induced processes to the background remains moderate throughout, a 50 % correction to the signal due to loop-induced processes can be observed for missing transverse energy cuts between 100 GeV and 150 GeV. In this region, both signal curves in figure 5.9 feature a distinctive peak. This peak

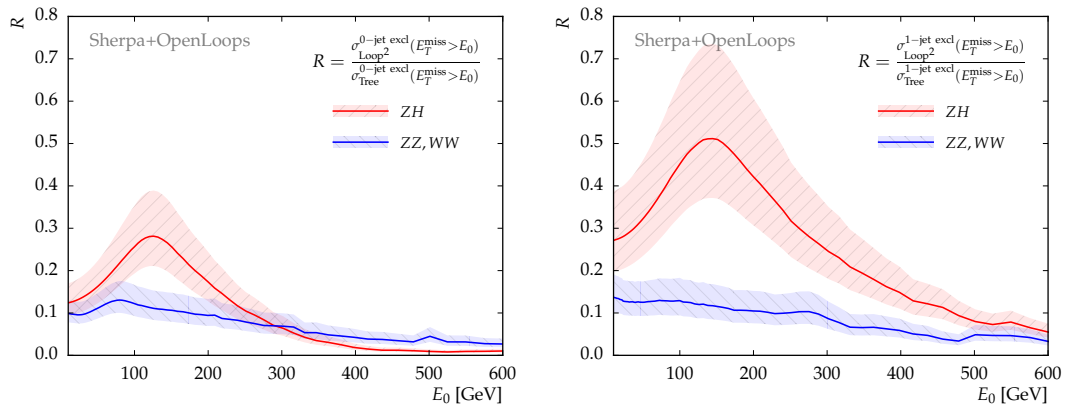

Figure 5.9: Ratio of loop- and tree-induced cross sections as a function of the minimum transverse energy cut in exclusive jet bins. Individual curves for the signal (ZH) and background (ZZ, WW) contributions are shown. The uncertainty bands are generated via independent variations of the factorisation and renormalisation scale in the calculation of the loop-induced contributions by factors of two up and down.

also appears in the differential missing transverse energy distribution, which is shown in figure 5.11. It is a manifestation of the top pair threshold at partonic centre-of-mass energies around $\hat{s} = 4m_t^2$ [250]. Assuming that the final state is produced with no longitudinal motion, the top pair threshold is approached when the transverse momentum of the Higgs boson reaches approximately 110 GeV. The loop-induced partonic background processes, being mediated dominantly by light quark flavors, do not feature such pronounced threshold effects.

Another distinctive feature of the loop-induced signal contributions is their large relative size in the one-jet bin when compared to the zero-jet bin, as shown in figure 5.9. In contrast to the background contributions, the signal contributions are much larger in the one jet bin, relative to the respective tree-induced contributions. This indicates differences in the QCD radiation pattern of the two processes, with the signal process radiating stronger. The propensity of a certain process to radiate can be quantified in terms of the jet veto efficiency

$$\epsilon(p_T^j) = \frac{\sigma^{0-\text{jet}}_{\text{excl}}(p_T^j)}{\sigma}. \tag{5.4}$$

It represents the fraction of events one retains after applying a jet veto and therefore depends on the minimum transverse momentum p_T^j of the jet definition. Figure 5.10 shows the dependence of the jet veto efficiency on the jet transverse momentum p_T^j for both the loop-induced background process and the loop-induced signal process. The overall picture in

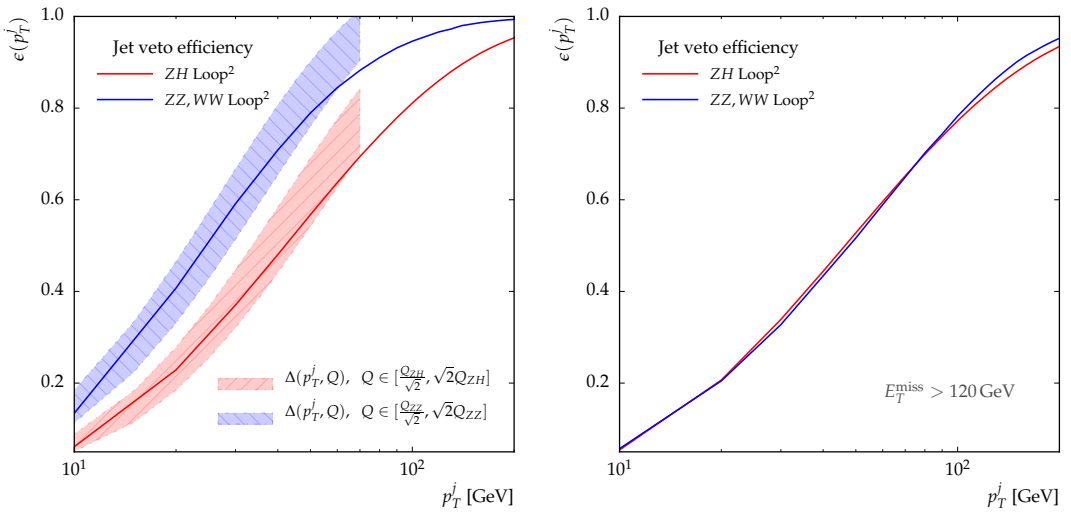

Figure 5.10: Jet veto efficiencies for the loop-induced components of signal (labelled ZH)and background processes (labelled ZZ, WW). The left panel shows the Sudakov approximations as described in the text. The right panel shows the efficiencies after imposing a cut on the missing transverse momentum E_T^{miss}.

which the signal process typically produces more QCD radiation is confirmed by an overall lower jet veto efficiency throughout the displayed range of p_T^j.

These observations can be understood quantitatively. In the leading logarithmic approximation, where a probabilistic parton shower treatment as outlined in chapter 2 can be applied, the jet veto efficiency is given by a no-emission probability, and hence in terms of the Sudakov form factor. For a process with two gluons in the initial state, we have [58]

$$\epsilon(p_T) = \left[\Delta_g(p_T^2, Q^2)\right]^2 = \exp\left[-2C_A \int_{p_T^2}^{Q^2} \frac{\mathrm{d}t'}{t'} \frac{\alpha_s(t')}{2\pi}\left(\ln\left(\frac{\hat{s}}{t'}\right) - \frac{11}{6} + \frac{5}{9}\right)\right], \tag{5.5}$$

where the scale Q denotes the energy scale that characterises the process. In case of the background, this scale is near the mass of the intermediate vector bosons, i.e. around $2m_Z$. In case of the signal, however, the average partonic centre-of-mass energy can exceed the sum of the intermediate bosons's masses considerably because the Higgs boson is typically produced with large transverse momentum above 100 GeV due to the aforementioned threshold effect. Inspired by these considerations, one can derive two characteristic scales

$$Q_{ZZ} = m_Z + m_Z + \kappa \left\langle p_T^Z \right\rangle^{ZZ,WW} \tag{5.6}$$

$$Q_{ZH} = m_Z + m_H + \kappa \left\langle p_T^Z \right\rangle^{ZH}, \tag{5.7}$$

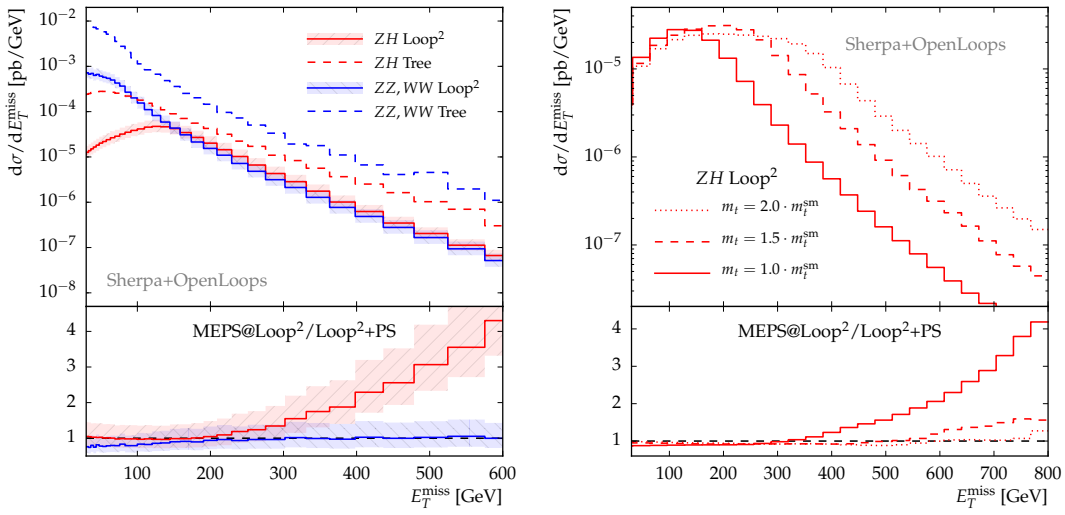

Figure 5.11: Missing transverse energy distributions for the signal and the ZZ and WW background processes. Separate histograms for loop-induced and tree-induced components are shown in the left panel. The merged calculation of loop-induced contribution displayed in the upper panels (MEPS@Loop^2) is compared to a calculation based on the parton shower only (Loop^2+PS) in the lower panels, which show the ratio of the two predictions. The uncertainty bands are generated via independent variations of the factorisation and renormalisation scale by factors of two up and down.The right panel shows results for the loop-induced signal process for hypothetical scenarios with a heavier top quark.

where $\left\langle p_T^Z \right\rangle^{ZZ,WW}$ and $\left\langle p_T^Z \right\rangle^{ZH}$ denote the mean transverse momentum of the dilepton pair in the respective samples and κ is a factor of order one. Figure 5.10 shows the resulting approximation of jet veto efficiencies by the Sudakov form factor in equation (5.5) obtained with the scale choices (5.7) and (5.6) for $\kappa \approx 1.5$. Because there is a considerable arbitrariness in choosing an appropriate scale, figure 5.10 shows bands for the Sudakov approximation that are generated by varying the scales in (5.7) and (5.6) by factors of $\sqrt{2}$ up and down. The resulting bands can qualitatively reproduce the jet veto efficiencies observed in the Monte Carlo samples in the region of moderate p_T^j, where the leading logarithmic approximation is applicable. Figure 5.10 also shows the jet veto efficiencies after applying a missing transverse energy cut of $E_T^{\mathrm{miss}} > 120\,\mathrm{GeV}$. In this kinematic regime, the signal and background jet veto efficiencies are now almost identical, since the additional cut leads to similar mean partonic centre-of-mass energies in both processes. This is in further support of the arguments put forward above.

Having established that in particular the loop-induced contributions to the signal in invisible Higgs decay searches can be sizeable, their final impact after the application of

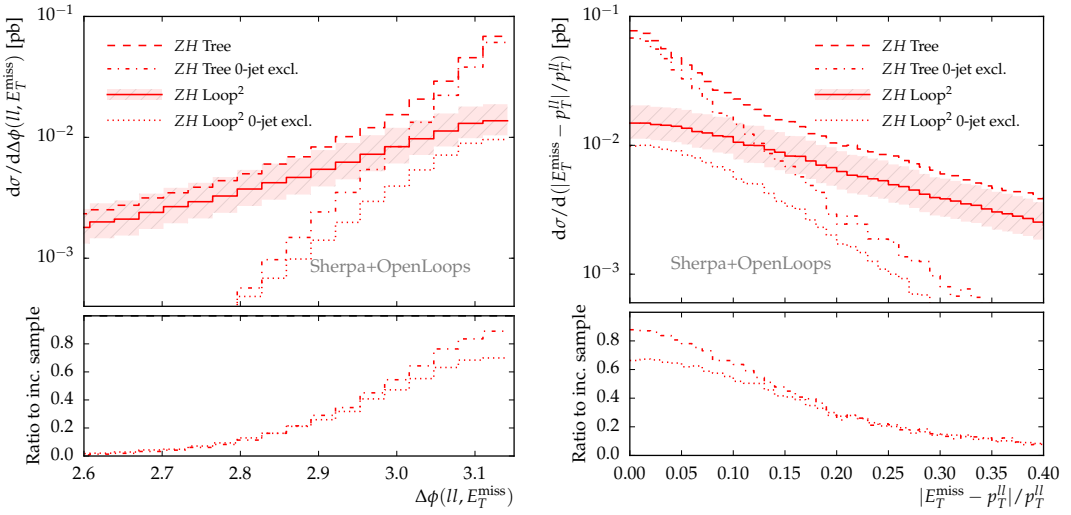

Figure 5.12: Azimuthal correlation (left panel) and correlation of the magnitude (right panel) of dilepton momentum and the missing transverse energy vector in the tree-induced and loop-induced signal contributions. Individual distributions for the inclusive samples as well as the zero-jet exclusive sub samples are displayed in the upper panels. The lower panels show the ratio of the latter to the former. The uncertainty bands are generated via independent variations of the factorisation and renormalisation scale by factors of two up and down.

further background suppression cuts needs to be determined. Further key observables for the purpose of background suppression are based on correlations between the missing transverse energy vector and the dilepton momentum. In the signal contributions, the dilepton transverse three-momentum $\boldsymbol{p}_T^{ll} = \boldsymbol{p}_T^{l^+} + \boldsymbol{p}_T^{l^-}$ and the missing transverse momentum vector $\boldsymbol{p}_T^{\text{miss}}$ are strongly correlated. At leading order, they are always back-to-back and of equal magnitude, which implies

$$\delta_T = \frac{|p_T^{ll} - E_T^{\text{miss}}|}{p_T^{\text{ll}}} = 0 \tag{5.8}$$

$$\Delta\phi(p^{ll}, p^{\text{miss}}) = \pi, \tag{5.9}$$

where $p_T^{ll} = |\boldsymbol{p}_T^{ll}|$. This correlation is necessarily much weaker in all reducible backgrounds, since the transverse recoil of the dilepton pair in any of those contributions is not exclusively provided by missing transverse momentum, even at leading order. These backgrounds can therefore be efficiently suppressed by vetoing events with a δ_T above some cut and events with an azimuthal separation $\Delta\phi(p^{ll}, p^{\text{miss}})$ below some cut.

Figure 5.12 shows the relevant distributions for tree- and loop-induced signal contributions.

	Tree-induced			Loop-induced		
	σ_{incl} [fb]	$\sigma_{\text{excl}}^{0\text{–jet}}$ [fb]	$\sigma_{\text{incl}}^{1\text{–jet}}$ [fb]	σ^{incl} [fb]	$\sigma_{\text{excl}}^{0\text{–jet}}$ [fb]	$\sigma_{\text{incl}}^{1\text{–jet}}$ [fb]
Basic selection	34.5	21.1	13.4	4.9	1.74	3.2
$E_T^{\text{miss}} > 120\,\text{GeV}$	9.7	4.98	4.74	2.9	0.95	1.96
$\Delta\phi(ll, E_T^{\text{miss}}) > 2.5$	8.0	4.97	3.04	2.4	0.95	1.42
$\lvert p_T(ll) - E_T^{\text{miss}}\rvert / p_T(ll) < 0.25$	6.5	4.81	1.65	1.57	0.88	0.70

Table 5.1: Cut flow for typical selection cuts in invisible Higgs decay searches. Tree- and loop-induced contributions to the signal processes are listed separately. The quoted cross section are for LHC proton-proton collisions at $\sqrt{s} = 13\,\text{TeV}$.

For the tree-induced components, the distributions shown in figure 5.12 peak strongly at large azimuthal separations $\Delta\phi(ll, E_T^{\text{miss}})$ and at small values of $|E_T^{\text{miss}} - p_T^{ll}|/p_T^{ll}$. In the case of the loop-induced contributions, the enhancement is much less pronounced in these regions. Background suppression cuts on $\Delta\phi(ll, E_T^{\text{miss}})$ and $|E_T^{\text{miss}} - p_T^{ll}|/p_T^{ll}$ therefore suppress loop-induced contributions slightly more than the tree-induced contributions to the signal. The less pronounced peak structure in the corresponding distribution can be attributed to larger amounts of QCD radiation in the loop-induced signal contributions. Additional QCD radiation decorrelates the momenta of the ZH pair by providing more final state objects that the Higgs boson can recoil against. As can be seen in the lower panels of figure 5.12, the relative contributions of one-jet events is in fact larger for loop-induced contributions than for tree-induced contributions even near $|E_T^{\text{miss}} - p_T^{ll}|/p_T^{ll} = 0$ and $\Delta\phi(ll, E_T^{\text{miss}}) = \pi$.

Table 5.1 shows the cross sections after typical selection cuts as they were applied in Run-I LHC analyses [243, 244] in the form of a cut flow for LHC collision energies of 13 TeV. Despite the fact that the cuts on $|E_T^{\text{miss}} - p_T^{ll}|/p_T^{ll} = 0$ and $\Delta\phi(ll, E_T^{\text{miss}}) = \pi$ slightly disfavour the loop-induced signal processes, their contribution remains sizeable even in the zero-jet exclusive sub sample. In fact, at the end of the cut flow, the relative size of the loop-induced contributions is at the level of 25 %, 20 %, and 40 % in the inclusive sample, the zero-jet exclusive sample, and the one-jet inclusive sample, respectively.

The large loop-induced contributions in the inclusive one-jet sub samples motivate further studies on the impact of multi-jet merging. In jet observables, merging effects can naturally be expected to be large. Without merging, any extra parton level QCD radiation is generated only by the parton shower and hard jets are, correspondingly, not appropriately described. The transverse momentum distribution for the hardest jet in loop-induced signal and background contributions is shown in figure 5.14. Large discrepancies can be observed when comparing the spectra obtained from a merged simulation with the ones obtained from a simulation based on the parton shower only. In the region of large transverse momenta, the

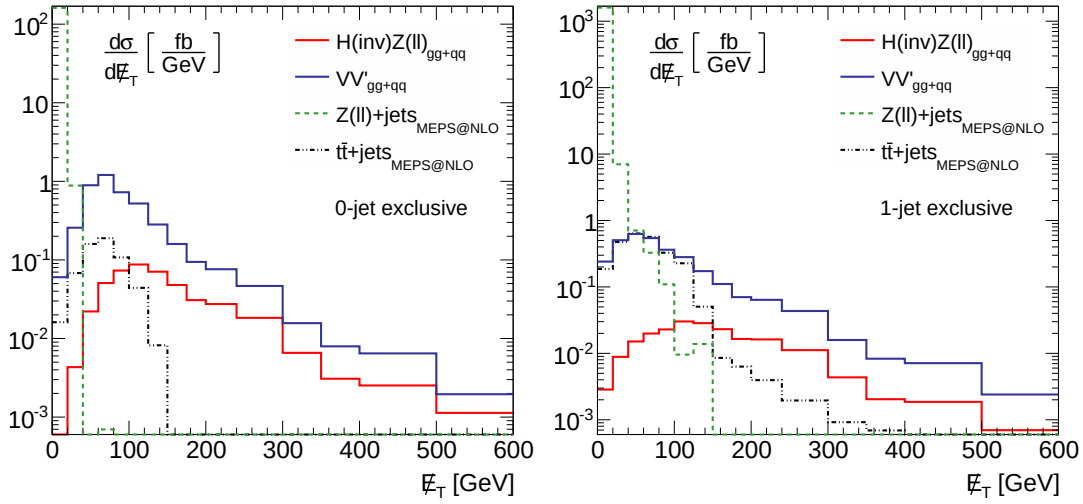

Figure 5.13: Missing transverse energy ($\not{E}_T$) distribution for the total signal contributions (labelled $H(\text{inv})Z(ll)$ in this figure, including loop- and tree-induced components) and the major background processes. The distribution labelled VV'_{gg+qq} includes loop- and tree-induced contributions to the ZZ/WW processes as well as the ZW process. The zero-jet exclusive sub sample is shown on the left while the one-jet exclusive sub sample is shown on the right.

latter underestimates the spectrum by orders of magnitude. For example, a relative factor of approximately 10 can be observed for $p_T^{j_{\text{lead}}} \approx 300\,\text{GeV}$ which is even further enhanced at higher energies. In this regime, the soft and collinear approximation inherent to the parton shower fails. By merging matrix elements with one additional jet into the sample, one can recover the corresponding fixed-order matrix element accuracy that is required for an appropriate description in this regime. The signal and background merging corrections exhibit similar patterns below $p_T^{j_{\text{lead}}} \approx 2m_t$. Above this threshold, however, larger corrections are observed in case of the signal. Furthermore, the background spectrum obtained from the merged simulation features a suppression below $p_T^{j_{\text{lead}}} \approx 100\,\text{GeV}$ when compared to the simulation based on the parton shower only. This indicates an overestimation of one-jet matrix elements by the parton shower splitting kernels in this regime. The right panel of figure 5.14 shows a comparison of the leading jet transverse momentum spectrum obtained from a parton shower simulation, from a merged calculation, and from a fixed order calculation. The fixed order calculation reproduces both the enhancement of the merged result in the tail as well as the corresponding suppression below $E_T^{\text{miss}} \approx 100\,\text{GeV}$, confirming that both features are indeed genuine effects of the 1-jet matrix elements which are included in the merged calculation.

Of even higher relevance in the context of invisible Higgs decay searches are the missing transverse energy distributions. They are shown in figure 5.11, where a merged calculation of loop-induced contributions is compared to a calculation based on the parton shower in the lower panel. For the signal process, the inclusion of additional matrix elements implements very large corrections above $E_T^{\text{miss}} \approx 200\,\text{GeV}$ of the order of several hundred per cent. The simulation based on only the parton shower drastically underestimates the spectrum in this region. The background distributions show no sign of a discrepancy in the tail. Instead, a slight suppression in the region of small values of E_T^{miss} can be observed when comparing the merged calculation to the simpler parton shower simulation. The origin of the striking differences between loop-induced signal and background components can be attributed to the different loop structure, with the signal process being mediated mostly through loops of heavy top quarks. At large values of E_T^{miss}, configurations in which the Higgs boson recoils against a hard jet rather than the dilepton pair apparently have a large impact. These configurations are properly accounted for only in the merged calculation, where they are described with the appropriate fixed-order matrix elements. The hard jet probes the details of the loop structure which is characterised by the top quark mass and the corresponding effects thus become extremely large for missing transverse energy values above the top mass. The right panel of figure 5.11 shows the missing transverse energy distribution for the loop-induced signal process for two hypothetical scenarios in which the top quark mass is scaled up by factors of 1.5 and 2.0. In order to keep the normalisation of the distributions similar, the top Yukawa coupling is kept fixed. From the lower panel of figure 5.11 it is evident that for these hypothetical scenarios the large enhancement of the spectrum in the tail of the distribution is shifted towards even higher values of E_T^{miss}, thus confirming that the loop structure is in fact the origin of the enhancement.

5.5 Constraints on Invisible Decays in Run-II

In this section, the sensitivity of the Z-associated Higgs production channel with leptonic Z decays for a measurement of the invisible Higgs branching ratio during Run-II of the LHC with $\sqrt{s} = 13\,\text{TeV}$ is analysed. For this purpose, signal and background Monte Carlo events were generated as outlined in section 5.3. The analysis is inspired by the Run-I searches of [243, 244] but slightly adapted in light of the findings discussed in section 5.4. In the analysis presented here, exactly two isolated same-flavour, opposite-sign leptons with transverse momentum above 20 GeV in the pseudorapidity range $|\eta| < 2.5$ are required. The lepton isolation criterion applied requires that the hadronic energy deposited withing a cone of radius $R = 0.2$ around the lepton momentum be smaller than 20 % of the lepton energy. The invariant mass of the di-lepton system m_{ll} is required to fall into a Z-boson mass window

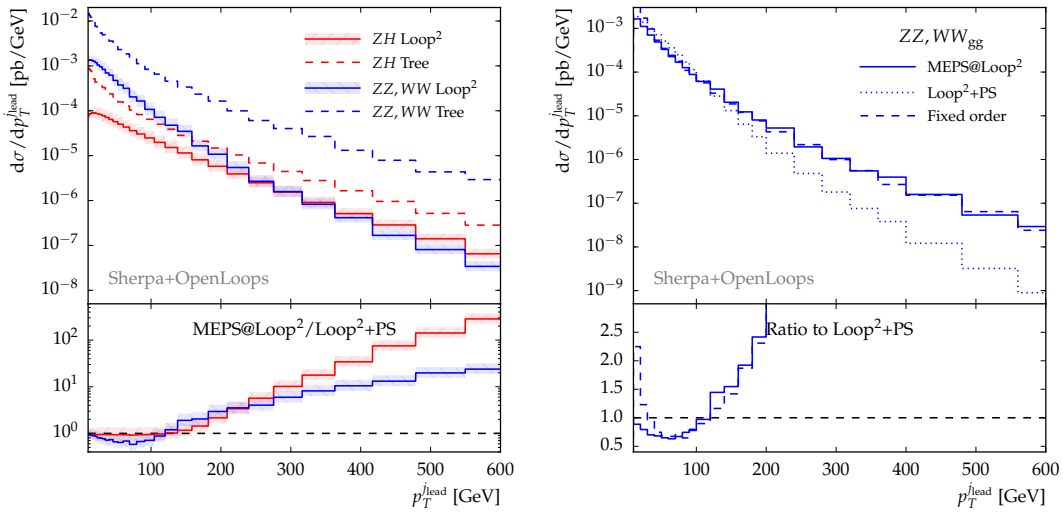

Figure 5.14: Leading jet transverse momentum distribution for loop-induced contributions to signal and background. For illustration purposes, tree-induced contributions are shown in the upper panel of the left figure as well. The merged calculation (MEPS@Loop^2) of loop-induced contributions is compared to simulation based on the parton shower only (Loop^2+PS) in the lower panel. The uncertainty bands are generated via independent variations of the factorisation and renormalisation scale by factors of two up and down. The right panel shows the leading jet transverse momentum as obtained from a merged calculation, a parton shower simulation, and a fixed-order calculation of the loop-induced contributions to the process $pp \to l^+l^-\nu\bar{\nu}+\text{jet}$.

with $|m_{ll} - m_Z| < 15\,\text{GeV}$. Jets are reconstructed using the anti-k_T jet algorithm with radius parameter $R = 0.4$. Only jets with transverse momentum above $p_T^j > 30\,\text{GeV}$ and $|\eta_j| < 5$ are retained in the analysis. To suppress the large $t\bar{t}$ background, b-tagged jets are vetoed, assuming a 70 % b-tagging efficiency and mistagging rate of 1 % [266]. In order to account for a finite experimental energy resolution, a smearing of the missing energy vector with a Gaussian shape of width $\Delta E_T^{\text{miss}} = 20\,\text{GeV}$ is applied.

Since most of the signal sensitivity lies in the boosted regime with $E_T^{\text{miss}} > 100\,\text{GeV}$, where the Z boson decays are emitted at small opening angles, a small azimuthal separation of the leptons $\Delta\phi(l,l) < 1.7$ is required in the analysis. This cut suppresses in particular the $t\bar{t}$ background further. In contrast to cuts on $\Delta\phi(ll, E_T^{\text{miss}})$ and $|E_T^{\text{miss}} - p_T^{ll}|/p_T^{ll}$, however, it does not suppress loop-induced contributions to the signal more than tree-induced contributions.

The full event samples are divided into zero- and one-jet exclusive sub samples, following the analysis of [243]. Given that the signal rate in the one-jet bin is significantly enhanced by loop-induced signal contributions, the events in the one-jet are not discarded as in the analysis of reference [244]. Figure 5.13 shows the missing transverse energy distribution for the signal and background components after the event selection outlined above. The combination of jet a two-jet veto and the missing transverse energy cut reduces both the Z+jets and $t\bar{t}$ backgrounds to manageable levels. The ZZ, WW backgrounds, however, remain sizeable.

In order to estimate the constraining power of this analysis for the invisible Higgs branching ratio $\mathcal{BR}(H \to \text{inv})$, a two-dimensional binned log-likelihood test was performed. The event rates in binned in the missing transverse energy and the number of jets serves as input. This procedure exploits the shapes of distributions in both panels of figure 5.13. The methods of [228] are used to calculate a confidence level CL based on the CL_s technique [229, 230].

Figure 5.15 shows the 95 % CL upper limit on the invisible Higgs boson branching ratio to be expected from LHC Run-II as a function of the integrated luminosity. By means of the analysis presented here, it is possible to constrain the invisible branching ratio to values below 0.3 with an integrated luminosity of only $10\,\text{fb}^{-1}$. This is to be compared to Run-I limits of 0.75 and 0.58 set by ATLAS and CMS, respectively, in the Z-associated Higgs production channel. Figure 5.15 also shows the quantitative impact of loop-induced contributions. When neglecting loop-induced contributions to the background, the limits are stronger and the sensitivity is thus overestimated. For small integrated luminosities, the limit on the invisible branching ratio is underestimated by slightly more than one standard deviation. If one neglects the loop-induced signal component, the bounds one would obtain would be of course weaker. At $10\,\text{fb}^{-1}$, this would result in shifting the correct bound on the invisible branching fraction from about 0.3 to approximately 0.4.

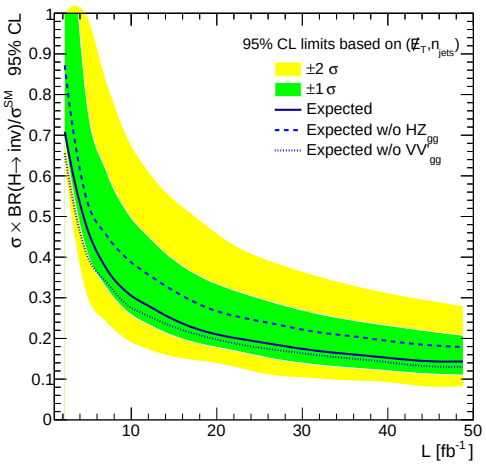

Figure 5.15: Expected 95 % CL upper limit on the product of the l^+l^-H production cross section and the invisible Higgs branching ratio $\mathcal{BR}(H \to \text{inv})$ normalised to the SM production cross section. For comparison, the expected upper limits one obtains when not accounting for the loop-induced background (dotted line) and when not accounting for the loop-induced signal (dashed line) are shown as well.

5.6 Constraints on Simplified Dark Matter Models

As briefly mentioned in chapter 1, there is convincing evidence for the presence of a significant amount of Dark Matter in the universe. While the concrete nature of this hypothesised form of matter remains unclear, weakly interacting massive particles (WIMPs) are one of the most widely studied candidates for Dark Matter. Within the standard model of cosmology and its thermodynamic description of the universe, the WIMP hypothesis assumes that WIMPs were produced at an early stage and in thermal equilibrium with Standard Model matter. With the following cool-down of the universe, the WIMP density would drop as it contributes to its overall energy content. However, assuming that WIMPs can only annihilate pairwise into SM particles, this mechanism becomes suppressed with decreasing WIMP density due to the decreasing probability of two WIMPs "finding" each other. This mechanism is commonly referred to as *freeze-out*. If the thermally averaged product of Dark Matter velocity and Dark Matter annihilation cross section into SM particles approximately assumes a certain value of about $\langle \sigma v \rangle \approx 3 \times 10^{-26}\,\text{cm}^3/\text{s}$, this mechanism can potentially explain the sizeable *relic abundance* of Dark Matter observed today. For weakly interacting particles with a weak scale mass, the thermally averaged annihilation cross section naturally falls into the this region, hence the name "WIMP".

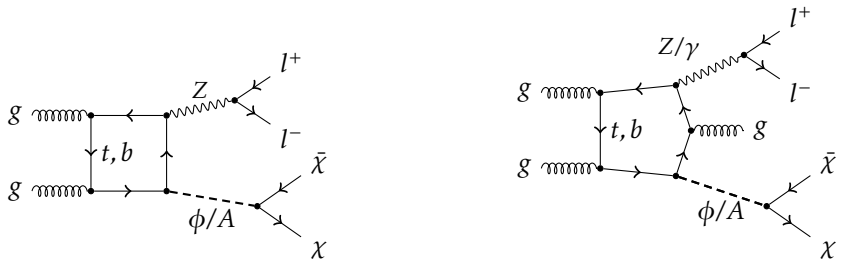

Figure 5.16: Example Feynman diagrams contributing to the signal processes $pp \to l^+l^-\chi\bar{\chi}$ (left) and $pp \to l^+l^-\chi\bar{\chi}\ j$ (right).

Since the concept of a WIMP is fairly generic, a variety of BSM models that predict viable WIMP Dark Matter candidates exists. Their detection is the aim of both direct detection experiments and collider searches. Direct detection experiments [267, 268] rely on scattering reactions between Dark Matter particles and heavy nuclei. These reactions typically involve small energy transfers in the keV range. In hadron collider searches [269–275], the production of Dark Matter particles would manifest itself in the form of missing transverse Energy.

With no indisputable evidence for the detection of Dark Matter in any of those experiments, it is advantageous to interpret experimental results model-independently in an effective field theory (EFT) framework. In this approach, the interactions of Dark Matter particles are introduced through a set of non-renormalisable effective operators whose coefficients can be constrained by experimental analyses. This description is equivalent to integrating out the degrees of freedom which would mediate the effective interactions in a particular model. It is therefore applicable only if typical energy transfers in the experiment do not exceed the masses of particles that are integrated out. This requirement is typically satisfied in direct detection experiments, where the measured energy transfers are of the order of a few keV. In LHC experiments, the energy scales involved are much larger and the applicability of EFT analyses is thus limited [276–283]. Instead of resorting to UV-complete theories and thereby losing the model independence of any derived constraint entirely, a set of simplified models can be invoked [284–290]. By introducing particles that mediate the interactions between the visible SM sector and the Dark Matter particles in a generic way, these models restore a proper description of the high energy collider regime while still representing a wide range of specific BSM models.

In the work presented in this section, expected limits on the parameter space of a simplified model for particle Dark Matter are derived using the analysis described in section 5.5. The model under consideration contains a fermionic Dirac Dark Matter particle χ as well as a mediator of either scalar or pseudoscalar nature that couples both χ and Standard Model

fermions [291–303]. The concept of Minimal Flavour Violation is invoked in order to avoid existing experimental constraints on flavour symmetry violating effects [304]. This is achieved by imposing the Standard Model structure of Yukawa couplings y_f onto the mediator couplings to SM fermions, i.e. by assuming those couplings to be proportional to the fermion masses. The relevant terms in the Lagrangian of this model read

$$\mathcal{L}_{\text{DM/SM}} = -\sum_f \frac{y_f}{\sqrt{2}}\left(g_v^{\phi}\phi\bar{f}f + ig_v^{A}\bar{f}\gamma_5 f A\right) - g_\chi^{\phi}\phi\bar{\chi}\chi - ig_\chi^{A}\bar{\chi}\gamma_5\chi A. \tag{5.10}$$

In (5.10), the summation is understood to be over all Standard Model fermions f. g_v^A and g_v^ϕ are the SM fermion coupling strengths of the pseudoscalar mediator A, and the scalar mediator ϕ, respectively. The mediators couple to the Dirac Dark Matter particle with coupling strengths g_χ^A and g_χ^ϕ. At the LHC, interactions of the form (5.10) lead to various signatures with missing transverse energy. Since the scalar mediators have essentially the same couplings to SM fermions as the Higgs boson, there are also Z-associated Dark Matter production channels with an intermediate scalar mediator. These channels are very similar to Z-associated Higgs production in the Standard Model and the corresponding collider signatures are identical to those studied in the previous section. The analysis presented in section 5.5 is therefore directly applicable. The absence of a tree-level scalar-Z-coupling for the Dark Matter Mediator implies the absence of tree-induced contributions to the $pp \to l^+l^-\chi\bar{\chi}$ signal process, however. Triangle diagrams with an intermediate Z coupling to the quark loop as displayed in figure 5.2a are also absent. Figure 5.16 shows two example Feynman diagrams contributing to the signal process, i.e. Dark Matter pair production in association with a dilepton pair.

Technically, the simulation of the simplified Dark Matter signal can be achieved by modifying the Z-Higgs coupling and the top-Higgs coupling in a Standard Model calculation by factors of κ_V and κ_t, respectively. Setting $\kappa_t = 1$, $\kappa_V = 0$, and $m_h = m_{\phi/A}$ in the Standard Model simulation, one can calculate the on-shell production cross section for the mediator in the simplified Dark Matter model with a scalar mediator. In order to accommodate a pseudoscalar, one needs to adapt the Lorentz-structure of the fermion-Higgs coupling. These functionalities were implemented in OpenLoops in order to facilitate this study. Working in the narrow-width-approximation and assuming $\mathcal{BR}(h \to \text{inv}) = \mathcal{BR}(\phi/A \to \chi\bar{\chi}) = 1$, one can perform the entire calculation with on-shell mediators, since the decay products of the scalars are not reconstructed in the analysis.

For illustration purposes, the missing transverse energy distribution for a scalar mediator of mass $m_\phi = 125\,\text{GeV}$ for $(\kappa_t, \kappa_V) \in \{(1,1),(0,1),(1,0)\}$ after applying the event selection cuts described in section 5.5 is shown in figure 5.17. Note that $(\kappa_t, \kappa_V) = (1,1)$ corresponds to a Standard Model invisible Higgs decay signal. From figure 5.17 it is evident that, in the tail

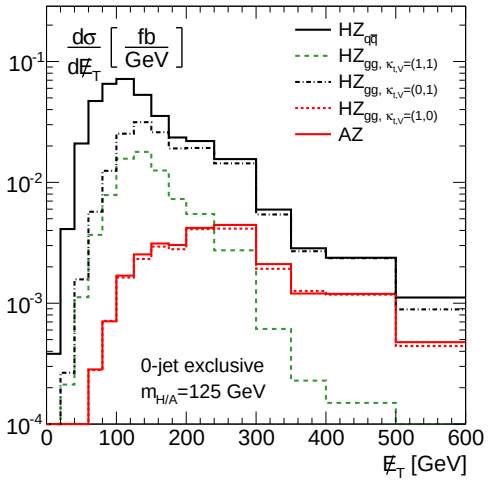

Figure 5.17: Transverse missing energy distribution (labelled $\not{E}_T$ in this figure) after applying the selection cuts of the analysis described in section 5.5. Individual curves are shown for the loop-induced signal (labelled HZ_{gg} in this figure) with a scalar mediator and $(\kappa_t, \kappa_V) \in \{(1,1),(0,1),(1,0)\}$ as described in the text. For $(\kappa_t, \kappa_V) = (1,0)$, i.e. the simplified Dark Matter model, results for a pseudoscalar mediator are shown as well. The Standard Model signal arising from the tree-induced HZ process with an invisibly decaying Higgs is included for reference (labelled $\mathrm{HZ}_{q\bar{q}}$).

of the distribution, the contributions involving the Z-coupling interfere destructively with those involving the heavy quark couplings of the mediator. As a consequence, the simplified Dark Matter signal is enhanced in the tail compared to the Standard Model Higgs invisible decay signal. For $(\kappa_t, \kappa_V) = (1,0)$, i.e. the simplified Dark Matter model, the pseudoscalar signal is displayed in figure 5.17 as well. It is very similar to the scalar signal with relative differences below 10 % throughout the displayed range of missing transverse energy.

In order to assess the Run-II sensitivity of the analysis described in section 5.5 in the context of simplified Dark Matter models, a two-dimensional binned log-likelihood analysis based on the missing transverse momentum distributions in exclusive jet bins was performed. This analysis was carried out using the same techniques and the same background predictions that were used in order to obtain the limits presented in section 5.5. An integrated luminosity of $100\,\mathrm{fb}^{-1}$ was assumed. Working in the narrow-width-approximation and assuming $\mathcal{BR}(\phi/A \to \chi\bar{\chi}) = 1$, exclusion limits only depend on the parameters that alter the mediator production cross section, i.e. on the mediator mass and its coupling to SM fermions $g_v^{\phi/A}$. This dependence is illustrated in figure 5.18, which shows the expected 95 % CL upper limit on g_v as a function of the mediator mass $m_{\phi/A}$ for scalar and pseudoscalar

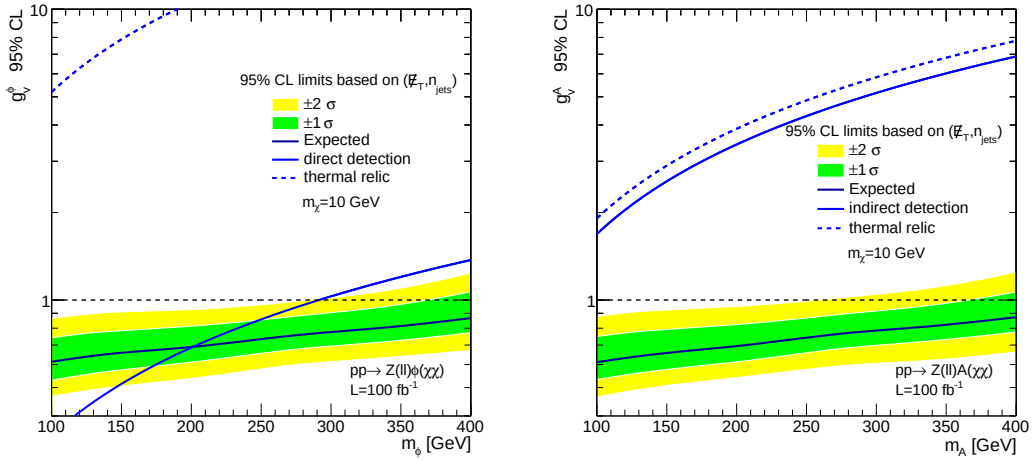

Figure 5.18: Expected 95 % CL upper limit on the mediator coupling to fermions g_v as a function of the mediator mass $m_{\phi/A}$ for a simplified Dark Matter model with a scalar (left) and a pseudoscalar mediator (right). For comparison, the 95 % CL upper limits of the LUX direct detection experiment [305] is shown along with 95 % CL upper limits set by the FermiLAT indirect detection experiment [306]. Furthermore, the value of g_v required in order to reproduce observed Dark Matter thermal relic density is also shown in both cases as a function of the mediator mass.

mediators. $g_v^{\phi/A}$ be constrained to values below 1 in all of the considered mediator mass range, i.e. between 100 GeV and 400 GeV. The bounds on models with a mediator of scalar and pseudoscalar nature are very similar as a result of their similar transverse momentum distributions.

In order to put the collider bounds into context, the non-collider bounds of references [291, 292] are shown in figure 5.18 as well. They include limits from both direct and indirect detection experiments. Direct detection experiments constrain the Dark-Matter nucleon scattering cross sections, which depend on $g_\chi^{\phi/A}$ and m_χ in addition to $g_v^{\phi/A}$ and the mediator mass $m_{\phi/A}$. This also applies to the indirect detection experiments considered here, which constrain thermally averaged Dark Matter annihilation cross sections into Standard Model particles. In order to facilitate a simple comparison with direct and indirect detection experiments, a scenario with $g_\chi^{\phi/A} = g_v^{\phi/A}$ and $m_\chi = 10\,\text{GeV}$ is assumed. Having made this choice, the limits from both types of experiments can be translated into limits on $g_v^{\phi/A}$ as a function of the mediator mass.

The strongest direct detection bounds on the scalar mediator scenario in the relevant Dark Matter mass range are set by the LUX experiment [305]. No direct detection bounds on

the pseudoscalar scenario are shown in figure 5.18 because the relevant scattering cross sections are suppressed by factors of the relative nucleon-DM velocity, which is of the order of 10^{-3}. The indirect detection bounds shown in figure 5.18 are from limits on the Dark matter annihilation cross section into bottom quarks set by the Fermi Large Area Telescope experiment [306]. This bound is only relevant for the pseudoscalar scenario because the relevant Dark Matter annihilation cross sections are velocity suppressed for a scalar-mediated interaction.

The Dark Matter abundance observed in the present-day universe can be translated into an estimate of the total thermally averaged Dark Matter annihilation cross section into Standard Model particles [307]. A canonically quoted estimate is $\langle \sigma v \rangle \approx 3 \times 10^{-26}\,\mathrm{cm}^3/\mathrm{s}$. For reference, the value of $g_V^{\phi/A}$ that reproduces this value is included in figure 5.18 as a function of the mediator mass and assuming $g_v^{\phi/A} = g_\chi^{\phi/A}$.

Under the aforementioned assumptions, the expected LHC bounds are very strong in comparison to non-collider limits. Only for scalar mediators with masses below 200 GeV are direct detection bounds stronger. For the pseudoscalar model, the expected LHC bounds are stronger than non-collider bounds throughout the explored region of mediator masses. Furthermore, the analysis discussed here is sensitive to parameters ranges that are required in order to obtain the correct thermal relic density.

5.7 Conclusions

Current measurements of the Higgs branching fraction into invisible states leave ample room for new physics in the Higgs sector. Additional measurements of the invisible Higgs branching fraction are therefore of major importance for the LHC Run-II. For these measurements, the Z-associated Higgs production mode is one of the key channels. In this work it was shown that loop-induced contributions to the background and in particular to the signal are significant for this channel. Both of these additional contributions should be taken into account when deriving limits on the invisible Higgs branching fraction. It was shown that merging techniques are indispensable when modeling the QCD radiation patterns of the loop-induced contributions. Key jet observables like the missing transverse energy distribution of the signal have proven to be sensitive to the matrix element corrections implemented by the merging. Using these state-of-the-art Monte Carlo simulation techniques, the sensitivity of the Z-associated production channel was estimated using an analysis that largely follows the Run-I analyses performed by ATLAS and CMS. It was found that with only $10\,\mathrm{fb}^{-1}$ of integrated luminosity in Run-II, the invisible Higgs branching ratio can be constrained to values below 0.3.

Furthermore, it was shown that the same analysis can be used in order to constrain the

parameter space of simplified Dark Matter models with scalar mediators. In these models, the signal process of Z-associated Dark Matter production is entirely loop-induced and a reliable modeling of loop-induced processes is of even higher priority. Based on an integrated luminosity of $100\,\text{fb}^{-1}$, it was shown that a 13 TeV LHC collider analysis can significantly constrain the simplified Model parameter space and that collider bounds are competitive with bounds derived from non-collider experiments.

6 Rare Higgs Decays into Light Resonances

The aim of the work presented in this section is an assessment of the LHC's potential of observing Higgs boson decays into light resonances through their hadronic decay channels. The motivation to consider these decays is twofold.

Firstly, Higgs decays into composite light quarkonia are predicted by the Standard Model. Such decays involve the Yukawa couplings of the quarkonia constituent quarks and have therefore been proposed as a probe for measuring Higgs boson couplings to first and second-generation quarks [308, 309]. However, for Standard Model couplings, the branching ratios for exclusive Higgs boson decays are generally very small, e.g $\mathcal{BR}(h \to Z\,\eta_c) \approx 1.4 \times 10^{-5}$, $\mathcal{BR}(h \to \rho^0\gamma) \approx 1.68 \times 10^{-5}$ or $\mathcal{BR}(h \to J/\psi\ \gamma) \approx 2.95 \times 10^{-6}$, rendering such analyses challenging [308, 310, 311]. Nevertheless, both general purpose experiments at the LHC have performed searches for exclusive Higgs boson decays, focusing on the dimuon decays of vector quarkonia. Using Run-I data, the ATLAS collaboration has set 95 % confidence level upper limits of $\mathcal{O}(10^{-3})$ on the branching ratios $\mathcal{BR}(h \to J/\psi\ \gamma)$ and $\mathcal{BR}(h \to \Upsilon(1S, 2S, 3S)\ \gamma)$ [312], while the CMS collaboration obtained a similar upper limit for $\mathcal{BR}(h \to J/\psi\ \gamma)$ [313].

Secondly, Higgs boson decays into elementary light resonances are predicted by many extensions of the SM [314]. They arise generically in scenarios with multiple Higgs fields. In the NMSSM, Higgs boson decays into an additional light CP-odd scalar can occur. Close to the alignment limit of the Two-Higgs-Doublet Model (2HDM) of Type I or II, a light CP-odd scalar with a mass of a few GeV can also be phenomenologically accommodated along with a 125 GeV SM-like Higgs boson h [315].

Hence, rare decays of Higgs bosons into light elementary or composite resonances are of direct relevance for the two most important tasks of the upcoming LHC runs, namely precision measurements of the Higgs boson properties, and searches for new physics.

While most existing search strategies rely upon resonance decays into leptons, the total width of most composite resonances and elementary scalars is dominated by decays into hadronic final states, e.g. $\mathcal{BR}(\eta_c \to \text{hadrons}) > 52\%$[1] [316]. Instead of exploiting only leptonic decay modes, one should therefore consider inclusive hadronic decays as well. Light

[1] Based on a simple sum of the branching fractions for the observed decays of the η_c into stable hadrons

resonances X with masses m_X below or around 10 GeV are highly boosted if produced in the decay of a SM Higgs boson with a mass of 125 GeV. The decay products of X are thus confined within a small area of the detector. The angular separation of the decay products of the resonance X scales like $\Delta R = \sqrt{\Delta\eta^2 + \Delta\phi^2} \sim 4m_X/m_h$, where η is the pseudorapidity and ϕ the azimuthal angle. Separating the decay products in the calorimeters of the detector poses a challenge, as the typical size of hadronic calorimeter cells is 0.1×0.1 in the η-ϕ-plane. Thus, to discriminate two jets the angular separation of their axes has to be roughly $\Delta R \gtrsim 0.2$. If opening angles are smaller, the total energy deposit of the resonance's decay products can still be measured, but the substructure, i.e. the energy sharing between the decay products, becomes opaque. To maintain the ability to separate between signal and QCD-induced backgrounds, a track-based reconstruction is proposed. Trajectories of charged particles as measured in the tracking detectors provide a much better spatial resolution than the reconstructed calorimeter clusters. Recently, a similar approach was advocated for highly boosted electroweak scale resonances [317–320].

In this work, track-based reconstruction techniques are used to evaluate the sensitivity of general purpose detectors at hadron colliders, with characteristics similar to those of ATLAS [13] and CMS [14], in measuring rare Higgs boson decays into light hadronically decaying resonances. Focusing on the high luminosity LHC (HL-LHC) regime, the analysis assumes a data set corresponding to an integrated luminosity of $3000\,\text{fb}^{-1}$ collected at centre-of-mass energy $\sqrt{s} = 13\,\text{TeV}$. Two Higgs boson production channels are considered: inclusive Higgs production and Higgs production in association with a hard jet of transverse momentum $p_T > 150\,\text{GeV}$. As two benchmark cases for rare Higgs boson decays into light resonances, the decays $h \to Z(\to \ell\ell) + \eta_c$ and $h \to Z(\to \ell\ell) + A$ are considered, where A is assumed to be an elementary CP-odd scalar of mass 4 GeV which decays mostly hadronically. The characteristics of the $h \to Z(\to \ell\ell) + \eta_c$ benchmark are expected to be representative of similar decays to vector charmonia (e.g. $h \to Z(\to \ell\ell) + J/\Psi$), due to similarities in their hadronic decay patterns and small mass differences.

6.1 Simulation Setup

For the simulation of both the signal and the background contributions, the Sherpa Monte Carlo is used. Parton shower effects, hadronisation, as well as underlying event contributions are taken into account throughout. Both Higgs boson production processes, h+jet and inclusive h, are calculated at NLO and matched to the parton shower. Finite top quark mass effects in the gluon fusion production mechanism are taken into account as described in section 4 and reference [2]. The Higgs boson decays $h \to Z\,\eta_c$, $h \to ZA$ as well as the subsequent decays of the elementary pseudoscalar A and the Z boson are calculated perturbatively at

leading order using the algorithm and methods described in chapter 3 and reference [1]. For the elementary pseudoscalar, decays into $c\bar{c}$ pairs and decays into gluons via an effective heavy-quark mediated interaction are considered separately. The decay of the η_c is simulated by the hadron decay module of Sherpa after the parton shower step. The parton shower therefore does not affect the kinematics of the η_c decay products. This in contrast to the elementary pseudoscalar A, whose decay products can radiate during the parton shower before hadronising. For the implementation of a pseudoscalar and its interactions, the UFO model format and the methods described in chapter 3 were used [1, 128].

For the inclusive Z boson background, the full dilepton final state is taken into account in the matrix elements and the core process is calculated at NLO. Additional hard jet emissions are accounted for by means of multi-jet merging techniques [90]. Leading order matrix elements with up to two additional jets are included in the setup.

The generated event samples are further processed with the Delphes detector simulation framework [321], which uses parametrised descriptions of the response of particle physics detectors to provide reconstructed physics objects, allowing a realistic data analyses to be performed. As an example of a general purpose LHC detector, the default ATLAS configuration card included in Delphes is used.

6.2 Reconstruction Setup and Selection

Leptonic Z Boson Decay Reconstruction

The reconstruction of $Z \to \ell\ell$ decays begins with the identification of isolated lepton (electron or muon) candidates. Reconstructed leptons are required to satisfy $p_T > 6\,\text{GeV}$ and $|\eta| < 2.5$. An isolation requirement based on the presence of reconstructed tracks and calorimeter deposits within $\Delta R < 0.2$ of a lepton is imposed. The sum of the transverse momentum of such objects is required to be less than 10 % of the transverse momentum of the lepton itself. Oppositely charged pairs of isolated leptons, which satisfy $81\,\text{GeV} < m_{\ell\ell} < 101\,\text{GeV}$ are identified as Z boson candidates.

Hadronic Resonance Reconstruction

The reconstruction of hadronically decaying resonances begins with a search for anti-k_t calorimeter jets with $R = 0.4$, seeded by clusters of calorimeter energy deposits. Calorimeter jets are required to have $p_T > 30\,\text{GeV}$ and $|\eta| < 2.5$. Any jets which are within $\Delta R < 0.3$ of leptons forming a $Z \to \ell\ell$ candidate are rejected. Following the identification of a calorimeter jet, the jet constituents are used to seed a search for an anti-k_t calorimeter jets with $R = 0.2$. The identification of an $R = 0.2$ jet from the constituents of the initial $R = 0.4$ jet is required

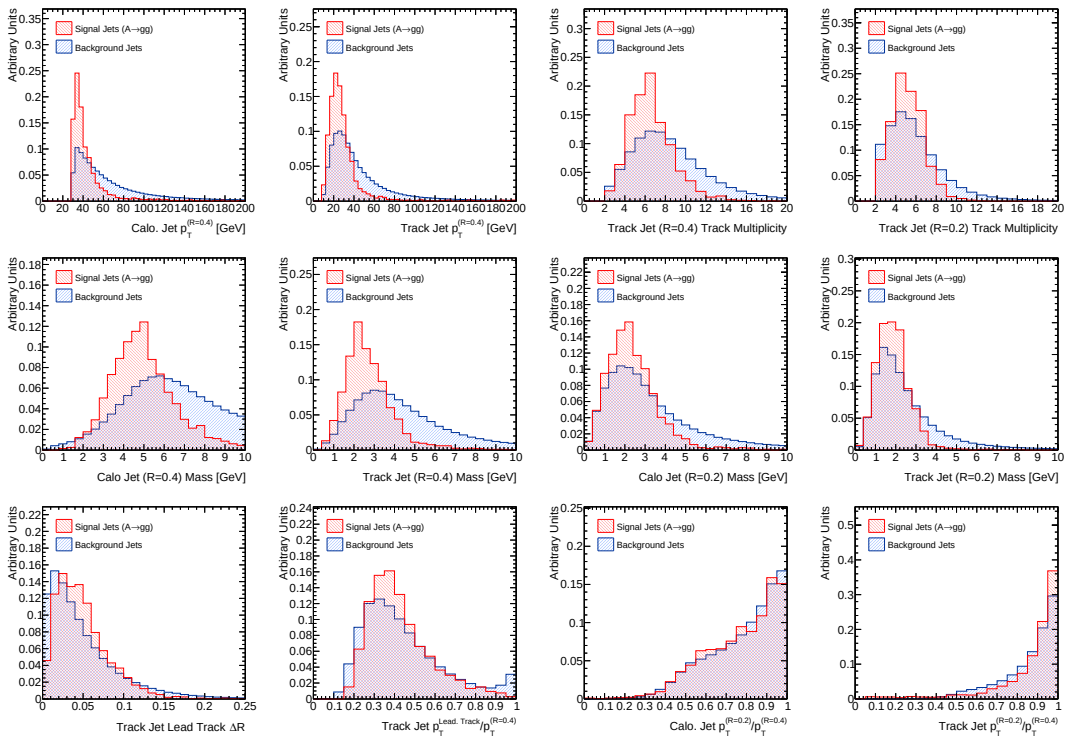

Figure 6.1: Distributions of input variables used as input to the BDT training for jets from $A \to gg$ decays and jets produced in association with Z bosons.

to be successful. This procedure, i.e. the reconstruction of anti-k_t $R = 0.2$ jets from the constituents of identified $R = 0.4$ jets, is repeated for track jets, seeded by reconstructed charged particles. Track jets are associated to calorimeter jets by a simple spatial matching, based on a requirement of $\Delta R < 0.4$ between the axes of the $R = 0.4$ calorimeter and track jets. Only jets reconstructed with both calorimeter and track components are considered for further analysis and at least one such jet is required to be reconstructed. As mentioned previously, the hadronic decay products of the light resonance are expected to be highly boosted and hence confined within a small radius jet. The two jet reconstruction steps with different radii $R = 0.4$ and $R = 0.2$ are therefore expected to yield jets with similar properties in case of the signal, since the highly collimated decay products are clustered into the jet in both cases. In case of background jets, one can expect a more significant amount of radiation contained in the $R = 0.4$ jet to be lost when reconstructing the narrow jet with $R = 0.2$.

To distinguish hadronically decaying charmonium states or light scalars from the copious production of low p_T background jets, a boosted decision tree (BDT) is employed through the TMVA package [322]. The following variables are used as input to the BDT:

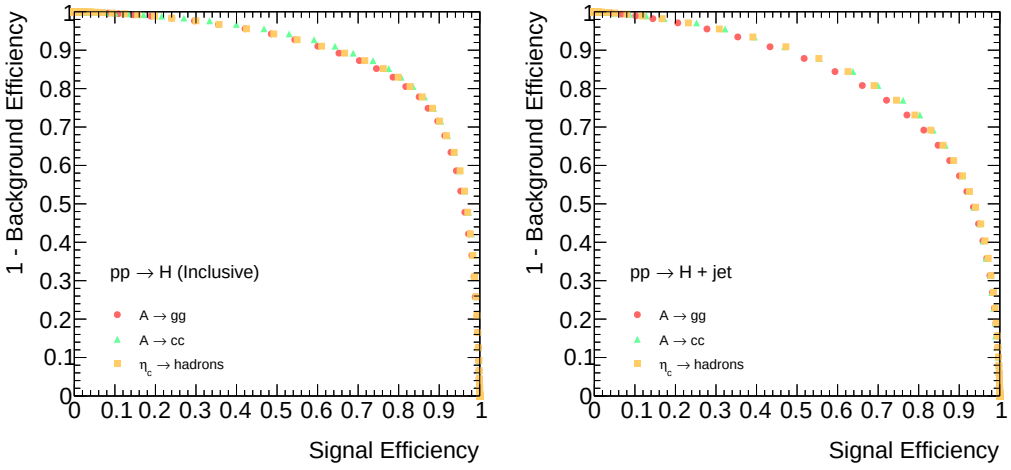

Figure 6.2: The background rejection as a function of signal efficiency for the low mass resonances considered for the inclusive (left) and h + jet (right) production channels. Separate curves are shown for the $h \to \eta_c Z$ channel and the $h \to ZA$ channel. The two partonic decay channels of A are also considered separately.

- The p_T of the $R = 0.4$ and track and calorimeter jets
- The number of track constituents associated with the $R = 0.4$ and $R = 0.2$ track jets
- The masses of the $R = 0.4$ and $R = 0.2$ track and calorimeter jets
- The ratio of the $R = 0.2$ calorimeter (track) jets p_T to the p_T of the associated $R = 0.4$ calorimeter (track) jet
- The spatial separation, ΔR, between the leading p_T track within the $R = 0.4$ track jet and the jet axis
- The ratio of the highest track p_T to the p_T of the $R = 0.4$ track jet

The BDT was trained with the inclusive Higgs production sample and the Z+jets sample as input before the leptonic Z boson reconstruction. The hadronic reconstruction described here can therefore be used as a generic hadronic tagger and is not tied to a particular production channel.

Examples of the distributions of the variables used to train the BDT are shown in figure 6.1. The performance of the BDT is summarised in figure 6.2, where the background rejection efficiency is shown as a function of the signal efficiency. As demonstrated in this figure, the performance of the analysis is insensitive to the modelling of the hadronic decay of the light resonances. Very similar efficiency curves are obtained for the composite η_c and for the

elementary A, despite the fact that no parton showering is involved in the treatment of the decay products of the η_c. Similarly, the partonic decay channel chosen for the pseudoscalar, being either $A \to c\bar{c}$ or $A \to gg$, affects the result only very little.

Selection of $h \to ZA$ and $h \to Z\,\eta_c$ Decays

Events containing at least one hadronic decay candidate and one $Z \to \ell\ell$ candidate are considered for further analysis. In the case of the h + jet production channel, an additional $R = 0.4$ anti-k_t calorimeter jet with $p_T > 150$GeV and $|\eta| < 2.5$ is required (no substructure or matching track jet is required). The single Z boson candidate with $m_{\ell\ell}$ closest to the Z boson mass is chosen to form the $h \to ZA(\eta_c)$ candidate. If multiple hadronic decay candidates are reconstructed, the candidate which when paired with the $Z \to \ell\ell$ candidate has an invariant mass closest to $m_h = 125$GeV is chosen. Finally, the transverse momentum of the h candidate is required to exceed 20 GeV. The invariant mass of the jet-dilepton system is shown for the inclusive and h + jet production channels in figure 6.3.

The BDT response is shown for both the signal and background contributions to the inclusive and h + jet production channels in figure 6.4.

6.3 Statistical Analysis and Results

The expected performance of the analysis is used to evaluate expected 95 % CL limits on the branching fractions $\mathcal{BR}(h \to ZA)$ and $\mathcal{BR}(h \to Z\eta_c)$. When deriving the former, $\mathcal{BR}(A \to gg) = 1.0$ or $\mathcal{BR}(A \to c\bar{c}) = 1.0$ are assumed. The yields of signal and background events within a reconstructed Higgs mass window of $110\,\text{GeV} < m_{\ell\ell j} < 140\,\text{GeV}$ are used to evaluate the limits. To exploit the additional sensitivity offered by the BDT, a requirement on the BDT response is imposed. The value of this requirement is optimised to provide the best limit on the branching fractions of interest. The expected 95 % CL limits on the branching fractions of interest are shown table 6.1. Branching fraction limits at the 1 % level can be expected. The inclusive production channel is found to be slightly more sensitive than the h + jet channel.

In addition to the production channels described, Higgs boson production in association with a leptonically decaying Z boson was also considered as a possible channel to gain additional sensitivity. Initial studies into this channel demonstrated improved signal to background ratios when compared to the two channels constituting the main study, though the substantially lower number of signal events resulted in expected branching fraction limits that were up to an order of magnitude higher than the the inclusive and h + jet channels.

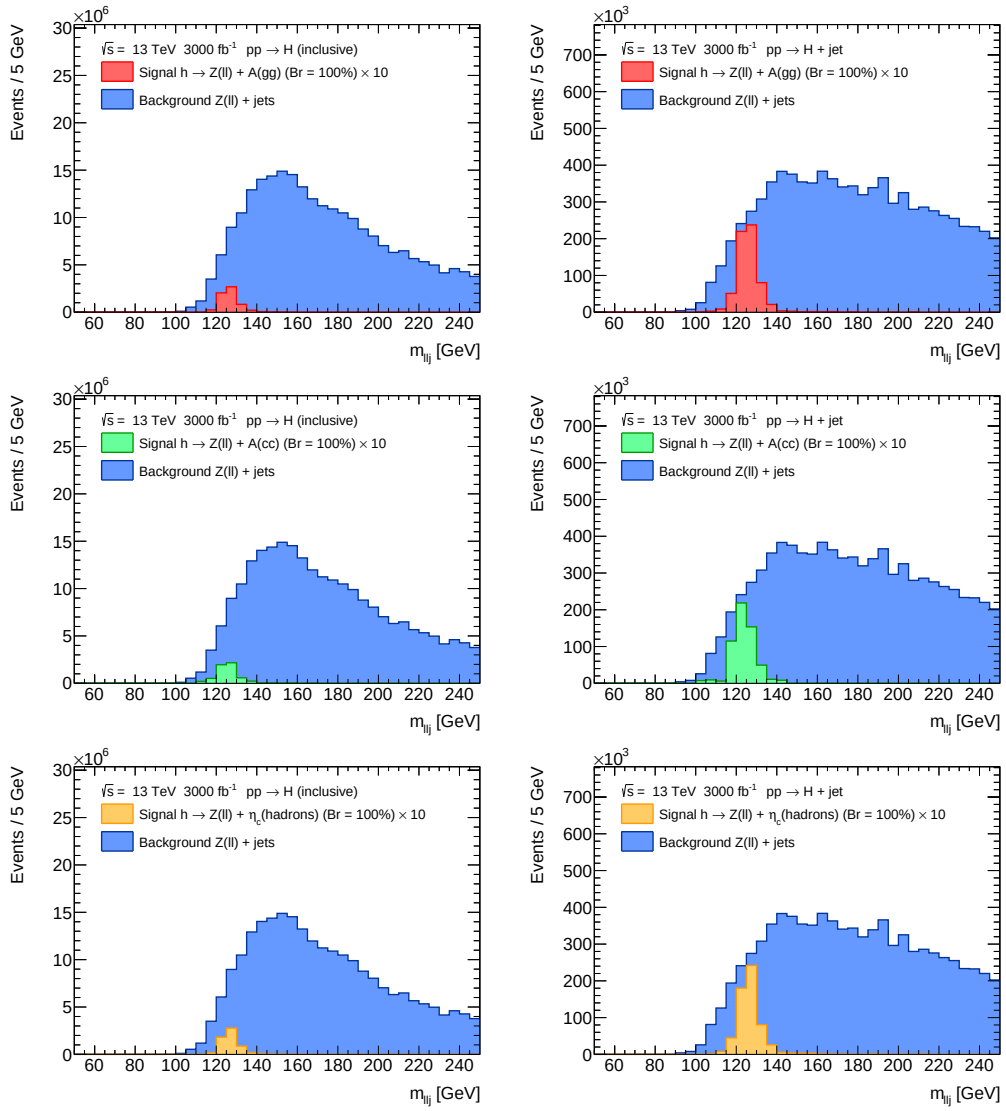

Figure 6.3: The invariant mass distribution of the jet-dilepton system (with no BDT based selection applied) in inclusive h production (left) and h + jet production (right) is shown for $A \to gg$ (top), $A \to c\bar{c}$ (middle) and $\eta_c \to$ hadrons (bottom) signals in comparison to the background contribution.

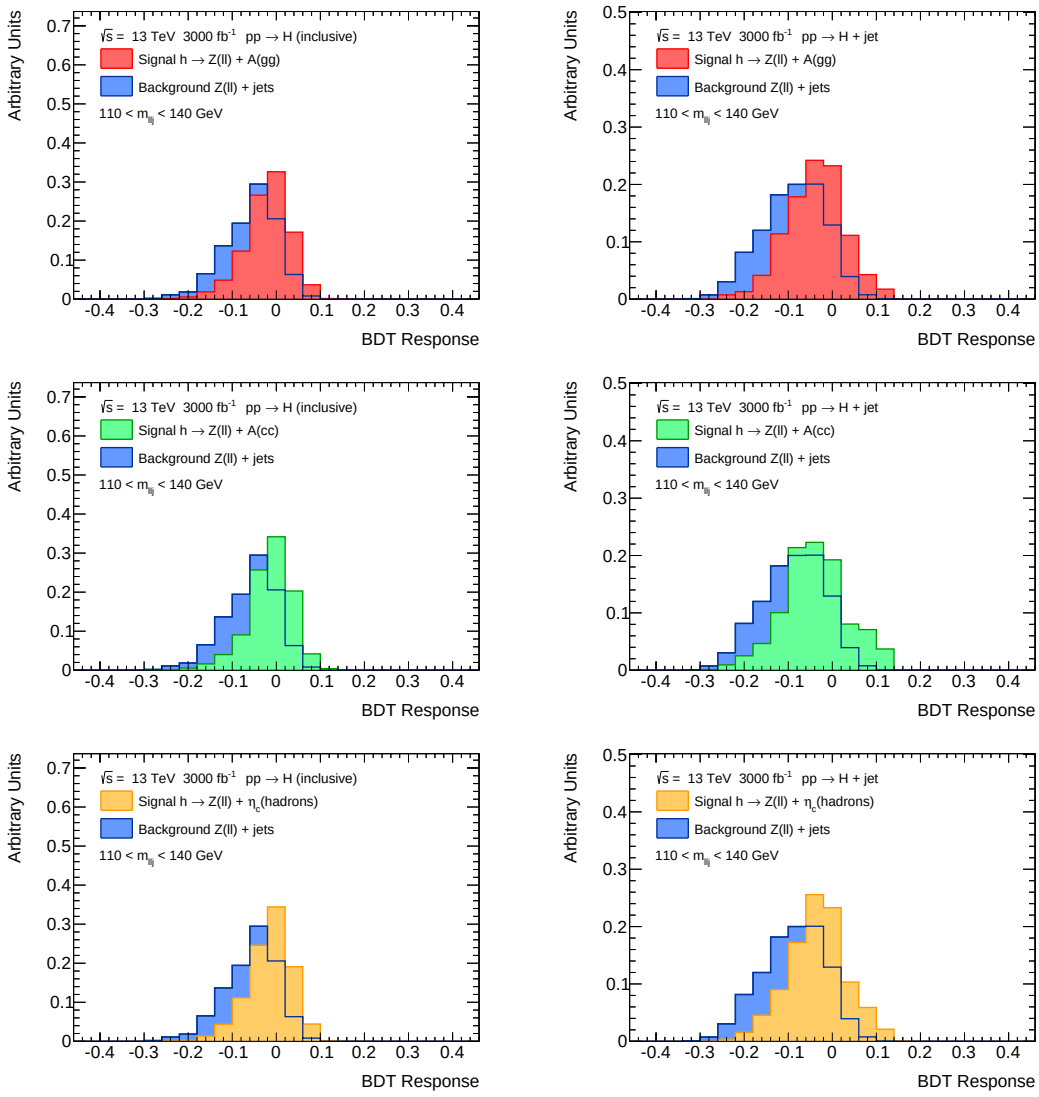

Figure 6.4: The normalised BDT response for the inclusive (left) and h+jet (right) production shown for $A \to gg$ (top), $A \to c\bar{c}$ (middle) and $\eta_c \to$ hadrons (right) in comparison to the background.

Channel	$h \to ZA(\to gg)$	$h \to ZA(\to c\bar{c})$	$h \to Z\,\eta_c$
Inclusive	2.0%	2.1%	2.0%
h + jet	3.6%	3.7%	3.7%

Table 6.1: The expected 95 % CL limits on the branching fractions of interest for both the inclusive and h + jet channels, assuming 3000 fb^{-1} at $\sqrt{s} = 13\,\text{TeV}$.

6.4 Constraints on the 2HDM Parameter Space

With a focus on the HL-LHC, it is assumed here that the Higgs boson couplings be tightly constrained to SM-like values. Assuming no evidence for new physics in the HL-LHC data, any 2HDM scenario compatible with the observations would therefore necessarily be close to the alignment limit. It has been pointed out in reference [315] that a light pseudoscalar A with mass below 10 GeV can be accommodated in this limit, particularly in Type I models, which are considered here. However, to the author's knowledge, no detailed analysis for this final state has been provided so far. In this mass range, the pseudoscalar has a considerable hadronic branching fraction and the results of our analysis can therefore be used in order to constrain such models. The hadronic decays of the light pseudoscalar proceed dominantly through quarks instead of gluons in the relevant parameter region. As shown in figure 6.2, the analysis presented here is, however, largely insensitive to these details.

In order to assess the constraining power of the analysis described above in this context, a 2HDM parameter scan for a fixed pseudoscalar mass of $m_A = 4\,\text{GeV}$ was performed. For each parameter point, the branching ratio relevant for the interpretation of our results, $\mathcal{BR}(h \to ZA)$, was calculated. At tree level, the corresponding partial decay width is given by

$$\Gamma(h \to ZA) = \frac{|\boldsymbol{p}|}{8\pi m_h^2} |\mathcal{M}(h \to ZA)|^2 = \frac{g_{hZA}^2}{2\pi} \frac{|\boldsymbol{p}|^3}{m_Z^2}, \tag{6.1}$$

where $\boldsymbol{p}$ is the three-momentum of either of the two decay products in the rest frame of the Higgs boson. Using the usual parametrisation of the 2HDM in terms of physical masses and the angles α and β [323], the hZA-coupling in the is given by

$$g_{hZA} = \frac{e \cos(\beta - \alpha)}{2 \cos\theta_W \sin\theta_W}. \tag{6.2}$$

The partial decay width $\Gamma(h \to ZA)$ therefore vanishes in the strict alignment limit, where $\cos(\beta - \alpha) = 0$. The corresponding branching fraction, however, can reach values of the order of a few per cent already for small $\cos(\beta - \alpha)$, especially if the decay $h \to AA$ does not contribute substantially to the Higgs boson's total width. The focus will therefore be on the

parameter region where $g_{hAA} = 0$ at tree level, which implies [324]

$$m_{12}^2 = (2m_A^2 + m_h^2)\sin(2\beta)/4.0\,. \tag{6.3}$$

To ensure alignment, a uniform scan with $\sin(\beta-\alpha) \in [0.99, 1.0]$ is performed. In this regime, one can assume the production cross sections of the 125 GeV-Higgs to be SM-like and directly apply the previously obtained limit on $\mathcal{BR}(h \to ZA)$. Note, however, that the limit must be applied to $\mathcal{BR}(h \to ZA) \times \mathcal{BR}(A \to \text{hadrons})$, since $\mathcal{BR}(A \to \text{hadrons}) = 1$ was assumed previously. When determining $\mathcal{BR}(A \to \text{hadrons})$, indirect hadronic decays through τ-leptons are also included, which gives $\mathcal{BR}(A \to \text{hadrons}) \approx 82\,\%$. The remaining free parameters of the model are uniformly varied in the intervals $m_H \in [130, 600]$GeV, $m_{H^\pm} \in [50, 600]$GeV, and $\tan\beta \in [0.1, 5.0]$. The physical spectrum and the relevant branching fractions are calculated with 2HDMC version 1.7.0 [325].

For each point, consistency checks for vacuum stability of the potential and tree-level unitarity are performed using the corresponding functionalities of 2HDMC. Experimental constraints on the electroweak oblique parameters S, T, U [326, 327], as calculated by 2HDMC, are taken into account. Only points that can be accommodated within these constraints are retained. Points that are incompatible with exclusion limits set by LEP, Tevatron, and LHC analyses are also rejected. For this purpose, the numerical program HiggsBounds [328–331] is employed. All analyses implemented in version 4.3.1 are taken into account. Only parameter points for which none of the scalars in the spectrum can be excluded at 95 % CL by any of the analyses are retained in our scan. In order to check for compatibility with LHC and Tevatron Higgs boson signals, the HiggsSignals program [332, 333] is employed. Any points that are excluded at 95 % confidence level based on the χ^2 calculated by HiggsSignals are discarded.

In figure 6.5, the results of the parameter scan are illustrated. The distribution of all parameter points that pass the applied theoretical and phenomenological constraints in a two-dimensional parameter plane spanned by $\cos^2(\beta-\alpha)$ and $\mathcal{BR}(h \to ZA) \times \mathcal{BR}(A \to \text{hadrons})$ is shown. Figure 6.5 also shows the tree-level functional dependence of these quantities given by equation (6.1), assuming for simplicity $\Gamma^h_{\text{tot}} = \Gamma^{h_{\text{SM}}}_{\text{tot}}$. For large $\cos(\beta-\alpha)$, this is assumption is violated due to the opening of further decay channels. At small $\cos(\beta-\alpha)$, however, the corresponding approximation proves to be reasonable for parameter points that pass the applied phenomenological constraints. As illustrated in figure 6.5, the scanned parameter space can effectively be constrained to very small values of $\cos^2(\beta-\alpha)$ by applying our expected limit on $\mathcal{BR}(h \to ZA)$. In fact, no parameter point with $\cos^2(\beta-\alpha) > 0.0035$ survives the limit set by the analysis presented above, translating to $\sin(\beta-\alpha) \gtrsim 0.998$ in the scanned subspace of parameters. Correspondingly, a mere 12 % of the parameter points displayed in figure 6.5 fall in the region of allowed values for $\mathcal{BR}(h \to ZA) \times \mathcal{BR}(A \to \text{hadrons})$

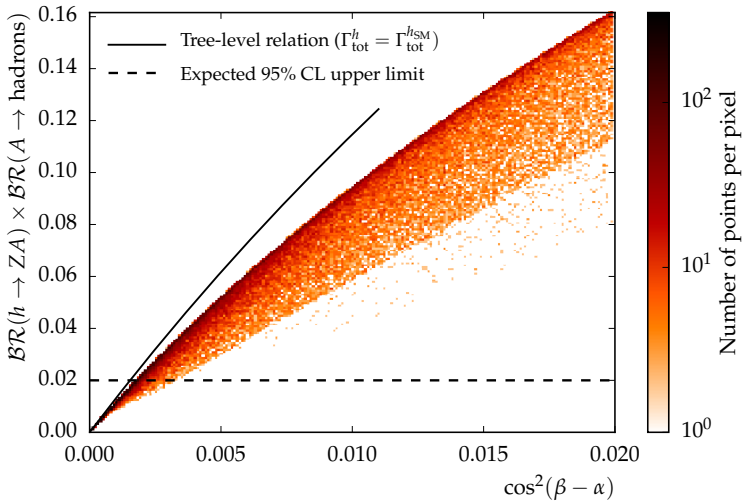

Figure 6.5: Distribution of scanned parameter points in the $\cos^2(\beta - \alpha)$ vs. $\mathcal{BR}(h \to ZA) \times \mathcal{BR}(A \to \text{hadrons})$ plane. The colour-coding denotes the density of points in the respective areas as indicated by the colour bar. The tree-level functional relationship between $\cos^2(\beta - \alpha)$ and $\mathcal{BR}(h \to ZA) \times \mathcal{BR}(A \to \text{hadrons})$, assuming $\Gamma^h_{\text{tot}} = \Gamma^{h_{\text{SM}}}_{\text{tot}}$ is shown as well. The dashed line shows the expected 95 % CL upper limit on the displayed branching fraction. All points above this line are expected to be excluded by the analysis presented here.

after applying the limit on $\mathcal{BR}(h \to ZA)$.

6.5 Conclusions

Searches for rare and exclusive Higgs boson decays are at the core of the program of the high luminosity LHC. The observation of Higgs boson decays into light elementary or composite resonances would be evidence for the existence of physics beyond the Standard Model.

While previous experimental strategies to reconstruct light resonances relied entirely on their leptonic decay products, the prospects for their discovery in the often dominant hadronic decay channels was assessed in this work. The focus was placed on Higgs boson production processes with the largest cross sections, $pp \to h$ and $pp \to h$+jet, with subsequent decays $h \to ZA$ or $h \to Z\eta_c$. The former is present in many multi-Higgs extensions of the Standard Model, while observing the latter at a branching ratio of $\mathcal{BR}(h \to Z\eta_c) \geq 10^{-3}$ could indicate an enhanced Higgs-charm coupling.

The decay products of light resonances with masses below a few GeV that arise from Higgs decays are highly collimated and get emitted into a small area of the detector. In such scenarios, jet substructure is an indispensable tool to retain sensitivity in discriminating

signal from large QCD-induced backgrounds. In particular, by exploiting the improved angular resolution of track-based observables, a good signal-to-background discrimination can be achieved, which results in a limit on the branching ratios of $\mathcal{O}(1)\%$ for a data sample corresponding to $3000\,\mathrm{fb}^{-1}$ at $\sqrt{s} = 13\,\mathrm{TeV}$. The limit on the branching fraction $\mathcal{BR}(h \to Z\,A)$ can be translated into tight constraints on a 2HDM parameter sub space in the alignment limit.

Summary and Outlook

A comprehensive new physics event generation framework based on the Sherpa Monte Carlo was presented in chapter 3 of this thesis. The framework is compatible with the widely used universal UFO BSM model format and supports a wide range of generic models. To facilitate event generation for models with arbitrary Lorentz structures, a new code generator for optimised Lorentz calculator routines was developed and integrated in the framework. The new fixed-order aspects of BSM event generation were thoroughly validated. It is left for future work to complete the last remaining steps towards a framework that supports event generation for completely arbitrary UFO models. This would require the implementation of spin-3/2 fields, the implementation of spin-2 external wave functions, and the generalisation of colour structures within the matrix element generator Comix.

In chapter 4, an implementation of heavy quark mass corrections to an effective description of the gluon fusion Higgs production mechanism was described. This implementation allows for an approximate treatment of finite top quark mass effects at NLO for Higgs production in association with an arbitrary number of jets, thus facilitating the generation of NLO multi-jet merged samples with finite top mass effects taken into account. In the approach presented, the effect of bottom quark loops is included at leading order. As an alternative to other methods proposed in the literature, multi-jet merging was considered in order to take into account the non-factorisation of amplitudes involving bottom loops in the resummation performed by the parton shower. A significant reduction of the associated uncertainties was thereby achieved. In a phenomenological study, the new implementation of finite top mass effects was used in order to assess the prospects of using the Higgs transverse momentum spectrum as a probe to constrain BSM models that introduce new particles which alter the loop-mediated Higgs-gluon coupling. While this strategy turned out to be feasible with a large data set collected at the LHC, it is likely that other more direct LHC analyses including top-associated Higgs production will be more competitive.

The new implementation of heavy quark mass effects in gluon fusion now allows for a meaningful description of the Higgs transverse momentum spectrum. A comparison of theory predictions to statistically significant LHC Run-II measurements of Higgs differential kinematics is therefore facilitated. The large perturbative uncertainties in gluon fusion Higgs

production even at NLO might, however, ultimately require NNLO calculations with finite heavy quark mass effects taken into account for the high luminosity phase of the LHC.

In chapter 5, loop-induced contributions to the Z-associated Higgs production channel and the corresponding backgrounds were scrutinised in the context of invisible Higgs decay searches. It was found that the loop-induced contributions have a significant impact on the bounds on the invisible Higgs branching fraction derived from LHC measurements. Furthermore, the impact of higher order corrections for loop-induced contributions was assessed using multi-jet merging techniques. While these techniques allowed to capture important and large effects of QCD real emission corrections on key differential distributions, the perturbative uncertainties remain large. In order to improve upon these uncertainties, full NLO calculations that involve the genuine two-loop contributions will be required in the future.

In chapter 6, a new strategy for measuring rare Higgs decays into light resonances was proposed. This strategy makes use of jet substructure techniques in order to exploit the often dominant hadronic decay modes of the light resonances of interest. It was found that Higgs branching fractions into light, hadronically decaying resonances can be constrained to the percent-level with a data set corresponding to an integrated luminosity of $3000\,\text{fb}^{-1}$ in the high luminosity phase of the LHC. Furthermore, it was shown that this constraint can be used to place severe bounds on a Two-Higgs-Doublet model in the alignment limit.

Bibliography

[1] Stefan Höche et al. 'Beyond Standard Model calculations with Sherpa'. *Eur. Phys. J.* C75.3 (2015), p. 135. arXiv: 1412.6478 [hep-ph].

[2] Malte Buschmann et al. 'Mass Effects in the Higgs-Gluon Coupling: Boosted vs Off-Shell Production'. *JHEP* 02 (2015), p. 038. arXiv: 1410.5806 [hep-ph].

[3] J. R. Andersen et al. 'Les Houches 2015: Physics at TeV Colliders Standard Model Working Group Report'. *9th Les Houches Workshop on Physics at TeV Colliders (PhysTeV 2015) Les Houches, France, June 1-19, 2015*. 2016. arXiv: 1605.04692 [hep-ph].

[4] Enrico Bothmann et al. 'Aspects of pQCD at a 100 TeV future hadron collider' (2016). arXiv: 1605.00617 [hep-ph].

[5] Dorival Goncalves et al. 'Higgs-Strahlung: Merging the NLO Drell-Yan and Loop-Induced 0+1 jet Multiplicities'. *Phys. Rev.* D92.7 (2015), p. 073006. arXiv: 1509.01597 [hep-ph].

[6] Dorival Goncalves et al. 'Boosting invisible searches via ZH: From the Higgs Boson to Dark Matter Simplified Models' (2016). arXiv: 1605.08039 [hep-ph].

[7] Andrew S. Chisholm et al. 'Measuring rare and exclusive Higgs boson decays into light resonances' (2016). arXiv: 1606.09177 [hep-ph].

[8] Lyndon Evans and Philip Bryant. 'LHC Machine'. *JINST* 3 (2008), S08001.

[9] Oliver S. Bruning et al. *LHC Design Report Vol.1: The LHC Main Ring*. Tech. rep. CERN, 2004.

[10] O. Buning et al. *LHC Design Report. 2. The LHC infrastructure and general services*. Tech. rep. CERN, 2004.

[11] M. Benedikt et al. *LHC Design Report. 3. The LHC injector chain*. Tech. rep. CERN, 2004.

[12] G Apollinari et al. *High-Luminosity Large Hadron Collider (HL-LHC) : Preliminary Design Report*. Tech. rep. CERN, 2015.

[13] G. Aad et al. 'The ATLAS Experiment at the CERN Large Hadron Collider'. *JINST* 3 (2008), S08003.

[14] S. Chatrchyan et al. 'The CMS experiment at the CERN LHC'. *JINST* 3 (2008), S08004.

[15] F. Englert and R. Brout. 'Broken Symmetry and the Mass of Gauge Vector Mesons'. *Phys. Rev. Lett.* 13 (1964), pp. 321–323.

[16] Peter W. Higgs. 'Broken symmetries, massless particles and gauge fields'. *Phys. Lett.* 12 (1964), pp. 132–133.

[17] Peter W. Higgs. 'Broken Symmetries and the Masses of Gauge Bosons'. *Phys. Rev. Lett.* 13 (1964), pp. 508–509.

[18] G. S. Guralnik, C. R. Hagen and T. W. B. Kibble. 'Global Conservation Laws and Massless Particles'. *Phys. Rev. Lett.* 13 (1964), pp. 585–587.

[19] Peter W. Higgs. 'Spontaneous Symmetry Breakdown without Massless Bosons'. *Phys. Rev.* 145 (1966), pp. 1156–1163.

[20] T. W. B. Kibble. 'Symmetry breaking in nonAbelian gauge theories'. *Phys. Rev.* 155 (1967), pp. 1554–1561.

[21] Serguei Chatrchyan et al. 'Observation of a New Boson at a Mass of 125 GeV with the CMS Experiment at the LHC'. *Phys. Lett.* B716 (2012), pp. 30–61. arXiv: 1207.7235 [hep-ex].

[22] Georges Aad et al. 'Observation of a new particle in the search for the Standard Model Higgs boson with the ATLAS detector at the LHC'. *Phys. Lett.* B716 (2012), pp. 1–29. arXiv: 1207.7214 [hep-ex].

[23] Georges Aad et al. 'Combined Measurement of the Higgs Boson Mass in pp Collisions at $\sqrt{s} = 7$ and 8 TeV with the ATLAS and CMS Experiments'. *Phys. Rev. Lett.* 114 (2015), p. 191803. arXiv: 1503.07589 [hep-ex].

[24] Vardan Khachatryan et al. 'Constraints on the spin-parity and anomalous HVV couplings of the Higgs boson in proton collisions at 7 and 8 TeV'. *Phys. Rev.* D92.1 (2015), p. 012004. arXiv: 1411.3441 [hep-ex].

[25] Georges Aad et al. 'Evidence for the spin-0 nature of the Higgs boson using ATLAS data'. *Phys. Lett.* B726 (2013), pp. 120–144. arXiv: 1307.1432 [hep-ex].

[26] Georges Aad et al. 'Measurements of the Higgs boson production and decay rates and constraints on its couplings from a combined ATLAS and CMS analysis of the LHC pp collision data at $\sqrt{s} = 7$ and 8 TeV' (2016). arXiv: 1606.02266 [hep-ex].

[27] Gerard Jungman, Marc Kamionkowski and Kim Griest. 'Supersymmetric dark matter'. *Phys. Rept.* 267 (1996), pp. 195–373. arXiv: hep-ph/9506380 [hep-ph].

[28] Lars Bergstrom. 'Nonbaryonic dark matter: Observational evidence and detection methods'. *Rept. Prog. Phys.* 63 (2000), p. 793. arXiv: hep-ph/0002126 [hep-ph].

[29] Gianfranco Bertone, Dan Hooper and Joseph Silk. 'Particle dark matter: Evidence, candidates and constraints'. *Phys. Rept.* 405 (2005), pp. 279–390. arXiv: hep-ph/0404175 [hep-ph].

[30] Steven Weinberg. 'Implications of Dynamical Symmetry Breaking'. *Phys. Rev.* D13 (1976), pp. 974–996.

[31] Steven Weinberg. 'Implications of Dynamical Symmetry Breaking: An Addendum'. *Phys. Rev.* D19 (1979), pp. 1277–1280.

[32] Eldad Gildener. 'Gauge Symmetry Hierarchies'. *Phys. Rev.* D14 (1976), p. 1667.

[33] Leonard Susskind. 'Dynamics of Spontaneous Symmetry Breaking in the Weinberg-Salam Theory'. *Phys. Rev.* D20 (1979), pp. 2619–2625.

[34] Georges Aad et al. 'Summary of the ATLAS experiment's sensitivity to supersymmetry after LHC Run 1 — interpreted in the phenomenological MSSM'. *JHEP* 10 (2015), p. 134. arXiv: 1508.06608 [hep-ex].

[35] S. P. Martin. *A Supersymmetry Primer*. 1997. arXiv: hep-ph/9709356 [hep-ph].

[36] T. Gleisberg et al. 'Event generation with SHERPA 1.1'. *JHEP* 02 (2009), p. 007. arXiv: 0811.4622 [hep-ph].

[37] F. James. 'Monte Carlo Theory and Practice'. *Rept. Prog. Phys.* 43 (1980), p. 1145.

[38] Ronald Kleiss and Roberto Pittau. 'Weight optimization in multichannel Monte Carlo'. *Comput. Phys. Commun.* 83 (1994), pp. 141–146. arXiv: hep-ph/9405257 [hep-ph].

[39] F. Krauss, R. Kuhn and G. Soff. 'AMEGIC++ 1.0: A Matrix element generator in C++'. *JHEP* 02 (2002), p. 044. arXiv: hep-ph/0109036 [hep-ph].

[40] Tanju Gleisberg and Stefan Hoeche. 'Comix, a new matrix element generator'. *JHEP* 12 (2008), p. 039. arXiv: 0808.3674 [hep-ph].

[41] J. Alwall et al. 'The Automated Computation of Tree-Level and Next-to-Leading Order Differential Cross Sections, and their Matching to Parton Shower Simulations'. *JHEP* 07 (2014), p. 079. arXiv: 1405.0301 [hep-ph].

[42] Mauro Moretti, Thorsten Ohl and Jurgen Reuter. 'O'Mega: An Optimizing Matrix Element Generator' (2001). arXiv: hep-ph/0102195 [hep-ph].

[43] Alexander Belyaev, Neil D. Christensen and Alexander Pukhov. 'CalcHEP 3.4 for Collider Physics within and beyond the Standard Model'. *Comput. Phys. Commun.* 184 (2013), pp. 1729–1769. arXiv: 1207.6082 [hep-ph].

[44] Fabio Cascioli, Philipp Maierhofer and Stefano Pozzorini. 'Scattering Amplitudes with Open Loops'. *Phys. Rev. Lett.* 108 (2012), p. 111601. arXiv: 1111.5206 [hep-ph].

[45] C. F. Berger et al. 'One-Loop Calculations with BlackHat'. *Nucl. Phys. Proc. Suppl.* 183 (2008), pp. 313–319. arXiv: 0807.3705 [hep-ph].

[46] Gavin Cullen et al. 'Automated One-Loop Calculations with GoSam'. *Eur. Phys. J.* C72 (2012), p. 1889. arXiv: 1111.2034 [hep-ph].

[47] Gavin Cullen et al. 'G*OSAM*-2.0: a tool for automated one-loop calculations within the Standard Model and beyond'. *Eur. Phys. J.* C74.8 (2014), p. 3001. arXiv: 1404.7096 [hep-ph].

[48] Valentin Hirschi et al. 'Automation of one-loop QCD corrections'. *JHEP* 05 (2011), p. 044. arXiv: 1103.0621 [hep-ph].

[49] Ansgar Denner, Stefan Dittmaier and Lars Hofer. 'COLLIER - A Fortran-Library for One-Loop Integrals'. *PoS* LL2014 (2014), p. 071. arXiv: 1407.0087 [hep-ph].

[50] Ansgar Denner, Stefan Dittmaier and Lars Hofer. 'Collier: a fortran-based Complex One-Loop LIbrary in Extended Regularizations' (2016). arXiv: 1604.06792 [hep-ph].

[51] Ansgar Denner and S. Dittmaier. 'Reduction of one loop tensor five point integrals'. *Nucl. Phys.* B658 (2003), pp. 175–202. arXiv: hep-ph/0212259 [hep-ph].

[52] Ansgar Denner and S. Dittmaier. 'Reduction schemes for one-loop tensor integrals'. *Nucl. Phys.* B734 (2006), pp. 62–115. arXiv: hep-ph/0509141 [hep-ph].

[53] A. Denner and S. Dittmaier. 'Scalar one-loop 4-point integrals'. *Nucl. Phys.* B844 (2011), pp. 199–242. arXiv: 1005.2076 [hep-ph].

[54] J. C. Collins, D. E. Soper and G. F. Sterman. 'Factorization of Hard Processes in QCD'. *Adv.Ser.Direct.High Energy Phys.* 5 (1988), pp. 1–91. arXiv: hep-ph/0409313 [hep-ph].

[55] Jeffrey R. Forshaw, Michael H. Seymour and Andrzej Siodmok. 'On the Breaking of Collinear Factorization in QCD'. *JHEP* 11 (2012), p. 066. arXiv: 1206.6363 [hep-ph].

[56] Guido Altarelli and G. Parisi. 'Asymptotic Freedom in Parton Language'. *Nucl. Phys.* B126 (1977), pp. 298–318.

[57] A. Bassetto, M. Ciafaloni and G. Marchesini. 'Jet Structure and Infrared Sensitive Quantities in Perturbative QCD'. *Physics Reports* 100 (1983), pp. 201–272.

[58] R. K. Ellis, B.R. Webber and W. J. Stirling. *QCD and Collider Physics*. Cambridge University Press, 1996.

[59] Y. L. Dokshitzer et al. *Basics of Perturbative QCD*. Editions Frontieres, 1991.

[60] Andrea Banfi, Gavin P. Salam and Giulia Zanderighi. 'Phenomenology of event shapes at hadron colliders'. *JHEP* 06 (2010), p. 038. arXiv: 1001.4082 [hep-ph].

[61] S. Catani et al. 'New clustering algorithm for multi - jet cross-sections in e+ e- annihilation'. *Phys. Lett.* B269 (1991), pp. 432–438.

[62] N. Brown and W. James Stirling. 'Finding jets and summing soft gluons: A New algorithm'. *Z. Phys.* C53 (1992), pp. 629–636.

[63] L. N. Lipatov. 'The parton model and perturbation theory'. *Sov. J. Nucl. Phys.* 20 (1975). [Yad. Fiz.20,181(1974)], pp. 94–102.

[64] V. N. Gribov and L. N. Lipatov. 'Deep inelastic e p scattering in perturbation theory'. *Sov. J. Nucl. Phys.* 15 (1972). [Yad. Fiz.15,781(1972)], pp. 438–450.

[65] Yuri L. Dokshitzer. 'Calculation of the Structure Functions for Deep Inelastic Scattering and e+ e- Annihilation by Perturbation Theory in Quantum Chromodynamics.' *Sov. Phys. JETP* 46 (1977). [Zh. Eksp. Teor. Fiz.73,1216(1977)], pp. 641–653.

[66] Torbjorn Sjostrand. 'A Model for Initial State Parton Showers'. *Phys. Lett.* B157 (1985), pp. 321–325.

[67] S. Catani et al. 'QCD Matrix Elements + Parton Showers'. *Journal of High Energy Physics* 0111 (2001), p. 063. arXiv: hep-ph/0109231 [hep-ph].

[68] F. Krauss. 'Matrix Elements and Parton Showers in Hadronic Interactions'. *Journal of High Energy Physics* 0208 (2002), p. 015. arXiv: hep-ph/0205283 [hep-ph].

[69] S. Hoeche et al. 'QCD Matrix Elements and Truncated Showers'. *Journal of High Energy Physics* 0905 (2009), p. 053. arXiv: 0903.1219 [hep-ph].

[70] Leif Lonnblad. 'Correcting the color dipole cascade model with fixed order matrix elements'. *JHEP* 05 (2002), p. 046. arXiv: hep-ph/0112284 [hep-ph].

[71] Michelangelo L. Mangano, Mauro Moretti and Roberto Pittau. 'Multijet matrix elements and shower evolution in hadronic collisions: $Wb\bar{b}$ + n jets as a case study'. *Nucl. Phys.* B632 (2002), pp. 343–362. arXiv: hep-ph/0108069 [hep-ph].

[72] Michelangelo L. Mangano et al. 'Matching matrix elements and shower evolution for top-quark production in hadronic collisions'. *JHEP* 01 (2007), p. 013. arXiv: hep-ph/0611129 [hep-ph].

[73] Stefan Höche et al. 'Matching parton showers and matrix elements'. *HERA and the LHC: A Workshop on the implications of HERA for LHC physics: Proceedings Part A*. 2006. arXiv: hep-ph/0602031 [hep-ph].

[74] Johan Alwall et al. 'Comparative study of various algorithms for the merging of parton showers and matrix elements in hadronic collisions'. *Eur. Phys. J.* C53 (2008), pp. 473–500. arXiv: 0706.2569 [hep-ph].

[75] S. Catani, Yuri L. Dokshitzer and B. R. Webber. 'The K^- perpendicular clustering algorithm for jets in deep inelastic scattering and hadron collisions'. *Phys. Lett.* B285 (1992), pp. 291–299.

[76] S. Catani et al. 'Longitudinally invariant K_t clustering algorithms for hadron hadron collisions'. *Nucl. Phys.* B406 (1993), pp. 187–224.

[77] T. Kinoshita. 'Mass Singularities of Feynman Amplitudes'. *Journal of Mathematical Physics* 3.4 (1962), pp. 650–677.

[78] T. D. Lee and M. Nauenberg. 'Degenerate Systems and Mass Singularities'. *Physical Review* 133 (1964), B1549–B1562.

[79] David A. Kosower. 'Antenna factorization of gauge theory amplitudes'. *Phys. Rev.* D57 (1998), pp. 5410–5416. arXiv: hep-ph/9710213 [hep-ph].

[80] A. Gehrmann-De Ridder, T. Gehrmann and E. W. Nigel Glover. 'Antenna subtraction at NNLO'. *JHEP* 09 (2005), p. 056. arXiv: hep-ph/0505111 [hep-ph].

[81] A. Daleo, T. Gehrmann and D. Maitre. 'Antenna subtraction with hadronic initial states'. *JHEP* 04 (2007), p. 016. arXiv: hep-ph/0612257 [hep-ph].

[82] S. Frixione, Z. Kunszt and A. Signer. 'Three jet cross-sections to next-to-leading order'. *Nucl. Phys.* B467 (1996), pp. 399–442. arXiv: hep-ph/9512328 [hep-ph].

[83] S. Frixione. 'A General approach to jet cross-sections in QCD'. *Nucl. Phys.* B507 (1997), pp. 295–314. arXiv: hep-ph/9706545 [hep-ph].

[84] S. Catani and M.H. Seymour. 'A General Algorithm for Calculating Jet Cross-Sections in NLO QCD'. *Nuclear Physics B* 485 (1997), pp. 291–419. arXiv: hep-ph/9605323 [hep-ph].

[85] S. Schumann and F. Krauss. 'A Parton Shower Algorithm Based on Catani-Seymour Dipole Factorisation'. *Journal of High Energy Physics* 0803 (2008), p. 038. arXiv: 0709.1027 [hep-ph].

[86] S. Frixione and B. R. Webber. 'Matching NLO QCD Computations and Parton Shower Simulations'. *Journal of High Energy Physics* 0206 (2002), p. 029. arXiv: hep-ph/0204244 [hep-ph].

[87] Paolo Nason. 'A New method for combining NLO QCD with shower Monte Carlo algorithms'. *JHEP* 11 (2004), p. 040. arXiv: hep-ph/0409146 [hep-ph].

[88] Stefano Frixione, Paolo Nason and Carlo Oleari. 'Matching NLO QCD computations with Parton Shower simulations: the POWHEG method'. *JHEP* 11 (2007), p. 070. arXiv: 0709.2092 [hep-ph].

[89] Thomas Gehrmann et al. 'NLO QCD matrix elements + parton showers in e^+e^- —> hadrons'. *JHEP* 01 (2013), p. 144. arXiv: 1207.5031 [hep-ph].

[90] S. Hoeche et al. 'QCD Matrix Elements + Parton Showers: The NLO Case'. *Journal of High Energy Physics* 1304 (2013), p. 027. arXiv: 1207.5030 [hep-ph].

[91] X. Artru and G. Mennessier. 'String model and multiproduction'. *Nucl. Phys.* B70 (1974), pp. 93–115.

[92] Bo Andersson et al. 'Parton Fragmentation and String Dynamics'. *Phys. Rept.* 97 (1983), pp. 31–145.

[93] Bo Andersson. *The Lund Model*. Cambridge University Press, 1998.

[94] Geoffrey C. Fox and Stephen Wolfram. 'A Model for Parton Showers in QCD'. *Nucl. Phys.* B168 (1980), pp. 285–295.

[95] Richard D. Field and Stephen Wolfram. 'A QCD Model for e+ e- Annihilation'. *Nucl. Phys.* B213 (1983), pp. 65–84.

[96] B. R. Webber. 'A QCD Model for Jet Fragmentation Including Soft Gluon Interference'. *Nucl. Phys.* B238 (1984), pp. 492–528.

[97] Jan-Christopher Winter, Frank Krauss and Gerhard Soff. 'A Modified cluster hadronization model'. *Eur. Phys. J.* C36 (2004), pp. 381–395. arXiv: hep-ph/0311085 [hep-ph].

[98] Georges Aad et al. 'Measurement of the underlying event in jet events from 7 TeV proton-proton collisions with the ATLAS detector'. *Eur. Phys. J.* C74.8 (2014), p. 2965. arXiv: 1406.0392 [hep-ex].

[99] Georges Aad et al. 'Measurement of distributions sensitive to the underlying event in inclusive Z-boson production in pp collisions at $\sqrt{s} = 7$ TeV with the ATLAS detector'. *Eur. Phys. J.* C74.12 (2014), p. 3195. arXiv: 1409.3433 [hep-ex].

[100] Georges Aad et al. 'Measurements of underlying-event properties using neutral and charged particles in pp collisions at 900 GeV and 7 TeV with the ATLAS detector at the LHC'. *Eur. Phys. J.* C71 (2011), p. 1636. arXiv: 1103.1816 [hep-ex].

[101] Georges Aad et al. 'Measurement of underlying event characteristics using charged particles in pp collisions at $\sqrt{s} = 900GeV$ and 7 TeV with the ATLAS detector'. *Phys. Rev.* D83 (2011), p. 112001. arXiv: 1012.0791 [hep-ex].

[102] Vardan Khachatryan et al. 'Measurement of the underlying event activity using charged-particle jets in proton-proton collisions at sqrt(s) = 2.76 TeV'. *JHEP* 09 (2015), p. 137. arXiv: 1507.07229 [hep-ex].

[103] Serguei Chatrchyan et al. 'Jet and underlying event properties as a function of charged-particle multiplicity in proton–proton collisions at $\sqrt{s} = 7$ TeV'. *Eur. Phys. J.* C73.12 (2013), p. 2674. arXiv: 1310.4554 [hep-ex].

[104] Serguei Chatrchyan et al. 'Study of the underlying event at forward rapidity in pp collisions at $\sqrt{s} = 0.9$, 2.76, and 7 TeV'. *JHEP* 04 (2013), p. 072. arXiv: 1302.2394 [hep-ex].

[105] Serguei Chatrchyan et al. 'Measurement of the underlying event activity in *pp* collisions at $\sqrt{s} = 0.9$ and 7 TeV with the novel jet-area/median approach'. *JHEP* 08 (2012), p. 130. arXiv: 1207.2392 [hep-ex].

[106] Serguei Chatrchyan et al. 'Measurement of the underlying event in the Drell-Yan process in proton-proton collisions at $\sqrt{s} = 7$ TeV'. *Eur. Phys. J.* C72 (2012), p. 2080. arXiv: 1204.1411 [hep-ex].

[107] Torbjorn Sjostrand and Maria van Zijl. 'A Multiple Interaction Model for the Event Structure in Hadron Collisions'. *Phys. Rev.* D36 (1987), p. 2019.

[108] A. V. Semenov. 'LanHEP: A Package for automatic generation of Feynman rules in gauge models' (1996). arXiv: hep-ph/9608488 [hep-ph].

[109] A. V. Semenov. 'LanHEP: A Package for automatic generation of Feynman rules in field theory. Version 2.0' (2002). arXiv: hep-ph/0208011 [hep-ph].

[110] A. Semenov. 'LanHEP: A Package for the automatic generation of Feynman rules in field theory. Version 3.0'. *Comput. Phys. Commun.* 180 (2009), pp. 431–454. arXiv: 0805.0555 [hep-ph].

[111] A. Semenov. 'LanHEP - a package for automatic generation of Feynman rules from the Lagrangian. Updated version 3.1' (2010). arXiv: 1005.1909 [hep-ph].

[112] A. Semenov. 'LanHEP — A package for automatic generation of Feynman rules from the Lagrangian. Version 3.2'. *Comput. Phys. Commun.* 201 (2016), pp. 167–170. arXiv: 1412.5016 [physics.comp-ph].

[113] Florian Staub. 'From Superpotential to Model Files for FeynArts and CalcHep / CompHep'. *Comput. Phys. Commun.* 181 (2010), pp. 1077–1086. arXiv: 0909.2863 [hep-ph].

[114] Florian Staub. 'Automatic Calculation of supersymmetric Renormalization Group Equations and Self Energies'. *Comput. Phys. Commun.* 182 (2011), pp. 808–833. arXiv: 1002.0840 [hep-ph].

[115] Florian Staub. 'SARAH 3.2: Dirac Gauginos, UFO output, and more'. *Comput. Phys. Commun.* 184 (2013), pp. 1792–1809. arXiv: 1207.0906 [hep-ph].

[116] Florian Staub. 'SARAH 4: A tool for (not only SUSY) model builders'. *Comput. Phys. Commun.* 185 (2014), pp. 1773–1790. arXiv: 1309.7223 [hep-ph].

[117] Neil D. Christensen and Claude Duhr. 'FeynRules - Feynman rules made easy'. *Comput. Phys. Commun.* 180 (2009), pp. 1614–1641. arXiv: 0806.4194 [hep-ph].

[118] Neil D. Christensen et al. 'A Comprehensive approach to new physics simulations'. *Eur. Phys. J.* C71 (2011), p. 1541. arXiv: 0906.2474 [hep-ph].

[119] Neil D. Christensen et al. 'Introducing an interface between WHIZARD and FeynRules'. *Eur. Phys. J.* C72 (2012), p. 1990. arXiv: 1010.3251 [hep-ph].

[120] Claude Duhr and Benjamin Fuks. 'A superspace module for the FeynRules package'. *Comput. Phys. Commun.* 182 (2011), pp. 2404–2426. arXiv: 1102.4191 [hep-ph].

[121] Adam Alloul et al. 'Automated mass spectrum generation for new physics'. *Eur. Phys. J.* C73.2 (2013), p. 2325. arXiv: 1301.5932 [hep-ph].

[122] Adam Alloul et al. 'FeynRules 2.0 - A complete toolbox for tree-level phenomenology'. *Comput.Phys.Commun.* 185 (2014), pp. 2250–2300. arXiv: 1310.1921 [hep-ph].

[123] K. Hagiwara et al. 'Supersymmetry simulations with off-shell effects for the CERN LHC and an ILC'. *Phys. Rev.* D73 (2006), p. 055005. eprint: hep-ph/0512260.

[124] T. Gleisberg et al. 'Helicity formalism for spin-2 particles'. *JHEP* 09 (2003), p. 001. eprint: hep-ph/0306182.

[125] Athanasios Dedes et al. 'Searching for Nambu-Goldstone Bosons at the LHC'. *JHEP* 11 (2008), p. 036. arXiv: 0807.4666 [hep-ph].

[126] Can Kilic, Steffen Schumann and Minho Son. 'Searching for Multijet Resonances at the LHC'. *JHEP* 04 (2009), p. 128. arXiv: 0810.5542 [hep-ph].

[127] Steffen Schumann, Adrien Renaud and Dirk Zerwas. 'Hadronically decaying color-adjoint scalars at the LHC'. *JHEP* 09 (2011), p. 074. arXiv: 1108.2957 [hep-ph].

[128] Celine Degrande et al. 'UFO - The Universal FeynRules Output'. *Comput. Phys. Commun.* 183 (2012), pp. 1201–1214. arXiv: 1108.2040 [hep-ph].

[129] P. Skands et al. 'SUSY Les Houches accord: interfacing SUSY spectrum calculators, decay packages, and event generators'. *JHEP* 07 (2004), p. 036. arXiv: hep-ph/0311123.

[130] Johan Alwall et al. 'A Les Houches Interface for BSM Generators' (2007). arXiv: 0712.3311 [hep-ph].

[131] B. Allanach et al. 'SUSY Les Houches Accord 2'. *Comp. Phys. Commun.* 180 (2009), pp. 8–25. arXiv: 0801.0045 [hep-ph].

[132] J. Bellm et al. 'Herwig++ 2.7 Release Note' (2013). arXiv: 1310.6877 [hep-ph].

[133] Johannes Bellm et al. 'Herwig 7.0/Herwig++ 3.0 release note'. *Eur. Phys. J.* C76.4 (2016), p. 196. arXiv: 1512.01178 [hep-ph].

[134] J. Alwall et al. 'MadGraph 5 : Going Beyond'. *Journal of High Energy Physics* 1106 (2011), p. 128. arXiv: 1106.0522 [hep-ph].

[135] Frits A. Berends and W. Giele. 'The Six Gluon Process as an Example of Weyl-Van Der Waerden Spinor Calculus'. *Nucl. Phys.* B294 (1987), p. 700.

[136] Frits A. Berends and W. T. Giele. 'Recursive Calculations for Processes with n Gluons'. *Nucl. Phys.* B306 (1988), p. 759.

[137] Claude Duhr, Stefan Hoeche and Fabio Maltoni. 'Color-dressed recursive relations for multi-parton amplitudes'. *JHEP* 08 (2006), p. 062. arXiv: hep-ph/0607057 [hep-ph].

[138] R. Kleiss and G. van den Oord. *Recursive equations for Majorana currents*. 2009. arXiv: 0906.0697 [hep-ph].

[139] Kaoru Hagiwara and D. Zeppenfeld. 'Helicity Amplitudes for Heavy Lepton Production in e+ e- Annihilation'. *Nucl. Phys.* B274 (1986), pp. 1–32.

[140] Hartmut M. Pilkuhn. *The Interactions of Hadrons*. North-Holland, 1967.

[141] Peter Richardson. 'Spin correlations in Monte Carlo simulations'. *JHEP* 11 (2001), p. 029. arXiv: hep-ph/0110108 [hep-ph].

[142] Timothy M. P. Tait. 'The tW^- mode of single top production'. *Phys. Rev.* D61 (1999), p. 034001. arXiv: hep-ph/9909352 [hep-ph].

[143] Stefano Frixione et al. 'Single-top hadroproduction in association with a W boson'. *JHEP* 07 (2008), p. 029. arXiv: 0805.3067 [hep-ph].

[144] T. Gleisberg et al. 'Cross-sections for multiparticle final states at a linear collider'. *Eur. Phys. J.* C34 (2004), pp. 173–180. arXiv: hep-ph/0311273 [hep-ph].

[145] Mikhail A. Shifman et al. 'Low-Energy Theorems for Higgs Boson Couplings to Photons'. *Sov. J. Nucl. Phys.* 30 (1979). [Yad. Fiz.30,1368(1979)], pp. 711–716.

[146] A. I. Vainshtein, Valentin I. Zakharov and Mikhail A. Shifman. 'Higgs Particles'. *Sov. Phys. Usp.* 23 (1980). [Usp. Fiz. Nauk131,537(1980)], pp. 429–449.

[147] M. B. Voloshin. 'Once Again About the Role of Gluonic Mechanism in Interaction of Light Higgs Boson with Hadrons'. *Sov. J. Nucl. Phys.* 44 (1986). [Yad. Fiz.44,738(1986)], p. 478.

[148] A. S. Belyaev et al. 'Strongly interacting vector bosons at the CERN LHC: Quartic anomalous couplings'. *Phys. Rev.* D59 (1999), p. 015022. arXiv: hep-ph/9805229 [hep-ph].

[149] Oscar J. P. Eboli et al. 'Anomalous quartic gauge boson couplings at hadron colliders'. *Phys. Rev.* D63 (2001), p. 075008. arXiv: hep-ph/0009262 [hep-ph].

[150] O. J. P. Eboli, M. C. Gonzalez-Garcia and S. M. Lietti. 'Bosonic quartic couplings at CERN LHC'. *Phys. Rev.* D69 (2004), p. 095005. arXiv: hep-ph/0310141 [hep-ph].

[151] O. J. P. Eboli, M. C. Gonzalez-Garcia and J. K. Mizukoshi. 'p p —> j j e+- mu+- nu nu and j j e+- mu-+ nu nu at O(alpha(em)**6) and O(alpha(em)**4 alpha(s)**2) for the study of the quartic electroweak gauge boson vertex at CERN LHC'. *Phys. Rev.* D74 (2006), p. 073005. arXiv: hep-ph/0606118 [hep-ph].

[152] Hsin-Chia Cheng, Konstantin T. Matchev and Martin Schmaltz. 'Bosonic supersymmetry? Getting fooled at the CERN LHC'. *Phys. Rev.* D66 (2002), p. 056006. arXiv: hep-ph/0205314 [hep-ph].

[153] Juan Antonio Aguilar-Saavedra et al. 'Supersymmetry parameter analysis: SPA convention and project'. *Eur. Phys. J.* C46 (2006), pp. 43–60. arXiv: hep-ph/0511344 [hep-ph].

[154] Priscila de Aquino et al. 'ALOHA: Automatic Libraries Of Helicity Amplitudes for Feynman Diagram Computations'. *Comput. Phys. Commun.* 183 (2012), pp. 2254–2263. arXiv: 1108.2041 [hep-ph].

[155] Abdelhak Djouadi. 'The Anatomy of electro-weak symmetry breaking. I: The Higgs boson in the standard model'. *Phys. Rept.* 457 (2008), pp. 1–216. arXiv: hep-ph/0503172 [hep-ph].

[156] Bernd A. Kniehl and Michael Spira. 'Low-energy theorems in Higgs physics'. *Z. Phys.* C69 (1995), pp. 77–88. arXiv: hep-ph/9505225 [hep-ph].

[157] M. Gillioz et al. 'Higgs Low-Energy Theorem (and its corrections) in Composite Models'. *JHEP* 10 (2012), p. 004. arXiv: 1206.7120 [hep-ph].

[158] S. Dawson. 'Radiative corrections to Higgs boson production'. *Nucl. Phys.* B359 (1991), pp. 283–300.

[159] A. Djouadi, M. Spira and P. M. Zerwas. 'Production of Higgs bosons in proton colliders: QCD corrections'. *Phys. Lett.* B264 (1991), pp. 440–446.

[160] Robert V. Harlander and William B. Kilgore. 'Next-to-Next-to-Leading Order Higgs Production at Hadron Colliders'. *Phys. Rev. Lett.* 88 (2002), p. 201801. arXiv: hep-ph/0201206 [hep-ph].

[161] Charalampos Anastasiou and Kirill Melnikov. 'Higgs boson production at hadron colliders in NNLO QCD'. *Nucl. Phys.* B646 (2002), pp. 220–256. arXiv: hep-ph/0207004 [hep-ph].

[162] V. Ravindran, J. Smith and W. L. van Neerven. 'NNLO corrections to the total cross-section for Higgs boson production in hadron hadron collisions'. *Nucl. Phys.* B665 (2003), pp. 325–366. arXiv: hep-ph/0302135 [hep-ph].

[163] Charalampos Anastasiou et al. 'Higgs boson gluon–fusion production at threshold in N^3LO QCD'. *Phys. Lett.* B737 (2014), pp. 325–328. arXiv: 1403.4616 [hep-ph].

[164] Charalampos Anastasiou et al. 'Higgs boson gluon-fusion production beyond threshold in N^3LO QCD'. *JHEP* 03 (2015), p. 091. arXiv: 1411.3584 [hep-ph].

[165] Charalampos Anastasiou et al. 'Higgs Boson Gluon-Fusion Production in QCD at Three Loops'. *Phys. Rev. Lett.* 114 (2015), p. 212001. arXiv: 1503.06056 [hep-ph].

[166] D. Graudenz, M. Spira and P. M. Zerwas. 'QCD corrections to Higgs boson production at proton proton colliders'. *Phys. Rev. Lett.* 70 (1993), pp. 1372–1375.

[167] S. Dawson and R. Kauffman. 'QCD corrections to Higgs boson production: nonleading terms in the heavy quark limit'. *Phys. Rev.* D49 (1994), pp. 2298–2309. arXiv: hep-ph/9310281 [hep-ph].

[168] M. Spira et al. 'Higgs boson production at the LHC'. *Nucl. Phys.* B453 (1995), pp. 17–82. arXiv: hep-ph/9504378 [hep-ph].

[169] Simone Marzani et al. 'Higgs production via gluon-gluon fusion with finite top mass beyond next-to-leading order'. *Nucl. Phys.* B800 (2008), pp. 127–145. arXiv: 0801.2544 [hep-ph].

[170] Alexey Pak, Mikhail Rogal and Matthias Steinhauser. 'Virtual three-loop corrections to Higgs boson production in gluon fusion for finite top quark mass'. *Phys. Lett.* B679 (2009), pp. 473–477. arXiv: 0907.2998 [hep-ph].

[171] Alexey Pak, Mikhail Rogal and Matthias Steinhauser. 'Finite top quark mass effects in NNLO Higgs boson production at LHC'. *JHEP* 02 (2010), p. 025. arXiv: 0911.4662 [hep-ph].

[172] Robert V. Harlander et al. 'Higgs Production in Gluon Fusion at Next-to-Next-to-Leading Order QCD for Finite Top Mass'. *Eur. Phys. J.* C66 (2010), pp. 359–372. arXiv: 0912.2104 [hep-ph].

[173] Robert V. Harlander and Kemal J. Ozeren. 'Finite Top Mass Effects for Hadronic Higgs Production at Next-to-Next-to-Leading Order'. *JHEP* 11 (2009), p. 088. arXiv: 0909.3420 [hep-ph].

[174] Robert V. Harlander and Kemal J. Ozeren. 'Top mass effects in Higgs production at next-to-next-to-leading order QCD: Virtual corrections'. *Phys. Lett.* B679 (2009), pp. 467–472. arXiv: 0907.2997 [hep-ph].

[175] Charalampos Anastasiou et al. 'High precision determination of the gluon fusion Higgs boson cross-section at the LHC' (2016). arXiv: 1602.00695 [hep-ph].

[176] U. Baur and E.W.N. Glover. 'Higgs Boson Production at Large Transverse Momentum in Hadronic Collisions'. *Nuclear Physics B* 339.1 (1990), pp. 38–66. ISSN: 0550-3213.

[177] R.K. Ellis et al. 'Higgs decay to $\tau\tau$ - A possible signature of intermediate mass Higgs bosons at high energy hadron colliders'. *Nuclear Physics B* 297.2 (1988), pp. 221–243. ISSN: 0550-3213.

[178] Wai-Yee Keung and Frank J. Petriello. 'Electroweak and Finite Quark-Mass Effects on the Higgs Boson Transverse Momentum Distribution'. *Phys. Rev.* D80 (2009), p. 013007. arXiv: 0905.2775 [hep-ph].

[179] Andrea Banfi, Adam Martin and Veronica Sanz. 'Probing top-partners in Higgs + jets'. *JHEP* 08 (2014), p. 053. arXiv: 1308.4771 [hep-ph].

[180] Nikolas Kauer and Giampiero Passarino. 'Inadequacy of zero-width approximation for a light Higgs boson signal'. *JHEP* 08 (2012), p. 116. arXiv: 1206.4803 [hep-ph].

[181] Fabrizio Caola and Kirill Melnikov. 'Constraining the Higgs boson width with ZZ production at the LHC'. *Phys. Rev.* D88 (2013), p. 054024. arXiv: 1307.4935 [hep-ph].

[182] John M. Campbell, R. Keith Ellis and Ciaran Williams. 'Bounding the Higgs width at the LHC using full analytic results for $gg- > e^-e^+\mu^-\mu^+$'. *JHEP* 04 (2014), p. 060. arXiv: 1311.3589 [hep-ph].

[183] M. Grazzini and H. Sargsyan. 'Heavy-quark Mass Effects in Higgs Boson Production at the LHC'. *Journal of High Energy Physics* 1309 (2013), p. 129. arXiv: 1306.4581 [hep-ph].

[184] Charalampos Anastasiou, Kirill Melnikov and Frank Petriello. 'Fully differential Higgs boson production and the di-photon signal through next-to-next-to-leading order'. *Nucl. Phys.* B724 (2005), pp. 197–246. arXiv: hep-ph/0501130 [hep-ph].

[185] Massimiliano Grazzini. 'NNLO predictions for the Higgs boson signal in the H —> WW —> lnu lnu and H —> ZZ —> 4l decay channels'. *JHEP* 02 (2008), p. 043. arXiv: 0801.3232 [hep-ph].

[186] Stefano Catani and Massimiliano Grazzini. 'HNNLO: A Monte Carlo program to compute Higgs boson production at hadron colliders'. *PoS* RADCOR2007 (2007), p. 046. arXiv: 0802.1410 [hep-ph].

[187] Stefan Hoeche, Ye Li and Stefan Prestel. 'Higgs-boson production through gluon fusion at NNLO QCD with parton showers'. *Phys. Rev.* D90.5 (2014), p. 054011. arXiv: 1407.3773 [hep-ph].

[188] Radja Boughezal et al. 'Higgs boson production in association with a jet at next-to-next-to-leading order in perturbative QCD'. *JHEP* 06 (2013), p. 072. arXiv: 1302.6216 [hep-ph].

[189] X. Chen et al. 'Precise QCD predictions for the production of Higgs + jet final states'. *Phys. Lett.* B740 (2015), pp. 147–150. arXiv: 1408.5325 [hep-ph].

[190] Radja Boughezal et al. 'Higgs boson production in association with a jet at next-to-next-to-leading order'. *Phys. Rev. Lett.* 115.8 (2015), p. 082003. arXiv: 1504.07922 [hep-ph].

[191] Radja Boughezal et al. 'Higgs boson production in association with a jet at NNLO using jettiness subtraction'. *Phys. Lett.* B748 (2015), pp. 5–8. arXiv: 1505.03893 [hep-ph].

[192] H. van Deurzen et al. 'NLO QCD corrections to the production of Higgs plus two jets at the LHC'. *Phys. Lett.* B721 (2013), pp. 74–81. arXiv: 1301.0493 [hep-ph].

[193] G. Cullen et al. 'Next-to-Leading-Order QCD Corrections to Higgs Boson Production Plus Three Jets in Gluon Fusion'. *Phys. Rev. Lett.* 111.13 (2013), p. 131801. arXiv: 1307.4737 [hep-ph].

[194] Nicolas Greiner et al. 'Phenomenological analysis of Higgs boson production through gluon fusion in association with jets'. *JHEP* 01 (2016), p. 169. arXiv: 1506.01016 [hep-ph].

[195] U. Langenegger et al. 'SM and MSSM Higgs Boson Production: Spectra at Large Transverse Momentum'. *JHEP* 06 (2006), p. 035. arXiv: hep-ph/0604156 [hep-ph].

[196] Charalampos Anastasiou, Stefan Bucherer and Zoltan Kunszt. 'HPro: A NLO Monte-Carlo for Higgs Production via Gluon Fusion with Finite Heavy Quark Masses'. *JHEP* 10 (2009), p. 068. arXiv: 0907.2362 [hep-ph].

[197] E. Bagnaschi et al. 'Higgs Production via Gluon Fusion in the POWHEG Approach in the SM and in the MSSM'. *Journal of High Energy Physics* 1202 (2012), p. 088. arXiv: 1111.2854 [hep-ph].

[198] Johan Alwall, Qiang Li and Fabio Maltoni. 'Matched predictions for Higgs production via heavy-quark loops in the SM and beyond'. *Phys. Rev.* D85 (2012), p. 014031. arXiv: 1110.1728 [hep-ph].

[199] R. V. Harlander et al. 'Top-Mass Effects in Differential Higgs Production through Gluon Fusion at Order α_s^4'. *Journal of High Energy Physics* 1208 (2012), p. 139. arXiv: 1206.0157 [hep-ph].

[200] Emanuele Bagnaschi et al. 'Resummation Ambiguities in the Higgs Transverse Momentum Spectrum in the Standard Model and Beyond'. *JHEP* 01 (2016), p. 090. arXiv: 1510.08850 [hep-ph].

[201] Stefano Catani and Massimiliano Grazzini. 'An NNLO subtraction formalism in hadron collisions and its application to Higgs boson production at the LHC'. *Phys. Rev. Lett.* 98 (2007), p. 222002. arXiv: hep-ph/0703012 [hep-ph].

[202] M. Cacciari, G. P. Salam and G. Soyez. 'The Anti-k(t) Jet Clustering Algorithm'. *Journal of High Energy Physics* 0804 (2008), p. 063. arXiv: 0802.1189 [hep-ph].

[203] Malte Buschmann et al. 'Resolving the Higgs-Gluon Coupling with Jets'. *Phys. Rev.* D90.1 (2014), p. 013010. arXiv: 1405.7651 [hep-ph].

[204] Emanuele Bagnaschi and Alessandro Vicini. 'The Higgs Transverse Momentum Distribution in Gluon Fusion as a Multiscale Problem'. *JHEP* 01 (2016), p. 056. arXiv: 1505.00735 [hep-ph].

[205] Robert V. Harlander, Hendrik Mantler and Marius Wiesemann. 'Transverse Momentum Resummation for Higgs Production via Gluon Fusion in the MSSM'. *JHEP* 11 (2014), p. 116. arXiv: 1409.0531 [hep-ph].

[206] Nima Arkani-Hamed et al. 'Physics Opportunities of a 100 TeV Proton-Proton Collider' (2015). arXiv: 1511.06495 [hep-ph].

[207] Ian Hinchliffe et al. 'Luminosity goals for a 100-TeV pp collider'. *Int. J. Mod. Phys.* A30.23 (2015), p. 1544002. arXiv: 1504.06108 [hep-ph].

[208] Alexander Belyaev and Laura Reina. 'pp —> t anti-t H, H —> tau+ tau-: Toward a model independent determination of the Higgs boson couplings at the LHC'. *JHEP* 08 (2002), p. 041. arXiv: hep-ph/0205270 [hep-ph].

[209] Eilam Gross and Lidija Zivkovic. '$t\bar{t}H \to t\bar{t}\tau^+\tau^-$ - Toward the Measurement of the top-Yukawa Coupling'. *Eur. Phys. J.* C59 (2009), pp. 731–754.

[210] Tilman Plehn, Gavin P. Salam and Michael Spannowsky. 'Fat Jets for a Light Higgs'. *Phys. Rev. Lett.* 104 (2010), p. 111801. arXiv: 0910.5472 [hep-ph].

[211] Pierre Artoisenet et al. 'Unravelling $t\bar{t}h$ via the Matrix Element Method'. *Phys. Rev. Lett.* 111.9 (2013), p. 091802. arXiv: 1304.6414 [hep-ph].

[212] Matthew R. Buckley et al. 'Buckets of Higgs and Tops'. *JHEP* 02 (2014), p. 130. arXiv: 1310.6034 [hep-ph].

[213] Adam Falkowski. 'Pseudo-goldstone Higgs production via gluon fusion'. *Phys. Rev.* D77 (2008), p. 055018. arXiv: 0711.0828 [hep-ph].

[214] Ian Low and Alessandro Vichi. 'On the production of a composite Higgs boson'. *Phys. Rev.* D84 (2011), p. 045019. arXiv: 1010.2753 [hep-ph].

[215] Aleksandr Azatov and Jamison Galloway. 'Light Custodians and Higgs Physics in Composite Models'. *Phys. Rev.* D85 (2012), p. 055013. arXiv: 1110.5646 [hep-ph].

[216] Cédric Delaunay, Christophe Grojean and Gilad Perez. 'Modified Higgs Physics from Composite Light Flavors'. *JHEP* 09 (2013), p. 090. arXiv: 1303.5701 [hep-ph].

[217] Marc Montull et al. 'Higgs Couplings in Composite Models'. *Phys. Rev.* D88 (2013), p. 095006. arXiv: 1308.0559 [hep-ph].

[218] Z. Kunszt and F. Zwirner. 'Testing the Higgs sector of the minimal supersymmetric standard model at large hadron colliders'. *Nucl. Phys.* B385 (1992), pp. 3–75. arXiv: hep-ph/9203223 [hep-ph].

[219] Vernon D. Barger et al. 'Supersymmetric Higgs boson hadroproduction and decays including radiative corrections'. *Phys. Rev.* D45 (1992), pp. 4128–4147.

[220] Howard Baer et al. 'Observability of gamma gamma decays of Higgs bosons from supersymmetry at hadron supercolliders'. *Phys. Rev.* D46 (1992), pp. 1067–1075.

[221] John F. Gunion and Lynne H. Orr. 'Detecting the Higgs bosons of the minimal supersymmetric model'. *Phys. Rev.* D46 (1992), pp. 2052–2067.

[222] John F. Gunion, Howard E. Haber and Chung Kao. 'Searching for the CP odd Higgs boson of the minimal supersymmetric model at hadron supercolliders'. *Phys. Rev.* D46 (1992), pp. 2907–2917.

[223] Christophe Grojean et al. 'Very boosted Higgs in gluon fusion'. *JHEP* 05 (2014), p. 022. arXiv: 1312.3317 [hep-ph].

[224] Aleksandr Azatov and Ayan Paul. 'Probing Higgs couplings with high p_T Higgs production'. *JHEP* 01 (2014), p. 014. arXiv: 1309.5273 [hep-ph].

[225] Matthias Schlaffer et al. 'Boosted Higgs Shapes'. *Eur. Phys. J.* C74.10 (2014), p. 3120. arXiv: 1405.4295 [hep-ph].

[226] M. Dittmar and Herbert K. Dreiner. 'How to find a Higgs boson with a mass between 155-GeV - 180-GeV at the LHC'. *Phys. Rev.* D55 (1997), pp. 167–172. arXiv: hep-ph/9608317 [hep-ph].

[227] Michael Dittmar and H. Dreiner. *LHC Higgs Search with l+nul- nubar Final States*. Unpublished. 1997.

[228] Thomas Junk. 'Confidence level computation for combining searches with small statistics'. *Nucl. Instrum. Meth.* A434 (1999), pp. 435–443. arXiv: hep-ex/9902006 [hep-ex].

[229] Gunter Zech. 'Upper Limits in Experiments with Background Or Measurement Errors'. *Nucl. Instrum. Meth.* A277 (1989), p. 608.

[230] Alexander L. Read. 'Presentation of search results: The CL(s) technique'. *J. Phys.* G28 (2002). [,11(2002)], pp. 2693–2704.

[231] Vanda Silveira and A. Zee. 'SCALAR PHANTOMS'. *Phys. Lett.* B161 (1985), pp. 136–140.

[232] Donal O'Connell, Michael J. Ramsey-Musolf and Mark B. Wise. 'Minimal Extension of the Standard Model Scalar Sector'. *Phys. Rev.* D75 (2007), p. 037701. arXiv: hep-ph/0611014 [hep-ph].

[233] Vernon Barger et al. 'LHC Phenomenology of an Extended Standard Model with a Real Scalar Singlet'. *Phys. Rev.* D77 (2008), p. 035005. arXiv: 0706.4311 [hep-ph].

[234] Daniele Bertolini and Matthew McCullough. 'The Social Higgs'. *JHEP* 12 (2012), p. 118. arXiv: 1207.4209 [hep-ph].

[235] Robert Schabinger and James D. Wells. 'A Minimal spontaneously broken hidden sector and its impact on Higgs boson physics at the large hadron collider'. *Phys. Rev.* D72 (2005), p. 093007. arXiv: hep-ph/0509209 [hep-ph].

[236] Emidio Gabrielli et al. 'Towards Completing the Standard Model: Vacuum Stability, EWSB and Dark Matter'. *Phys. Rev.* D89.1 (2014), p. 015017. arXiv: 1309.6632 [hep-ph].

[237] Christoph Englert et al. 'Emergence of the Electroweak Scale through the Higgs Portal'. *JHEP* 04 (2013), p. 060. arXiv: 1301.4224 [hep-ph].

[238] Hooman Davoudiasl, Tao Han and Heather E. Logan. 'Discovering an invisibly decaying Higgs at hadron colliders'. *Phys. Rev.* D71 (2005), p. 115007. arXiv: hep-ph/0412269 [hep-ph].

[239] Oscar J. P. Eboli and D. Zeppenfeld. 'Observing an invisible Higgs boson'. *Phys. Lett.* B495 (2000), pp. 147–154. arXiv: hep-ph/0009158 [hep-ph].

[240] Debajyoti Choudhury and D. P. Roy. 'Signatures of an invisibly decaying Higgs particle at LHC'. *Phys. Lett.* B322 (1994), pp. 368–373. arXiv: hep-ph/9312347 [hep-ph].

[241] R. M. Godbole et al. 'Search for 'invisible' Higgs signals at LHC via associated production with gauge bosons'. *Phys. Lett.* B571 (2003), pp. 184–192. arXiv: hep-ph/0304137 [hep-ph].

[242] Georges Aad et al. 'Constraints on new phenomena via Higgs boson couplings and invisible decays with the ATLAS detector'. *JHEP* 11 (2015), p. 206. arXiv: 1509.00672 [hep-ex].

[243] Serguei Chatrchyan et al. 'Search for Invisible Decays of Higgs Bosons in the Vector Boson Fusion and Associated ZH Production Modes'. *Eur. Phys. J.* C74 (2014), p. 2980. arXiv: 1404.1344 [hep-ex].

[244] Georges Aad et al. 'Search for Invisible Decays of a Higgs Boson Produced in Association with a Z Boson in ATLAS'. *Phys. Rev. Lett.* 112 (2014), p. 201802. arXiv: 1402.3244 [hep-ex].

[245] Georges Aad et al. 'Search for invisible decays of the Higgs boson produced in association with a hadronically decaying vector boson in pp collisions at $\sqrt{s} = 8$ TeV with the ATLAS detector'. *Eur. Phys. J.* C75.7 (2015), p. 337. arXiv: 1504.04324 [hep-ex].

[246] Tao Han and S. Willenbrock. 'QCD Correction to the p p —> W H and Z H Total Cross-Sections'. *Phys. Lett.* B273 (1991), pp. 167–172.

[247] Oliver Brein, Abdelhak Djouadi and Robert Harlander. 'NNLO QCD Corrections to the Higgs-Strahlung Processes at Hadron Colliders'. *Phys. Lett.* B579 (2004), pp. 149–156. arXiv: hep-ph/0307206 [hep-ph].

[248] Vernon D. Barger et al. 'Higgs Boson Z^0 Associated Production From Fourth Generation Quarks at Super Collider Energies'. *Phys. Rev. Lett.* 57 (1986), p. 1672.

[249] Duane A. Dicus and Chung Kao. 'Higgs Boson - Z^0 Production From Gluon Fusion'. *Phys. Rev.* D38 (1988). [Erratum: Phys. Rev.D42,2412(1990)], p. 1008.

[250] Bernd A. Kniehl. 'Associated Production of Higgs and Z Bosons From Gluon Fusion in Hadron Collisions'. *Phys. Rev.* D42 (1990), pp. 2253–2258.

[251] L. D. Landau. 'The moment of a 2-photon System'. *Dok. Akad. Nauk SSSR* 60 (1948), p. 207.

[252] Chen-Ning Yang. 'Selection Rules for the Dematerialization of a Particle Into Two Photons'. *Phys. Rev.* 77 (1950), pp. 242–245.

[253] W. H. Furry. 'A Symmetry Theorem in the Positron Theory'. *Phys. Rev.* 51 (1937), pp. 125–129.

[254] T. Binoth, N. Kauer and P. Mertsch. 'Gluon-induced QCD corrections to pp —> ZZ —> l anti-l l-prime anti-l-prime'. *Proceedings, 16th International Workshop on Deep Inelastic Scattering and Related Subjects (DIS 2008)*. 2008, p. 142. arXiv: 0807.0024 [hep-ph].

[255] C. Zecher, T. Matsuura and J. J. van der Bij. 'Leptonic signals from off-shell Z boson pairs at hadron colliders'. *Z. Phys.* C64 (1994), pp. 219–226. arXiv: hep-ph/9404295 [hep-ph].

[256] T. Binoth et al. 'Gluon-induced W-boson pair production at the LHC'. *JHEP* 12 (2006), p. 046. arXiv: hep-ph/0611170 [hep-ph].

[257] John M. Campbell, R. Keith Ellis and Ciaran Williams. 'Gluon-Gluon Contributions to W+ W- Production and Higgs Interference Effects'. *JHEP* 10 (2011), p. 005. arXiv: 1107.5569 [hep-ph].

[258] L. Altenkamp et al. 'Gluon-induced Higgs-strahlung at next-to-leading order QCD'. *JHEP* 1302 (2013), p. 078. arXiv: 1211.5015 [hep-ph].

[259] Fabrizio Caola et al. 'QCD corrections to ZZ production in gluon fusion at the LHC'. *Phys. Rev.* D92.9 (2015), p. 094028. arXiv: 1509.06734 [hep-ph].

[260] Kirill Melnikov and Matthew Dowling. 'Production of two Z-bosons in gluon fusion in the heavy top quark approximation'. *Phys. Lett.* B744 (2015), pp. 43–47. arXiv: 1503.01274 [hep-ph].

[261] Fabrizio Caola et al. 'QCD corrections to W^+W^- production through gluon fusion'. *Phys. Lett.* B754 (2016), pp. 275–280. arXiv: 1511.08617 [hep-ph].

[262] Tom Melia et al. 'Gluon fusion contribution to W+W- + jet production'. *JHEP* 08 (2012), p. 115. arXiv: 1205.6987 [hep-ph].

[263] Francisco Campanario et al. 'ZZ+jet production via gluon fusion at the LHC'. *JHEP* 06 (2013), p. 069. arXiv: 1211.5429 [hep-ph].

[264] Pankaj Agrawal and Ambresh Shivaji. 'Di-Vector Boson + Jet Production via Gluon Fusion at Hadron Colliders'. *Phys. Rev.* D86 (2012), p. 073013. arXiv: 1207.2927 [hep-ph].

[265] Pankaj Agrawal and Ambresh Shivaji. 'Gluon Fusion Contribution to VHj Production at Hadron Colliders'. *Phys. Lett.* B741 (2015), pp. 111–116. arXiv: 1409.8059 [hep-ph].

[266] CMS Collaboration. *Performance of b tagging at sqrt(s)=8 TeV in multijet, ttbar and boosted topology events*. Tech. rep. CMS-PAS-BTV-13-001. Geneva: CERN, 2013.

[267] Laura Baudis. 'Direct dark matter detection: the next decade'. *Phys. Dark Univ.* 1 (2012), pp. 94–108. arXiv: 1211.7222 [astro-ph.IM].

[268] Teresa Marrodan Undagoitia and Ludwig Rauch. 'Dark matter direct-detection experiments'. *J. Phys.* G43.1 (2016), p. 013001. arXiv: 1509.08767 [physics.ins-det].

[269] Morad Aaboud et al. 'Search for new phenomena in final states with an energetic jet and large missing transverse momentum in pp collisions at $\sqrt{s} = 13$ TeV using the ATLAS detector' (2016). arXiv: 1604.07773 [hep-ex].

[270] Morad Aaboud et al. 'Search for new phenomena in events with a photon and missing transverse momentum in pp collisions at $\sqrt{s}$ = 13 TeV with the ATLAS detector'. *JHEP* 06 (2016), p. 059. arXiv: 1604.01306 [hep-ex].

[271] CMS Collaboration. 'Search for dark matter in association with a boosted top quark in the all hadronic final state' (2016).

[272] CMS Collaboration. 'Search for Dark Matter and Large Extra Dimensions in the gamma + MET final state in pp Collisions at sqrt(s) = 13 TeV' (2016).

[273] Vardan Khachatryan et al. 'Search for dark matter and unparticles produced in association with a Z boson in proton-proton collisions at $\sqrt{s}$ = 8 TeV'. *Phys. Rev.* D93.5 (2016), p. 052011. arXiv: 1511.09375 [hep-ex].

[274] CMS Collaboration. 'Search for dark matter production in association with jets, or hadronically decaying W or Z boson at $\sqrt{s}$ = 13 TeV' (2016).

[275] CMS Collaboration. 'Search for Dark Matter produced in association with bottom quarks' (2016).

[276] Patrick J. Fox et al. 'LEP Shines Light on Dark Matter'. *Phys. Rev.* D84 (2011), p. 014028. arXiv: 1103.0240 [hep-ph].

[277] Ian M. Shoemaker and Luca Vecchi. 'Unitarity and Monojet Bounds on Models for DAMA, CoGeNT, and CRESST-II'. *Phys. Rev.* D86 (2012), p. 015023. arXiv: 1112.5457 [hep-ph].

[278] Neal Weiner and Itay Yavin. 'How Dark Are Majorana WIMPs? Signals from MiDM and Rayleigh Dark Matter'. *Phys. Rev.* D86 (2012), p. 075021. arXiv: 1206.2910 [hep-ph].

[279] Giorgio Busoni et al. 'On the Validity of the Effective Field Theory for Dark Matter Searches at the LHC'. *Phys. Lett.* B728 (2014), pp. 412–421. arXiv: 1307.2253 [hep-ph].

[280] O. Buchmueller, Matthew J. Dolan and Christopher McCabe. 'Beyond Effective Field Theory for Dark Matter Searches at the LHC'. *JHEP* 01 (2014), p. 025. arXiv: 1308.6799 [hep-ph].

[281] Oliver Buchmueller et al. 'Characterising dark matter searches at colliders and direct detection experiments: Vector mediators'. *JHEP* 01 (2015), p. 037. arXiv: 1407.8257 [hep-ph].

[282] Giorgio Busoni et al. 'On the Validity of the Effective Field Theory for Dark Matter Searches at the LHC, Part II: Complete Analysis for the s-channel'. *JCAP* 1406 (2014), p. 060. arXiv: 1402.1275 [hep-ph].

[283] Giorgio Busoni et al. 'On the Validity of the Effective Field Theory for Dark Matter Searches at the LHC Part III: Analysis for the t-channel'. *JCAP* 1409 (2014), p. 022. arXiv: 1405.3101 [hep-ph].

[284] Johan Alwall, Philip Schuster and Natalia Toro. 'Simplified Models for a First Characterization of New Physics at the LHC'. *Phys. Rev.* D79 (2009), p. 075020. arXiv: 0810.3921 [hep-ph].

[285] Daniele Alves. 'Simplified Models for LHC New Physics Searches'. *J. Phys.* G39 (2012). Ed. by Nima Arkani-Hamed et al., p. 105005. arXiv: 1105.2838 [hep-ph].

[286] Jessica Goodman and William Shepherd. 'LHC Bounds on UV-Complete Models of Dark Matter' (2011). arXiv: 1111.2359 [hep-ph].

[287] Thomas Jacques and Karl Nordstrom. 'Mapping monojet constraints onto Simplified Dark Matter Models'. *JHEP* 06 (2015), p. 142. arXiv: 1502.05721 [hep-ph].

[288] Rohini M. Godbole, Gaurav Mendiratta and Tim M. P. Tait. 'A Simplified Model for Dark Matter Interacting Primarily with Gluons'. *JHEP* 08 (2015), p. 064. arXiv: 1506.01408 [hep-ph].

[289] Jalal Abdallah et al. 'Simplified Models for Dark Matter Searches at the LHC'. *Phys. Dark Univ.* 9-10 (2015), pp. 8–23. arXiv: 1506.03116 [hep-ph].

[290] Daniel Abercrombie et al. 'Dark Matter Benchmark Models for Early LHC Run-2 Searches: Report of the ATLAS/CMS Dark Matter Forum' (2015). Ed. by Antonio Boveia et al. arXiv: 1507.00966 [hep-ex].

[291] Matthew R. Buckley, David Feld and Dorival Goncalves. 'Scalar Simplified Models for Dark Matter'. *Phys. Rev.* D91 (2015), p. 015017. arXiv: 1410.6497 [hep-ph].

[292] Matthew R. Buckley and Dorival Goncalves. 'Constraining the Strength and CP Structure of Dark Production at the LHC: the Associated Top-Pair Channel'. *Phys. Rev.* D93.3 (2016). [Phys. Rev.D93,034003(2016)], p. 034003. arXiv: 1511.06451 [hep-ph].

[293] Ulrich Haisch, Felix Kahlhoefer and James Unwin. 'The impact of heavy-quark loops on LHC dark matter searches'. *JHEP* 07 (2013), p. 125. arXiv: 1208.4605 [hep-ph].

[294] Ulrich Haisch, Felix Kahlhoefer and Emanuele Re. 'QCD effects in mono-jet searches for dark matter'. *JHEP* 12 (2013), p. 007. arXiv: 1310.4491 [hep-ph].

[295] Ulrich Haisch, Anthony Hibbs and Emanuele Re. 'Determining the structure of dark-matter couplings at the LHC'. *Phys. Rev.* D89 (2014), p. 034009. arXiv: 1311.7131 [hep-ph].

[296] Andreas Crivellin, Francesco D'Eramo and Massimiliano Procura. 'New Constraints on Dark Matter Effective Theories from Standard Model Loops'. *Phys. Rev. Lett.* 112 (2014), p. 191304. arXiv: 1402.1173 [hep-ph].

[297] Christoph Englert, Matthew McCullough and Michael Spannowsky. 'S-Channel Dark Matter Simplified Models and Unitarity' (2016). arXiv: 1604.07975 [hep-ph].

[298] Karim Ghorbani. 'Fermionic dark matter with pseudo-scalar Yukawa interaction'. *JCAP* 1501 (2015), p. 015. arXiv: 1408.4929 [hep-ph].

[299] Mihailo Backovic et al. 'Higher-order QCD predictions for dark matter production at the LHC in simplified models with s-channel mediators'. *Eur. Phys. J.* C75.10 (2015), p. 482. arXiv: 1508.05327 [hep-ph].

[300] Philip Harris et al. 'Constraining Dark Sectors at Colliders: Beyond the Effective Theory Approach'. *Phys. Rev.* D91 (2015), p. 055009. arXiv: 1411.0535 [hep-ph].

[301] Olivier Mattelaer and Eleni Vryonidou. 'Dark matter production through loop-induced processes at the LHC: the s-channel mediator case'. *Eur. Phys. J.* C75.9 (2015), p. 436. arXiv: 1508.00564 [hep-ph].

[302] Ulrich Haisch and Emanuele Re. 'Simplified dark matter top-quark interactions at the LHC'. *JHEP* 06 (2015), p. 078. arXiv: 1503.00691 [hep-ph].

[303] Asher Berlin et al. 'Pseudoscalar Portal Dark Matter'. *Phys. Rev.* D92 (2015), p. 015005. arXiv: 1502.06000 [hep-ph].

[304] Gino Isidori, Yosef Nir and Gilad Perez. 'Flavor Physics Constraints for Physics Beyond the Standard Model'. *Ann. Rev. Nucl. Part. Sci.* 60 (2010), p. 355. arXiv: 1002.0900 [hep-ph].

[305] D. S. Akerib et al. 'First results from the LUX dark matter experiment at the Sanford Underground Research Facility'. *Phys. Rev. Lett.* 112 (2014), p. 091303. arXiv: 1310.8214 [astro-ph.CO].

[306] M. Ackermann et al. 'Searching for Dark Matter Annihilation from Milky Way Dwarf Spheroidal Galaxies with Six Years of Fermi Large Area Telescope Data'. *Phys. Rev. Lett.* 115.23 (2015), p. 231301. arXiv: 1503.02641 [astro-ph.HE].

[307] Gary Steigman, Basudeb Dasgupta and John F. Beacom. 'Precise Relic WIMP Abundance and its Impact on Searches for Dark Matter Annihilation'. *Phys. Rev.* D86 (2012), p. 023506. arXiv: 1204.3622 [hep-ph].

[308] Geoffrey T. Bodwin et al. 'Higgs boson decays to quarkonia and the $H\bar{c}c$ coupling'. *Phys. Rev.* D88.5 (2013), p. 053003. arXiv: 1306.5770 [hep-ph].

[309] Alexander L. Kagan et al. 'Exclusive Window onto Higgs Yukawa Couplings'. *Phys. Rev. Lett.* 114.10 (2015), p. 101802. arXiv: 1406.1722 [hep-ph].

[310] Gino Isidori, Aneesh V. Manohar and Michael Trott. 'Probing the nature of the Higgs-like Boson via $h \to V\mathcal{F}$ decays'. *Phys. Lett.* B728 (2014), pp. 131–135. arXiv: 1305.0663 [hep-ph].

[311] Matthias Koenig and Matthias Neubert. 'Exclusive Radiative Higgs Decays as Probes of Light-Quark Yukawa Couplings'. *JHEP* 08 (2015), p. 012. arXiv: 1505.03870 [hep-ph].

[312] Georges Aad et al. 'Search for Higgs and Z Boson Decays to $J/\psi\gamma$ and $\Upsilon(nS)\gamma$ with the ATLAS Detector'. *Phys. Rev. Lett.* 114.12 (2015), p. 121801. arXiv: 1501.03276 [hep-ex].

[313] Vardan Khachatryan et al. 'Search for a Higgs boson decaying into $\gamma^*\gamma \to \ell\ell\gamma$ with low dilepton mass in pp collisions at $\sqrt{s} = 8$ TeV'. *Phys. Lett.* B753 (2016), pp. 341–362. arXiv: 1507.03031 [hep-ex].

[314] David Curtin et al. 'Exotic decays of the 125 GeV Higgs boson'. *Phys. Rev.* D90.7 (2014), p. 075004. arXiv: 1312.4992 [hep-ph].

[315] Jeremy Bernon et al. 'Scrutinizing the alignment limit in two-Higgs-doublet models: m_h=125 GeV'. *Phys. Rev.* D92.7 (2015), p. 075004. arXiv: 1507.00933 [hep-ph].

[316] K. A. Olive et al. 'Review of Particle Physics'. *Chin. Phys.* C38 (2014), p. 090001.

[317] Andrey Katz, Minho Son and Brock Tweedie. 'Jet Substructure and the Search for Neutral Spin-One Resonances in Electroweak Boson Channels'. *JHEP* 03 (2011), p. 011. arXiv: 1010.5253 [hep-ph].

[318] Sebastian Schaetzel and Michael Spannowsky. 'Tagging highly boosted top quarks'. *Phys. Rev.* D89.1 (2014), p. 014007. arXiv: 1308.0540 [hep-ph].

[319] Andrew J. Larkoski, Fabio Maltoni and Michele Selvaggi. 'Tracking down hyper-boosted top quarks'. *JHEP* 06 (2015), p. 032. arXiv: 1503.03347 [hep-ph].

[320] Michael Spannowsky and Martin Stoll. 'Tracking New Physics at the LHC and beyond'. *Phys. Rev.* D92.5 (2015), p. 054033. arXiv: 1505.01921 [hep-ph].

[321] J. de Favereau et al. 'DELPHES 3, A modular framework for fast simulation of a generic collider experiment'. *JHEP* 02 (2014), p. 057. arXiv: 1307.6346 [hep-ex].

[322] Andreas Hocker et al. 'TMVA - Toolkit for Multivariate Data Analysis'. *PoS* ACAT (2007), p. 040. arXiv: physics/0703039 [PHYSICS].

[323] G. C. Branco et al. 'Theory and phenomenology of two-Higgs-doublet models'. *Phys. Rept.* 516 (2012), pp. 1–102. arXiv: 1106.0034 [hep-ph].

[324] Mirkoantonio Casolino et al. 'Probing a light CP-odd scalar in di-top-associated production at the LHC'. *Eur. Phys. J.* C75 (2015), p. 498. arXiv: 1507.07004 [hep-ph].

[325] David Eriksson, Johan Rathsman and Oscar Stal. '2HDMC: Two-Higgs-Doublet Model Calculator Physics and Manual'. *Comput. Phys. Commun.* 181 (2010), pp. 189–205. arXiv: 0902.0851 [hep-ph].

[326] Michael E. Peskin and Tatsu Takeuchi. 'A New constraint on a strongly interacting Higgs sector'. *Phys. Rev. Lett.* 65 (1990), pp. 964–967.

[327] Michael E. Peskin and Tatsu Takeuchi. 'Estimation of oblique electroweak corrections'. *Phys. Rev.* D46 (1992), pp. 381–409.

[328] Philip Bechtle et al. 'HiggsBounds: Confronting Arbitrary Higgs Sectors with Exclusion Bounds from LEP and the Tevatron'. *Comput. Phys. Commun.* 181 (2010), pp. 138–167. arXiv: 0811.4169 [hep-ph].

[329] Philip Bechtle et al. 'HiggsBounds 2.0.0: Confronting Neutral and Charged Higgs Sector Predictions with Exclusion Bounds from LEP and the Tevatron'. *Comput. Phys. Commun.* 182 (2011), pp. 2605–2631. arXiv: 1102.1898 [hep-ph].

[330] Philip Bechtle et al. 'Recent Developments in HiggsBounds and a Preview of HiggsSignals'. *PoS* CHARGED2012 (2012), p. 024. arXiv: 1301.2345 [hep-ph].

[331] Philip Bechtle et al. 'Applying Exclusion Likelihoods from LHC Searches to Extended Higgs Sectors'. *Eur. Phys. J.* C75.9 (2015), p. 421. arXiv: 1507.06706 [hep-ph].

[332] Philip Bechtle et al. 'HiggsSignals: Confronting arbitrary Higgs sectors with measurements at the Tevatron and the LHC'. *Eur. Phys. J.* C74.2 (2014), p. 2711. arXiv: 1305.1933 [hep-ph].

[333] Philip Bechtle et al. 'Probing the Standard Model with Higgs signal rates from the Tevatron, the LHC and a future ILC'. *JHEP* 11 (2014), p. 039. arXiv: 1403.1582 [hep-ph].